THE RELATIONSHIP BETWEEN MORPHOLOGY AND IONIC CONDUCTIVITY OF SILK AND CELLULOSE BIOCOMPOSITES

By

BAILEY BLESSING

A thesis submitted to the

Graduate School-Camden

Rutgers, The State University of New Jersey

In partial fulfillment of the requirements

For the degree of Master of Science

Graduate Program in Chemistry

Written under the direction of

Dr. David Salas-de la Cruz

And approved by

_____

Dr. David Salas-de la Cruz, Ph.D.

_____

Dr. Sean M. O'Malley, Ph.D.

_____

Dr. Guillaume Lamoureux, Ph.D.

Camden, New Jersey

May 2020

THESIS ABSTRACT

The Relationship Between Morphology and Ionic Conductivity of Silk and Cellulose Biocomposites

by BAILEY BLESSING

Thesis Director:
Dr. David Salas-de la Cruz

Structural proteins and polysaccharides form hydrophobic and electrostatic interactions when mixed, and the resulting matrices can exhibit novel and useful properties. This study investigates the morphology, and physicochemical properties, especially ionic conductivity, of a mixture of silk and cellulose biomacromolecules as a function of composition, ionic liquid type, coagulation agent, and ionic liquid concentration. The structural, morphological, thermal, mechanical, and conductive properties of biomaterials composed of microcrystalline cellulose and *Bombyx mori* silk when regenerated together using ionic liquids and various coagulation agents were investigated using a diverse set of techniques including scanning electron microscopy (SEM), Fourier transform infrared spectroscopy (FTIR), thermal gravimetric analysis (TGA), differential scanning calorimetry (DSC), X-ray scattering, atomic force microscopy (AFM) based nanoindentation, and dielectric relaxation spectroscopy (DRS). The results demonstrate that the thermal, electrical, and mechanical properties were dependent on intermolecular interactions dictated by the type of ionic liquid used during the coagulation process. X-ray scattering provided information on how cellulose semicrystallinity varied with coagulation agent, composition, and ionic liquid concentration. Specifically, samples containing a

higher percentage of cellulose and coagulated with hydrogen peroxide showed an increase in cellulose semicrystallinity, ultimately impacting properties such as elastic modulus, hardness, and ionic conductivity of the biocomposites. Also, the results revealed a strong correlation between β-sheet content and cellulose semicrystallinity and ionic conductivity. Specifically, it was seen that when the composition of silk and cellulose is equal, or the composition of silk is higher, the ionic conductivity is dependent on protein β-sheet content, with increasing β-sheet content leading to higher ionic conductivity. When the cellulose composition was higher than the silk, cellulose morphology and physicochemical properties became an essential factor in determining the ionic conductivity of the biocomposites. Furthermore, a change in the ionic liquid concentration in the biomaterial resulted in strong morphological and ionic conductivity changes. For these reasons, it is possible to suggest that ionic conductivity is dominated by molecular composition, ionic concentration, and morphology, as stated by the Vogel-Fulcher-Tammann model.

Dedications

I want to dedicate my thesis to my family for their unconditional support, encouragement, and love throughout the entirety of my academic career. My parents, Jeffrey and Stacey Blessing, have been nothing but patient and helpful through this journey. My brother, Austin Blessing, has also been someone I have been able to count on for help and reassurance when times were tough during my graduate school career. He also managed to make me laugh and bring a smile to my face during extremely stressful times. Thank you for always being there for me. I am incredibly fortunate to have this amazing family I can call my own.

Acknowledgments

I would like to thank Dr. Salas-de la Cruz for guiding me throughout my graduate academic career. You were always positive, energetic, and passionate about the work we do, and this helped show me what to strive for when conducting my work. You also helped me throughout my schooling by not only being patient with me during the entirety of this project but additionally encouraging me and believing in me to complete this critical research task. Thank you for teaching me about myself and helping me to grow as a person. I have learned valuable life skills along this journey that I will be able to use in my future.

I would also like to thank Mrs. Craig for supporting me throughout this journey. When completing my undergraduate degree, you were always there to not only be my teacher but also to help me whenever I had a question or concern. You allowed me to become a teacher for the Chemistry department, and as a result, assisted in me obtaining this Teaching Assistantship position to gain my Master's degree. Without you, I would not have gotten to where I am today. You have been someone who motivated me to do my best, encouraged me to keep going when times were stressful and challenging, and someone I could talk to when I needed advice or a laugh. Thank you for always being there for me and helping me achieve this milestone in my life.

Table of Contents

Copyright © 2019 by John Wiley & Sons, Inc. (Granted permission to use this material.)

List of Tables

List of Figures

Chapter 1

Introduction

Biomaterials can be defined as both natural and synthetic materials that are designed to be used in relation to biological systems [1]. Natural materials can include cultured cells, and natural polymers, such as silk, cellulose, collagen, keratin, microbial polyesters, chitosan, and many others [2-3]. Approximately 65 years ago, the field of biomaterials did not exist as it does today. Since then, the research on these critical materials has grown not only steadily, but also rapidly since they encompass many desirable properties such as biodegradability (depending on materials used), low-cost (compared to other resources that could be utilized in their place), and tunability (in terms of their morphological, mechanical and physical properties). As a result of these desirable properties, biomaterials now hold high importance in multiple disciplines and fields, which include chemistry, medicine, materials science, and biology. For example, biomaterials can be integrated into equipment utilized in biotechnological applications, used for tissue engineering, applied to grow cells in culture, used for sutures and wound dressings, and used to create artificial skin [1, 3].

While these applications are essential, the field in which biomaterials sees the most use and demand is medicine [1]. Materials utilized in medical use can fall into three classes, with biomaterials falling into Class III, which means they are in constant contact with tissues [2]. Within this class, there are three specific types of biomaterials, which include bioactive (i.e., replicating natural tissue functions and properties), biodegradable (i.e., the

body absorbs the materials, and they are eventually replaced with regenerating tissues), and bioinert (i.e., no host reactions, but the structures remain) [2].

One of the most critical requirements of biomaterials when biologically adapted for medical use is biocompatibility, which is when a material, in a particular application, is capable of making the desired response within the host [1]. This requirement can be broken down into three separate types of biocompatibility, including mechanical, interfacial, and the ability of the material to biochemically and mechanically work well together with the tissues. Mechanical biocompatibility relies on shape, size, and mechanical properties. Interfacial biocompatibility relies on organ dysfunctions, tissue disturbance, and ingredient release [2]. Since the issue of biocompatibility has been taken into account when designing materials, the medical field has and will continue to see advancements in biomaterials as they are used in multiple facets such as diagnosis, repair, treatment, and replacement [4]. The demand for new technology and ideas is high as the population not only keeps growing but also lives longer to require more care and treatment against disease and illness [4]. Two advancements using biomaterials in the medical discipline include scaffolds for tissue growth as well as drug delivery system capsules for delivering drugs to a specific target [5]. Also, advancements have been made in medical applications of biomaterials for implantable and biodegradable batteries. Currently, toxic electrode materials are used in the batteries of long-lasting implants. These new batteries aim to be not only biodegradable but also biocompatible while still performing their desired function [6].

Proteins can be used to create a biomaterial when blended with another material, creating a biocomposite. This material falls into the class of polypeptides, which, on the small-scale level, consist of amino acids covalently bonded together, forming peptide

bonds [3]. Many natural proteins have been studied for their unique electrical, optical, mechanical, electromagnetic, and chemical properties [7]. These original properties help to create multiple types of resources with a wide range of functional requirements. Examples of natural proteins include collagens (generally, in animal tissues), keratins (found in epidermal structures such as wool, hair, and nails), silks (created by spiders and silkworms), resilins (generally elastic rubbers), and elastins (used to form elastic fibers within tissues). These different proteins can come from several sources or be created by various insects, including rat tail and Achilles tendon, as well as spiders, silkworms, rat mites, and scorpions, respectively [3, 7-8]. This distinction between protein type also leads to a very diverse variation in the protein's highly repetitive amino acid sequence, in turn causing differences in secondary structures, which can include β-sheets, alpha helices, random coils, side chains, and turns [7]. Each unique material has distinct functional roles in nature as well as vital applications in the world of biomaterials, such as biosensors and tissue regeneration [7].

Silk is a specific biopolymer that is extremely important in creating biomaterials. The process of making silk involves specialized glands where the production of silk proteins occurs. After this happens, the proteins are moved into the lumen of the gland and eventually spun into fibers, which can vary drastically in properties, composition, structure, and amino acid composition due to different sources [8]. There are several medicinal applications for these fibers, such as controlled release, nerve guides, dental fibers that can release drugs, and sutures capable of releasing antibiotics, [3, 8].

The natural protein used in this study is *Bombyx mori* silk created by the *Bombyx mori* silkworm. This has been used for decades in creating biomedical sutures [8]. This insect

spins the water-soluble silk fibroin into fibers coated with sericin proteins, a sticky, glue-like substance. Once the spinning step takes place, the silk gets transformed into an insoluble state partially composed of anti-parallel β-sheets compared to its once silk solution state [7]. Each of these states is known as silk I and silk II. Specifically, silk I is the water-soluble form, while silk II is the transformed insoluble fiber [9]. Silk I often changes to silk II, the more common form, due to its instability to mechanical deformation [10]. There are also differences in structure between these two silk forms. Silk I has both hydrogen-bonded and antiparallel sheets, while silk II contains alternating back to back sheets [10]. The insoluble *Bombyx mori* silk fibroin form includes the amino acids glycine, alanine, and serine in the distinct repetition [GSGAGA]n, with the structure shown below in **Figure 1.1**. Some desirable properties of this form of silk include toughness, slow degradability, high biocompatibility, and high tensile strength [7, 11]. This particular silk is exceptionally stable, and also very difficult to dissolve in ordinary solvents including water, due to the hydrophobicity of the silk, the large amount of hydrogen bonding, and crystallinity [8]. This can be overcome using particular solvents.

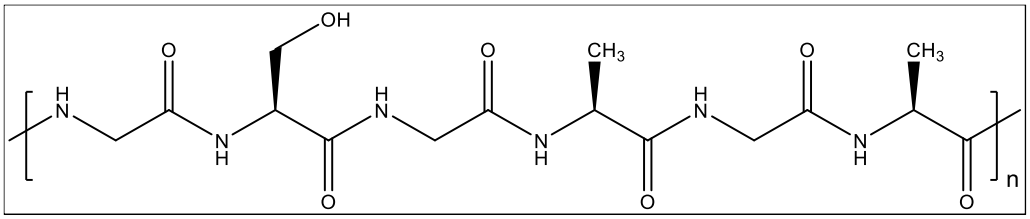

Figure 1.1. *The repeat unit of Bombyx mori silk fibroin.*

Polysaccharides can be used to combine with proteins to form biocomposites with useful and novel properties. This biopolymer group is a small subset of the carbohydrates group [12], something that is often consumed by people in their daily diet. They are

considered to be the most abundant renewable resource when discussing natural polymers, even generating more than synthetic polymers each year [13]. While some polysaccharides give cells stored energy, others are structural building blocks that naturally occur in nature [12]. Also, they are considered to be stable when compared to other groups of biopolymers, including nucleic acids and proteins [14]. Some common examples of polysaccharides that fall into these categories include starch, chitin, cellulose, yeast, as well as xylan [13]. This group of polymers can contain varying molecular weights, properties leading to solubility or insolubility in water, and advantages such as non-immunogenicity, not being irreversibly denatured when heated, low toxicity, and environmental safety [14]. A polysaccharide can be built from several of the common base saccharides, including monosaccharides, disaccharides, and oligosaccharides. A disaccharide contains two monosaccharides connected through a glycosidic linkage. Eventually, this builds up to a polysaccharide comprised of several saccharide units, generally more than ten, that are connected through glycosidic linkages [13-15]. These long chains can either be branched or linear, and have varying molecular weights from low, intermediate, to high [14-15]. Based on these differences, polysaccharides can have several different applications in various fields. For example, they can be used for nanocomposites and nanomaterials, small scale materials [14], and as bioactive polysaccharides, which can include creating gels, and utilizing properties of polysaccharides for drug release agents, plasma substitutes, and the making of materials used in the pharmaceutical industry [15]. Also, polysaccharides can have specific biological activities, including anti-tumor, antigenicity, and the ability to create new drugs and vaccines [15]. Given all of these applications, it is easy to observe why polysaccharides have become such an essential part of the biomaterials field.

The polysaccharide used in this study is cellulose, specifically Avicel cellulose, which is a type of microcrystalline cellulose. Cellulose is a polysaccharide that is found in numerous locations, including a specific species of slime mold, algae, and other higher plants, as well as the secondary cell wall [16-18]. Since it is found in many different plants, it is considered to be the most abundant natural biomolecule on earth [19-20]. There are several forms of cellulose, including cellulose I, II, III, and IV, each having their own defining characteristics [13]. Cellulose I has parallel chain packing, cellulose II is generally regenerated and has anti-parallel chain packing, cellulose III is considered to be highly crystalline and is converted from cellulose I using means such as immersion in liquid ammonia and high levels of pressure [21-22], and cellulose IV is converted from either cellulose I or cellulose III [13, 21-22]. Cellulose II can sometimes be found naturally as a mutant bacteria strain product, in a low-temperature treatment bacteria product, and a *Halycistis* cell wall component [16], but often it is created by converting cellulose I to cellulose II through either mercerization or regeneration processes [23]. This new form is less crystalline than the original form of cellulose I, making it easier to work with for application purposes [23]. All of these forms have several glucose residues connected through a β-(1–4) glycosidic link, but they can vary in orientation [20]. The generic structure of cellulose is shown below in **Figure 1.2**. Cellulose has several different applications, including but not limited to photoelectric devices, packaging materials, structural materials, filtration materials, and use in biomedical engineering [24]. For example, cellulose I, the microcrystalline, natural form of cellulose, can be found in Iα and Iβ crystalline allomorphs, generally existing as a mixture of these two when found in nature, with Iβ being the more prominent structure found in plants [20]. Both forms have opposite facing glucose units in an alternating fashion,

and the parallel chains are connected through hydrogen bonding between the hydroxyl groups and hydrogen groups. Through van der Waals attractions and CH-O interactions, these chains are stacked on top of each other creating sheets [20]. This helps to explain why cellulose I is crystalline in nature and very difficult to breakdown [23]. Specifically, there are several intra- and intermolecular hydrogen bonds within this structure due to the numerous hydroxyl groups [13, 23]. This contributes to cellulose's lack of solubility in typical solvents, such as water or organic solvents.

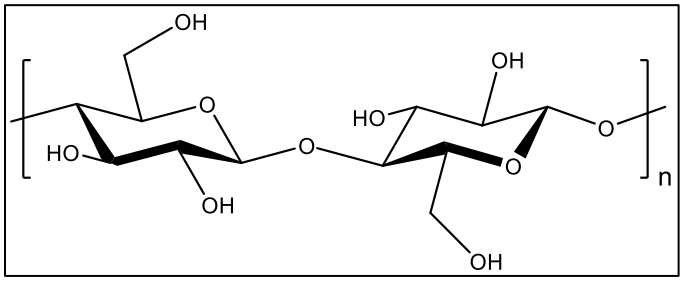

Figure 1.2. *The repeat unit of microcrystalline Avicel cellulose.*

For this reason, ionic liquids are used as the solvent in the dissolution process of *Bombyx mori* silk and microcrystalline Avicel cellulose. When creating a biocomposite with these two materials, unique challenges are presented, but this combination helps to enhance properties that each biomaterial may be lacking [25]. The first step in forming a silk-cellulose biocomposite is the dissolution of both materials, but this cannot be achieved easily since both silk and cellulose are challenging to break down. This is in part due to their crystalline structures, which include β-sheet content and close chain packing and stiffness from hydrogen bonding, respectively [11, 26]. To overcome this challenge, ionic liquids are used. The first attempted use of ionic liquids was in the 1960s for electrolytes in thermal batteries at the U.S. Air Force Academy. However, they had many shortcomings

and were finally overcome by second-generation ionic liquids in the early 1990s [27]. After this occurred, in 2003, ionic liquids were used in the first industrial process, expanding the interest in these liquids [28]. These solvents used to be known as molten salts at room temperature, but this proposed they were corrosive, viscous, and high-temperature media [28]. This was not the reality, so they are now known as ionic liquids, which are liquids at temperatures less than 100 °C [27, 29]. These liquids are made up entirely of ions compared to something that would be considered a solution, like salt in water [28]. They have several desirable properties, including high thermal stability, the ability to be recycled and reused, wide electrochemical windows, and negligible vapor pressure, which means they do not contribute volatile organic compounds to the atmosphere [28-30]. In addition, ionic liquids can be used for several different applications including the creation of devices that can replace capacitors and batteries [31], dissolution of enzymes [32], and an industrial process called BASIL, biphasic acid scavenging using ionic liquids, which helps to separate waste from the reaction mixture and regenerate the ionic liquid for further use [33].

Depending on the desired application, ionic liquids can be catered to the specific needs by choosing a certain anion, cation, or both [34]. A specific type of ionic liquid used in this study is imidazolium-based ionic liquids. In these ionic liquids, the cation is the imidazole ring with a particular substituent, which can vary, and the anion is an ion that is negatively charged and can be either smaller or larger than the cation. Depending on the anion chosen for these ionic liquids, as well as the substituent of the imidazole ring, the needs of specific applications can be met [35-36]. Imidazole ionic liquids have gained much attention in recent years due to their tunability. This is partially due to the imidazole ring, which can both donate and accept protons [35]. The five-membered imidazole ring consists

of nitrogen and carbon entirely, with two double bonds in the ring, one between carbon and nitrogen and the other between carbon and carbon. This ring is also associated with high thermal stability, some ionic liquids surpassing 275 °C, something that other ionic liquid types may not be able to offer to the same degree [35]. This stability in part is due to the ionic interaction through pi-pi stacking of the imidazolium portion of the ionic liquid, and hydrogen bonding [35].

The two specific ionic liquids studied in this experiment were 1-ethyl-3-methyl-imidazolium acetate (EMIMAc) as well as 1-ethyl-3-methyl-imidazolium chloride (EMIMCl), with their structures pictured below in **Figure 1.3**. Both of these structures have the same cation with the imidazole ring and a methyl and ethyl substituent. The anion is different for both. EMIMAc has a bulky acetate anion group compared to the small chloride anion in EMIMCl. Each of these ionic liquids is capable of breaking down materials with extensive hydrogen bonding, such as cellulose [37]. Both ionic liquids have hydrogen bonding within their structure. EMIMAc can form hydrogen bonds between the 1-ethyl-3-methylimidazolium cation and the acetate anion [38], and EMIMCl can form one strong hydrogen bond between a chloride anion and multiple hydrogen atoms in the imidazole ring [39]. This hydrogen bonding leads to some of the desired and useful properties of ionic liquids, listed previously. These two ionic liquids were chosen for experimentation for specific reasons. First, the alteration of the anion allows analysis to take place based on just changing this one part of the structure, rather than the cation as well. It is crucial to see how different properties of the material are changed by changing this one small part of the structure. Second, it has previously been proven that bulky cations, such as those with long or bulky side chains on the imidazole ring, are less efficient at dissolving cellulose [40]. Third,

the two chosen ionic liquids have smaller side chains attached to the ring, and therefore should be more efficient at breaking apart cellulose. Finally, EMIMCl is explicitly found to be proficient at dissolving cellulose because the chloride anion interacts with the hydroxyl groups of cellulose [26]. This ionic liquid is also found to be effective at dissolving silk because it can interrupt hydrogen bonding within the β-sheet [41]. EMIMAc should work similarly as EMIMCl since the only thing that is changed is the anion.

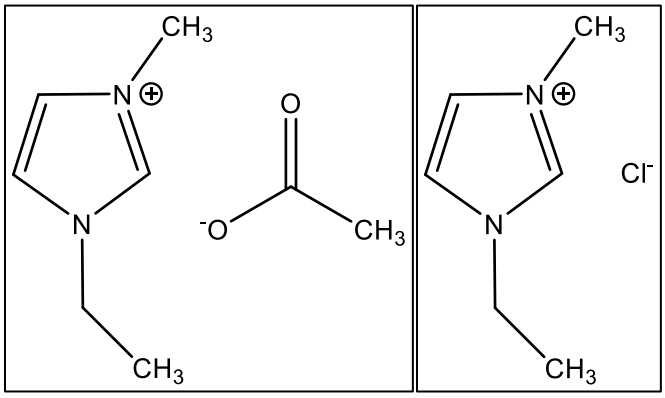

Figure 1.3. *Structures of ionic liquids; 1-ethyl-3-methyl-imidazolium acetate on the left and 1-ethyl-3-methyl imidazolium chloride on the right.*

When these two ionic liquids are used, silk and cellulose can be dissolved into the ionic liquid, and eventually wholly regenerated into a biocomposite using a coagulation agent. Briefly mentioned above, the cation and anion of the ionic liquid associates with the oxygen and hydrogen from the cellulose hydroxyl groups, respectively [26-27]. This disrupts the hydrogen bonding and makes it so the cellulose can be broken down. A similar process occurs within the silk polymer chains. Once both biopolymers are dissolved completely, they can amalgamate through different types of interactions in solution, including electrostatic, hydrogen bonding, and hydrophobic-hydrophobic [25, 42]. After this step occurs, a solution named a coagulation agent, such as ethanol, water, or hydrogen peroxide is used

to remove the ionic liquid. This results in the majority of the anions moving into the liquid and out of the biocomposite. There is a small amount of residual ionic liquid left behind in the biocomposite, but it is not a significant amount; however, they are the source of ion conduction. Once the ionic liquid is removed, cellulose and silk can come together in its absence since there is very little competition for bonding at this point. However, some of this minimal competition comes from the coagulation agent, which forms a hydrogel. For this to be removed, a drying process is applied, and once this is completed, a solid biocomposite is finally formed [43]. Altering the ionic liquid, coagulation agent, or sample ratio is a way in which the physicochemical properties such as the thermal, morphological, and conductive properties of the biocomposites can be tuned. In the past, it has been shown treating the solution with alcohol led to an increase in β-sheet content [44], which ultimately changes other properties within the material. Also, the use of various ionic liquids, compositions, and coagulation agents have been ways to alter the morphological properties of the biocomposites [25, 43, 45]. This helps to tune the materials to the specific desired use or field.

As a result of the difference in processing conditions of the biocomposites, including ionic liquid, coagulation agent, or biopolymer ratio, the ionic conductivity of these samples will differ. Ionic conductivity involves the movement of ions throughout a structure. In the biocomposite structure, ionic conductivity comes from the movement of residual ionic liquid ions throughout both the amorphous and semicrystalline regions within the structure. Conductivity is expressed using the equation,

(1.1) $$\sigma = pq\mu$$

where σ is the conductivity, p is the density of positive charges, q is the charge of the cation, and μ is the mobility of the ions [46]. This equation can be broken down further by defining the density of charges as well as the mobility and charge components [46-47]. The way in which the density is defined is by using an Arrhenius relationship in the form of the equation,

$$p_0 = p_\infty \exp(\frac{-E_a}{RT}) \tag{1.2}$$

where R is the ideal gas constant, T is the temperature, p_∞ is the cation concentration as the temperature approaches infinity, and E_a is the activation energy of an anion-cation pair, or conducting ions [47-48]. The mobility of the ions can be defined in two ways. The first is from the equation,

$$\mu = \mu_\infty \exp\left(-\frac{B}{T-T_0}\right) \tag{1.3}$$

where μ_∞ is infinite temperature mobility, T_0 is when mobility goes to zero, or the Vogel temperature, and B is a constant and has temperature units [47]. This equation expresses that there should be a Vogel- Fulcher-Tammann temperature dependence since the segmental motion of the polymer matrix partially controls the free ion mobility in a polymer [47]. In addition to this equation for the mobility of ions, there is another from the Einstein relation in the form of the equation,

$$\mu = \frac{Dq}{kT} \tag{1.4}$$

where k is the Boltzmann's constant, and D is the ion diffusivity [47]. This is very important because ionic conductivity can be broken down into two different main processes, which include ion diffusion and ion dissociation [46]. Ion diffusion is built into the ion mobility component of the overall conductivity equation. This process includes both the segmental

motion of polymer chains as well as ion hopping [48-49]. This diffusivity variable can be described by the Stokes-Einstein equation,

(1.5) $$D = \frac{kT}{6\pi\eta r}$$

where r is the hydrodynamic radius, and η is the viscosity [46]. By looking at this equation used in the Einstein relation formula, it is clear to see that the ion mobility is inversely related to viscosity [46]. Intuitively, this should make sense because when something becomes more viscous, it is more challenging to travel through. As a result, it would be expected that the ion diffusion would decrease. When relating all of these terms in one formula for ionic conductivity, the ion mobility relating to the VFT temperature dependence is used as well as the expanded equation of ion density. The equation below is obtained by combining both equations into the central conductivity equation [46-48].

(1.6) $$\sigma = q\rho_{\infty}\mu_{\infty} exp\left(-\frac{E_a}{RT}\right) exp\left(-\frac{B}{(T-T_0)}\right)$$

Several parameters listed above impact the conductivity of materials, including temperature, viscosity, ion dissociation energies, and ion concentrations. However, in the above equation, one of the most critical variables is B, a constant related to the energy barrier for the mobility of ions. This constant is expressed as the sum of two other constants,

(1.7) $$B = B_{seg} + B_h$$

where B_h is the ion hopping energy barrier and B_{seg} is the polymer segmental motion energy barrier [46]. This expression of the constant helps to demonstrate the direct relationship to morphology [46]. This means when there is a change in the morphology of the polymer system, changes in B occur, which then influences the ionic conductivity. An example of this morphology and conductivity relationship is seen by Pereira et al., where

higher β-sheet content correlated with higher ionic conductivity in prepared silk fibroin separators [50].

Ionic conductivity can be calculated at each measured temperature. The formula $\sigma = {}^{L}/_{AR}$ was used to calculate the conductivity. L is the distance between the two inner electrodes, A is the cross-sectional area, and R is the resistance determined from the Nyquist plot using the high x-intercept of the semicircle [51]. A Nyquist plot is created by plotting Z" on the *y*-axis, the imaginary part of impedance, versus Z' on the *x*-axis, the real part of impedance [52]. In addition, the Bode plot is created by plotting the logarithm of Z on the *y*-axis versus the logarithm of the frequency on the *x*-axis [53]. It is also possible to determine the resistance from this plot. When there is a plateau at high frequency, the impedance value is equal to the resistance [54]. When plotting the conductivity data, often, the logarithm of conductivity versus 1000/temperature is used to report the data. Further analysis can be used to determine the activation energy by plotting an Arrhenius plot. This is where the natural logarithm (ln) of conductivity is plotted on the *y*-axis, and 1/temperature in units of Kelvin is plotted on the *x*-axis. The slope of this graph is equal to $\frac{-E_a}{k_B}$, where E_a is the activation energy and k_B is the Boltzmann's constant equal to a value of 1.3806 x 10^{-23} J/K [55]. As a result, the activation energy can be calculated by multiplying the slope by the negative value of the Boltzmann's constant for the overall sample [55].

Biomaterials are essential for advancement in numerous fields. As a result, research in this field has expanded drastically over the past several years. Prior work has included the interactions between silk and cellulose, how ionic liquids affect morphology and other properties of the biocomposites, as well as how differing coagulation agents can influence resulting thermal and morphological properties. However, there has been a lesser amount

of work put into researching how the ionic conductivity of these biocomposites can not only be tuned for different applications but also how it is impacted when altering coagulant, ionic liquid or polymer ratio. This work aims to determine how the ionic conductivity of silk and cellulose biocomposites can change as a function of any one of these parameters, and as a result, how the resulting morphological, thermal, and mechanical properties change as well. Relating these changes in ionic conductivity to cellulose crystallinity, as well as β-sheet content in silk, helps to characterize the morphology of the system. Eventually, the main parameters may be able to be changed to tune the conductivity to ideal values for specific applications in the human body or electronic devices.

Chapter 2

The Impact of Composition and Morphology on Ionic Conductivity of Silk/Cellulose Bio-composites Fabricated from Ionic Liquid as a Function of Coagulation Agent

2.1. Introduction

Polysaccharides and proteins, when blended together, form biocomposites that can lead to new and useful properties and technologies such as scaffolds, drug delivery capsules, and bio-electrolyte membranes [5-6]. These materials could ideally be used in the human body as they have high biocompatibility and hold promise in the development of medical batteries. By furthering the understanding of the relationship between the ionic conductivity and the morphology, it would be possible to tune these biocomposites to a variety of applications.

Cellulose is a structural polymer and the most abundant polysaccharide on earth [20]. The natural polymer is formed of several repeating glucose residues connected through β-(1–4) glycosidic linkers [56]. The microcrystalline natural form, with a parallel arrangement of strands, is called cellulose I; several other versions of cellulose can exist as well, such as cellulose II and III [57]. Cellulose II contains antiparallel packing [16], and is often processed from cellulose I through regeneration or the use of caustic chemicals [23]. This technique is also used to create cellulose III [57]. However, this process is complicated since cellulose is resistant to breaking apart due to its complex hydrogen-bonding network [23]. Specifically, intra- and intermolecular hydrogen bonds occur within this structure due to the numerous hydroxyl groups, which make the polysaccharide resistant to breakage [13, 23].

Cellulose can be blended with *Bombyx mori* silk, a spin fiber coated in sericin proteins. This sericin coating is removed with different chemicals to ensure only the pure fibroin remains. These fibroins contain the amino acids glycine, alanine, and serine in the repeating formation $[GAGAGS]_n$ [7]. Some of the notable characteristics of this protein include high biocompatibility, slow degradability, toughness, and high tensile strength [7, 11]. These properties may result from the crystalline regions within the fibroin, which experience strong attraction through the hydrogen bonding of the C-O and N-H groups on the amino acids, which sometimes arrange in an antiparallel direction [58-59]. Within the protein, there are secondary structures, including alpha helices, random coils, side chains, and turns. However, one of the most essential secondary structures that can lead to changes in the physicochemical properties is β-sheets. Interestingly, random coils and alpha helices can be transformed into β-sheets using alcohol-based solutions [7, 11, 60-61].

Both of these materials, cellulose and silk, are considered to fall under the category of biomaterials, which are defined as materials that interact with biological systems and can be both manufactured and natural [5]. Being able to tune the thermal, conductive, and morphological properties from their native state into various biomaterial-based applications is imperative but presents challenges in terms of dissolution and fabrication. One way to dissolve these natural macromolecules, without affecting their molecular weight, is through the use of various ionic liquids [25, 43, 45, 62]. These are molten salts at room temperature with high ionic conductivity, wide electrochemical windows, and good thermal stability [26, 29]. During the dissolution process, the hydrogen bonding is disturbed by associating the anion and cation of the ionic liquid with the hydrogen and oxygen of the hydroxyl groups of cellulose [26-27]. Once the silk chains undergo a similar process, these

two biopolymers will interact through different types of interactions in solution: hydrophobic-hydrophobic, electrostatic, and hydrogen bonding [25, 42]. A coagulation agent, such as ethanol or water, is then used to remove the ionic liquid by causing the anions of the salt to move into the liquid and out of the biocomposite. Typically, only a small amount of residual ionic liquid is left. Once the ionic liquid is removed, the coagulant now creates a phase separation of liquid and hydrogel regions. Upon drying, the coagulant is removed, and as a result, the silk and cellulose can aggregate in its absence [25, 43, 45, 63].

Ionic conductivity in solid polymer electrolytes is dependent on the material's physiochemical properties, including morphology, which can directly affect ion diffusion and dissociation processes [46]. For example, natural silk was found to be considerably more conductive than natural cellulose, which demonstrates the significance that composition may play in connection with conductivity [64]. Additionally, a previous study demonstrated the effects of two ionic liquids, EMIMAc and EMIMCl, and two coagulation agents, 25% ethanol and 25% hydrogen peroxide, on resulting morphological, thermal, mechanical, and ionic conductivity properties [62]. The study revealed that the ionic conductivity was dependent on β-sheet content. Higher β-sheet content corresponded to higher ionic conductivity, a conclusion observed by others as well when using different materials and processing conditions [50, 62].

Based on these studies, a general hypothesis can be stated that the conductivity would correlate with the dominating polymer, such that higher silk content would lead to higher conductivity, and higher cellulose content would lead to lower conductivity. Therefore, in this study, the effects of varying composition on conductivity as well as other morphological, thermal, and mechanical properties will be investigated. Two different

ratios of silk and cellulose biocomposites used include 25% silk/75% cellulose and 75% silk/25% cellulose. Pure silk and pure cellulose samples were also created for comparison purposes. All samples, including silk, cellulose, and the biocomposites, were dissolved in 1-ethyl-3-methylimidazolium acetate and coagulated in various agents. It is evident from the data that the composition, as well as coagulation agent, produce morphological, thermal, mechanical, and conductive variations.

2.2. Experimental Section

Materials

Ionic Liquid

The ionic liquid, 1-Ethyl-3-methylimidazolium acetate (95%), was purchased from Sigma-Aldrich. Before use, the liquid was pretreated in a vacuum oven (30 inHg) at 50 °C for 24 hours. This removes any water in the ionic liquid.

Cellulose

Avicel microcrystalline cellulose of 250 μm (Techware: Z26578-0) was purchased from Analtech and used to mix with *Bombyx mori* silk. Like the ionic liquid, the cellulose was placed in a vacuum oven (30 inHg) at 50 °C for 24 hours to remove any residual water before mixing.

Silk

Treenway Silks (Lakewood, CO) was used to acquire the *Bombyx mori* silk cocoons. A 0.02 M $NaHCO_3$ (Sigma-Aldrich) solution was used to boil the silkworm

cocoons for 15 minutes. This removed the sericin coating on the fibers, followed by rinsing with deionized water three times to ensure all sericin was adequately removed. These degummed fibers air-dried overnight. Following this, they were put into a vacuum oven (30 inHg) at room temperature to remove moisture on the surface of the fibers.

Dissolution of the Protein and Polysaccharide

The ionic liquid and protein/polysaccharide were measured to be specific percentages of the total mass of the biocomposite film. The ionic liquid accounted for 90% of the mass, while the protein (silk) and polysaccharide (cellulose) together were measured to be 10% by mass of the film. The solids were broken down further into individual ratios of silk and cellulose. Specifically, one set of biocomposites contained 25% silk and 75% cellulose while the other contained 75% silk and 25% cellulose, in addition to the 100% silk and 100% cellulose samples. The pretreated ionic liquid was placed in a vial and then placed into a silica oil bath held at 80 °C. The dissolution process began by first adding silk to the vial, followed by cellulose. When both materials were fully dissolved in the ionic liquid, the solution was left to mix for 24 hours at 80 °C.

Preparation of Regenerated Biofilm

After 24 hours of continuous mixing, the gel solution was transferred into 12 mm x 12 mm x 1 mm polylactic acid 3-D printed molds. Specifically, 1 mL micropipette tips were first heated to 75 °C to ensure the solution did not solidify inside the tip. Then, the solution was pipetted into the molds. Once filled, each mold was placed in 100 mL of coagulation agent inside a 250 mL beaker and sealed with parafilm for 48 hours. This step removes as much ionic liquid as possible from the film as well as regenerates the natural

polymers. Once 48 hours had passed, each mold was removed and rinsed three times with distilled water to remove as much residual ionic liquid on the surface as possible. The molds were then transferred to Teflon Petri dishes and allowed to dry in a low-pressure desiccator.

Characterization

2.2.1. Fourier Transform Infrared Spectroscopy

Fourier Transform Infrared Spectroscopy (FTIR) analysis was performed using a Bruker ALPHA-Platinum ATR-FTIR Spectrometer with Platinum-Diamond sample module. Before any background scans and between each sample, acetone was used to clean the FTIR diamond and hammer. 32 sample scans in 6 different locations of the biocomposite were performed after 128 background scans. Following this, the amide I region (1595 cm^{-1}-1705 cm^{-1}) was studied using Fourier self-deconvolution. Specifically, Lorentzian line shape with a noise reduction factor of 0.3 and 25.614 cm^{-1} half-bandwidth was utilized for deconvolution. Fitting the results and integrating to find the area correlation to a particular wavelength was performed using Gaussian profiles. These analyses were run using Opus 7.2 software. After Fourier self-deconvolution, min-max normalization was used to normalize the data from 4000 cm^{-1} to 400 cm^{-1} to highlight the functional groups better.

2.2.2. Scanning Electron Microscopy

A JEOL JCM-6000 SEM was used for Scanning Electron Microscopy (SEM). The topography of the biocomposites was studied in the resulting images. A magnification of

200x was used to acquire images. Au-Pt coating was deposited onto the films to lessen the buildup of surface charge during imaging. The conductive coating was applied using a DII-29010SCTR Smart Coater at vacuum level 4 Pa with a deposition time of 60 seconds.

2.2.3. Thermogravimetric Analysis

TA Instruments Discovery TGA system was utilized to perform Thermogravimetric analysis (TGA) with 5 mg samples under a nitrogen gas purge of 25 mL/minute. The run was started at 30 °C, followed by an isothermal period of one minute, and ramped to 10 °C per minute to 600 °C. The furnace was allowed to cool to 30 °C in between each sample run. The data was analyzed using step transition analyses and derivative plots. Using these analysis techniques allowed the weight-loss percentage, temperature corresponding to the decomposition of the sample at its highest rate ($T_{\Delta Max}$), as well as the onset temperature of decomposition (T_{Onset}), to be determined.

2.2.4. Differential Scanning Calorimetry

5 mg samples encapsulated in aluminum Tzero pans were analyzed under a nitrogen gas flow of 50 mL per minute using the TA Instruments Differential Scanning Calorimetry (DSC). This was equipped with a refrigerated cooling system. Before running any samples, indium was used for DSC calibration for temperature and heat flow, and calibration of the heat capacity and heat flow was performed using sapphire and aluminum references. The samples were first equilibrated to room temperature, isothermal for 10 minutes, ramped 10.00 °C per minute to 120 °C, isothermal for 10 minutes to remove bound solvents, ramped 10.00 °C per minute back to -30 °C, isothermal for another 10 minutes, and ramped 10.00 °C per minute to 275 °C.

2.2.5. X-ray Scattering

Dual Source and Environmental X-ray Scattering (DEXS) was used to perform X-ray scattering under vacuum and at room temperature. Prior to running the samples, they were placed in a desiccator and then cut into squares that cover the sample holder. A high flux collimation with a 1.2 mm x 1.2 mm slot was used with a 600 second run time for the 75% silk and 100% silk samples, while 300 seconds was used for the 25% silk and 100% cellulose samples. Foxtrot 3.4.9 was used to evaluate the X-ray scattering profiles, and ultimately, azimuthal integration was used on the isotropic 2-D scattering patterns to yield intensity versus scattering vector.

2.2.6. Atomic Force Microscopy (Nanoindentation)

The elastic modulus of four silk-cellulose composites was measured at 120 °C via Atomic Force Microscopy (AFM). The samples were adhered to steel disks using silver paste and left in a fume hood to dry and to prevent adhesive vapor from depositing onto the sample surface. Subsequently, the samples were stored in a vacuum desiccator to keep the samples in a dehydrated state. An Asylum Research MFP-3D equipped with a Nanotools Biosphere BFP-40 AFM was employed for both topographical scans and nanoindentation measurements. The inverse optical lever sensitivity (InVols) of the AFM probe was determined by performing nanoindentation on a clean disk of mica and measuring the slope of the deflection versus cantilever position curve. The spring constant of the probe was extrapolated from its thermal oscillation spectrum. Prior to measurement, the samples were magnetically mounted onto a heating plate integrated into the AFM. The sample was allowed to heat at a rate of 5 °C per minute up to 120 °C. Subsequently, a 20 µm x 20 µm topographical scan was performed, followed by nanoindentation

measurements at 25 different locations. The topographical scan was done in tapping mode to prevent deformation by the tip. A force versus load-displacement curve was obtained from each nanoindentation, and the elastic moduli were extracted using the Johnson-Kendall-Roberts (JKR) model. The JKR model is a modification of the Hertzian model that accounts for the adhesion between the sample and tip during nanoindentation [65]. The JKR model is typically used when measuring soft materials where adhesion can strongly influence the determination of elastic properties [66]. While both the loading and unloading force versus indentation curves were collected, only the loading curve was considered during analysis. The JKR model is considered most accurate when applied to the loading curve when using AFM based systems [67]. The analysis tool built into the Asylum MFP-3D software package (v. 31) was utilized for all regression analyses.

2.2.7. Dielectric Relaxation Spectroscopy

Dielectric Relaxation Spectroscopy (DRS) was used to determine the ionic conductivity of the biocomposites made with different compositions and coagulation agents and was performed at the University of Pennsylvania. The film was placed between two stainless steel electrodes, the top plate having a diameter of 6 mm, and then placed in a Janis VPF-100 cryostat under vacuum [68]. Solartron Modulab XM materials test system was utilized in a temperature range of 300 K – 450 K (26.85 – 176.85 °C), with the measurements starting at 450 K to ensure no excess water remained in the biocomposite. Also, the samples were tested over a frequency range of 0.1 Hz to 1 MHz [68]. After each measurement, the temperature was decreased by 10 K.

2.3. **Results and Discussion**

Morphological, thermal, mechanical, and ionic conductivity differences are demonstrated in the qualitative and quantitative data obtained by varying the coagulation agents as well as biopolymer ratios. Films regenerated with a higher percentage of cellulose were less flexible than those with more silk. Morphological differences correlated with changes in secondary structure calculations, mechanical properties, as well as ionic conductivity, and are illustrated in the following characterization tests.

2.3.1. Fourier Transform Infrared Spectroscopy

FTIR was used to identify secondary protein structures within the regenerated biomaterial films, and to ensure proper blending. **Figure 2.1** shows the normalized IR spectra of the six biopolymer films. The spectra were normalized to easily locate the various functional groups within the samples, as well as to compare peak linewidth. In nearly all of the spectra, the two most pronounced peaks can be seen at approximately 1030 cm^{-1} and from 3550 to 3000 cm^{-1}, which are stretching modes corresponding to C-O and O-H functional groups, respectively, found in cellulose. All of the spectra corresponding to the films coagulated with 1 and 10% ethanol look very similar in terms of peak breadth as well as the presence of different functional groups. Specifically, these four biocomposites contain the amide I and II regions, labeled in the first spectrum in **Figure 2.1**. Furthermore, they all have a small shoulder peak at approximately 1160 cm^{-1}, which corresponds to the C-N stretch in an imidazolium ring from the ionic liquid. Since this peak is small and not very pronounced, it is possible there may be only a small amount of residual ionic liquid leftover in the system after using the coagulation agent.

Compared to the other four spectra, there are noticeable differences seen in the 100% regenerated cellulose and silk spectra. The amide regions are very pronounced in the 100% regenerated silk film, and the N-H stretch peak is also very pronounced. This is seen in the FTIR spectra of pure *Bombyx mori* silk fibroin (not shown) and is related to the amine group. When looking at the 100% regenerated cellulose spectrum compared to those of the four mixed films, it looks very different. Specifically, the C-O peak is much more pronounced than in the other films, and the O-H peak is also more distinct. This spectrum looks more similar to the silk/cellulose biocomposites than the 100% regenerated silk spectrum does.

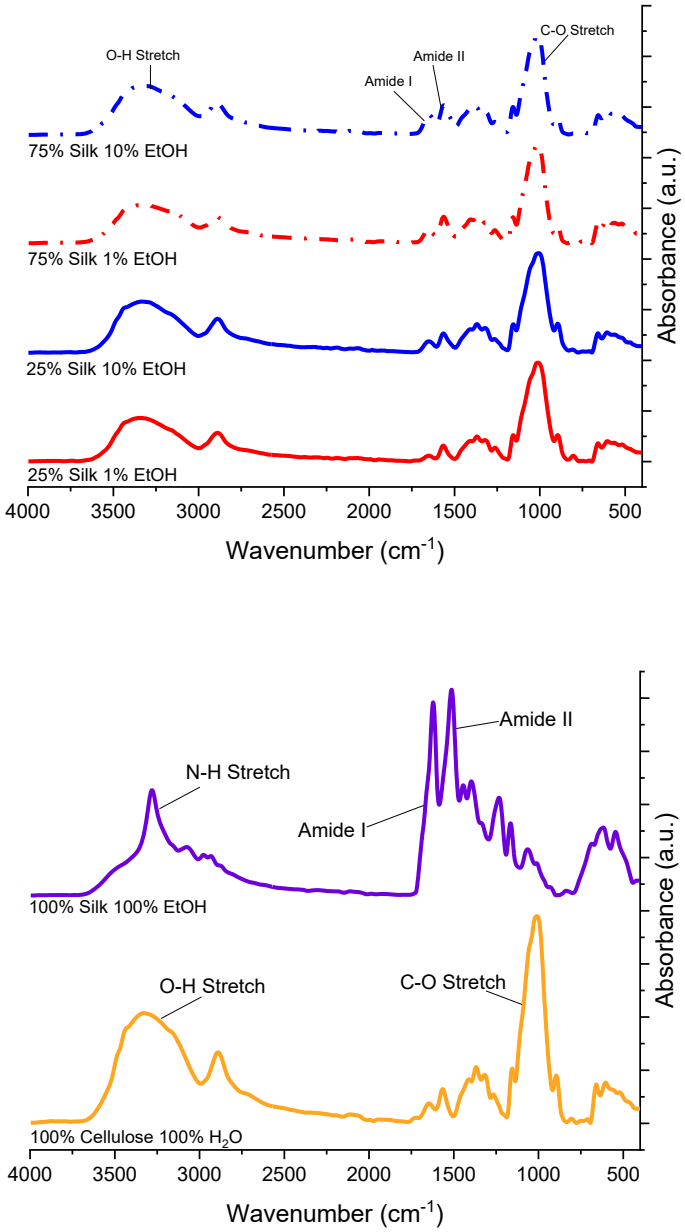

Figure 2.1. *FTIR spectra of regenerated silk and cellulose samples, as well as silk/cellulose biocomposites with varying composition ratios and coagulation agents.*

The amide I region was analyzed from 1705 cm^{-1} to 1595 cm^{-1} using Fourier Self-Deconvolution [69], and the secondary structure content from this analysis is summarized in

Table 2.1. When looking at all five secondary structure types, it is clear that the side chains vary the least between all samples, specifically by only 5.27%. This is followed by turns that differ by a maximum of 10.48% and then alpha helices, which vary by 11.47%. Random coils had a slightly higher percentage of change, with 23.47% difference between the 100% regenerated silk film and 25% silk film coagulated with 1% ethanol. Finally, β-sheet content differed by the highest percentage, with there being a 32.74% difference between the 100% regenerated silk film and 25% silk film coagulated with 1% ethanol. If the silk/cellulose biocomposite films are compared without the 100% regenerated silk film, there are no drastic differences in secondary structures. The only secondary structure that varies more than the others is the random coils due to the 25% silk coagulated with 1% ethanol sample having a higher percentage of approximately 39% compared to the other mixtures. If the 100% silk film is used for comparison purposes, it is interesting to see that in three of the five secondary structures, this sample had the lowest percentage when compared to the mixed films. The sample was only greater in side chains and β-sheets when compared to the other biocomposites. The increase in β-sheet content was expected since this film was not only made of 100% silk but was also coagulated with 100% ethanol, which is shown to increase β-sheet content as a function of percentage [7]. β-sheet content differs between all of the samples listed in **Table 2.1** and is also connected to the ionic conductivity, which is discussed in a later section. When looking at the different ratios, the 75% silk samples have higher β-sheet content compared to the 25% silk samples. This may be a result of these samples having a higher silk content, although the percentages are not drastically higher than the 25% silk samples. When looking at the differences in β-sheet content between the samples of the same composition, the 75% silk films have less of a

difference than the 25% silk films. The changes in this particular secondary structure are fascinating when correlating it with ionic conductivity.

Table 2.1. *Secondary structure contents of the 100% regenerated silk sample, and 25% silk and 75% silk biocomposites.*

Composition	***Coagulation***	***Side Chains***	***β-Sheets***	***Random Coils***	***Alpha Helices***	***Turns***
75/25 Silk-Cellulose	10% EtOH	0.92%	20.56%	29.16%	18.37%	30.98%
75/25 Silk-Cellulose	1% EtOH	0.44%	18.24%	27.14%	22.40%	31.77%
25/75 Silk-Cellulose	10% EtOH	1.08%	17.12%	33.36%	19.42%	29.02%
25/75 Silk-Cellulose	1% EtOH	1.04%	13.97%	38.83%	17.27%	28.89%
100 Silk	100% EtOH	5.71%	46.71%	15.36%	10.93%	21.29%

2.3.2. Scanning Electron Microscopy

Topographical and morphological properties of the regenerated silk/cellulose biocomposites seen in **Figure 2.2** were studied using Scanning Electron Microscopy (SEM). All films, except for the 100% silk film, generally look very similar to one another at the surface level. Both films coagulated with 10% ethanol look almost entirely smooth on the surface, with the 75% silk film only showing one distinct ridge running along the bottom right corner of the imaged surface. The films coagulated with 1% ethanol look slightly different. The 75% silk film has slight ridges running across the entire surface of the film, while the 25% silk film demonstrates areas with small bumps and a few shallow spheres. In comparison to both films coagulated with 10% ethanol, the films coagulated

with 1% ethanol are not as smooth and uniform on the surface. When looking at the films created with only one polymer, the 100% cellulose film looks relatively smooth, but also contains small bumps or pinholes on the surface. Compared to all the other films, the 100% silk film is the most dissimilar. This is apparent in the image presented where striations are along the entire surface of the film, and the silk fibers are visible throughout. It also looks as if there are fine cracks on the surface. The effect of various biopolymer ratios, as well as coagulation agents on the topography of the films, is evident when looking at these images presented in **Figure 2.2**.

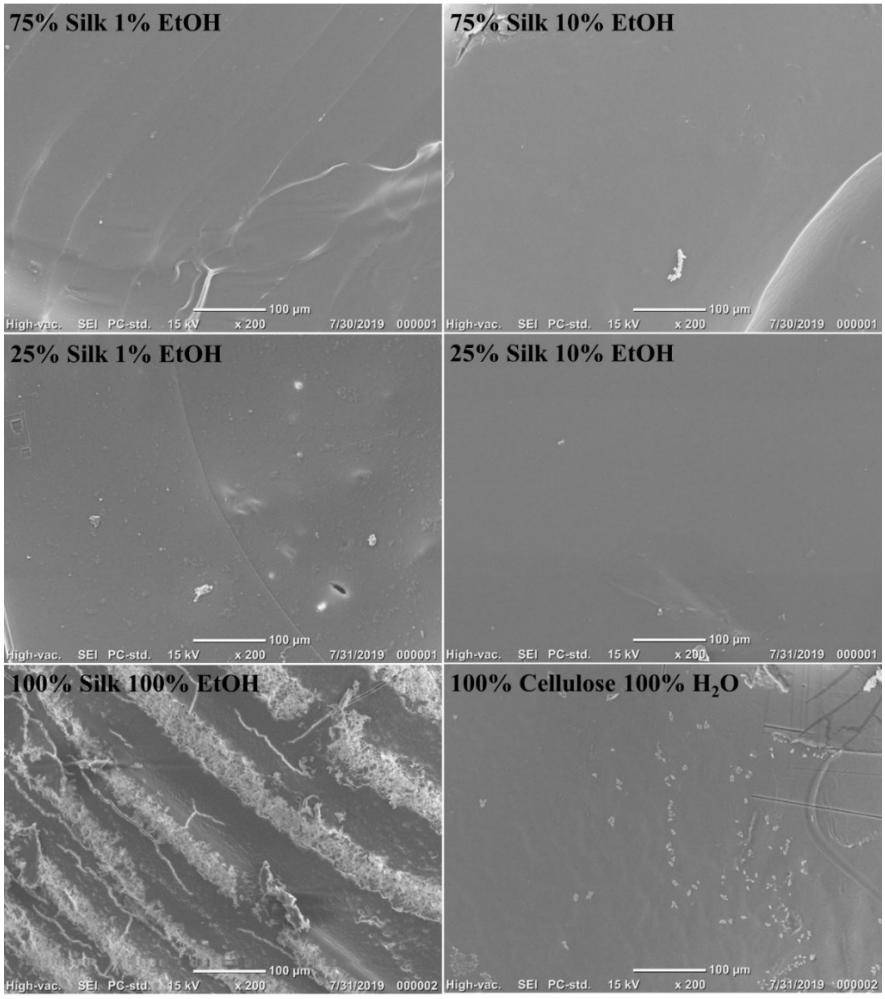

Figure 2.2. *SEM images of 100% regenerated films and varied biopolymer ratio samples using various coagulation agents.*

2.3.3. Thermogravimetric Analysis

The thermograms obtained from TGA analysis of six different biopolymer films are displayed in **Figure 2.3**. **Figure 2.4** differs in that it demonstrates the derivate weight-loss percentage thermograms, which help determine crucial thermal stability statistics shown in the biocomposites such as the onset and end temperatures, weight-loss percentage, and $T_{\Delta Max}$. Utilizing both **Figure 2.3** and **Figure 2.4**, the resulting values from these analyses are displayed in **Table 2.2**. First, looking at the 100% regenerated silk and cellulose films in **Figure 2.4**, it is clear that the 100% silk film demonstrates a single peak thermogram compared to the 100% cellulose film, which shows a trimodal thermogram. As a result, the silk film most likely has fewer interfaces than the cellulose sample [43]. When looking at the onset, end, and $T_{\Delta Max}$ temperatures of these two samples, it is seen that the silk film has an overall higher thermal stability than the cellulose film. The 100% regenerated silk film has a higher onset temperature by 31.6 °C, higher end temperature by 10.4 °C, lower weight percent loss by 11.26%, and only one $T_{\Delta Max,}$ which corresponds to only one peak and therefore fewer interfaces. When comparing the four mixed biocomposite samples, it is interesting to see a slight pattern in the thermograms in **Figure 2.4**. The two films composed of 75% silk, the higher percentage biopolymer in the film, only have two peaks, meaning it is a bimodal thermogram. This differs from the films with 25% silk, the lesser percentage compared to cellulose, which have three peaks, meaning it is a trimodal thermogram. As the silk content is decreased and the cellulose content increased, making it the dominant biopolymer in the system, the thermograms follow the same trend, deviating from the single peak to the three peaks, similar to the 100% regenerated cellulose sample, as expected. When studying the onset, end, and weight-loss

percentages of these four films, subtle differences are observed. The 75% silk film coagulated with 1% ethanol has the lowest onset temperature compared to the other three samples, specifically 12 °C lower than the highest onset temperature in 75% silk coagulated with 10% ethanol. The 25% silk coagulated with 10% ethanol sample has the lowest end temperature when compared with the other three mixed biocomposites. Also, all weight-loss percentages are nearly the same except for the 25% silk film coagulated with 10% ethanol, which is 2.00% less than the highest weight-loss percentage of the mixed samples. These results show how the thermal stability of the biocomposites changes as a function of not only composition but also coagulation agents. When the composition is changed, the results of sample analyses tend to fall more in line with the dominant polymer.

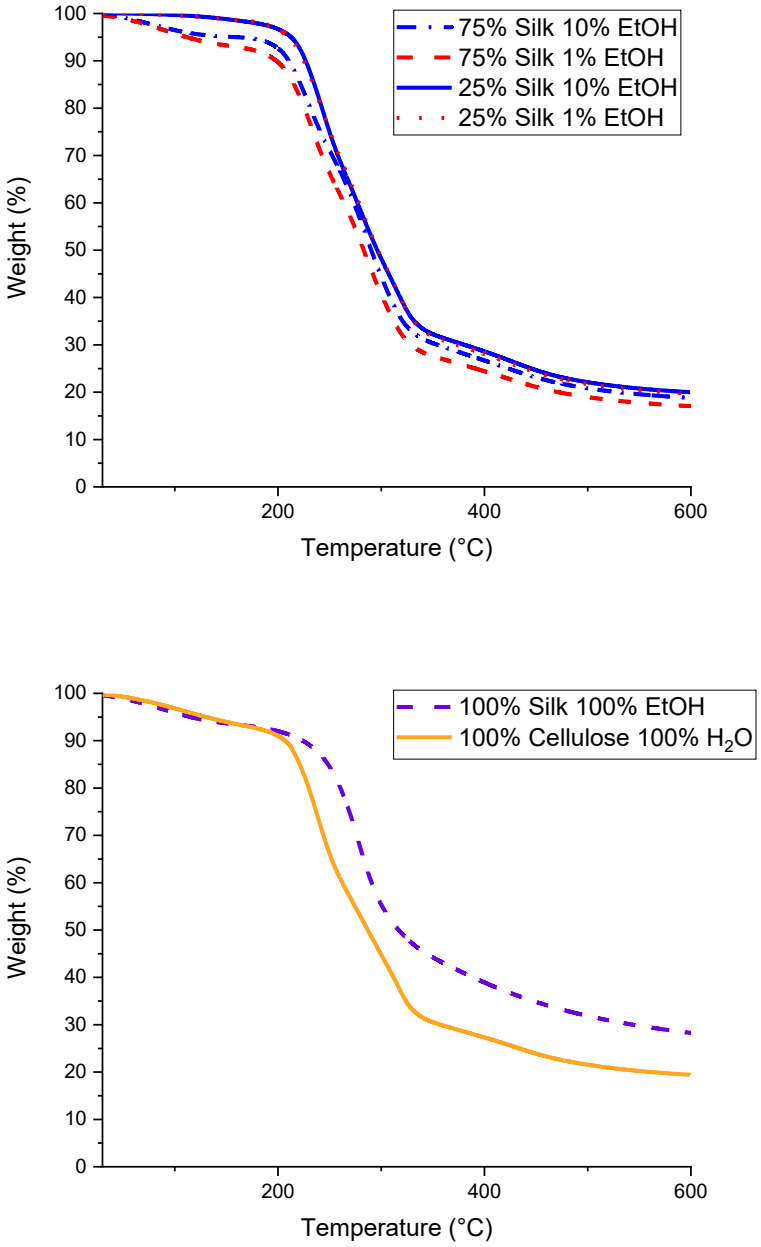

Figure 2.3. *Thermograms of silk/cellulose biocomposites with varied compositions and 100% regenerated samples.*

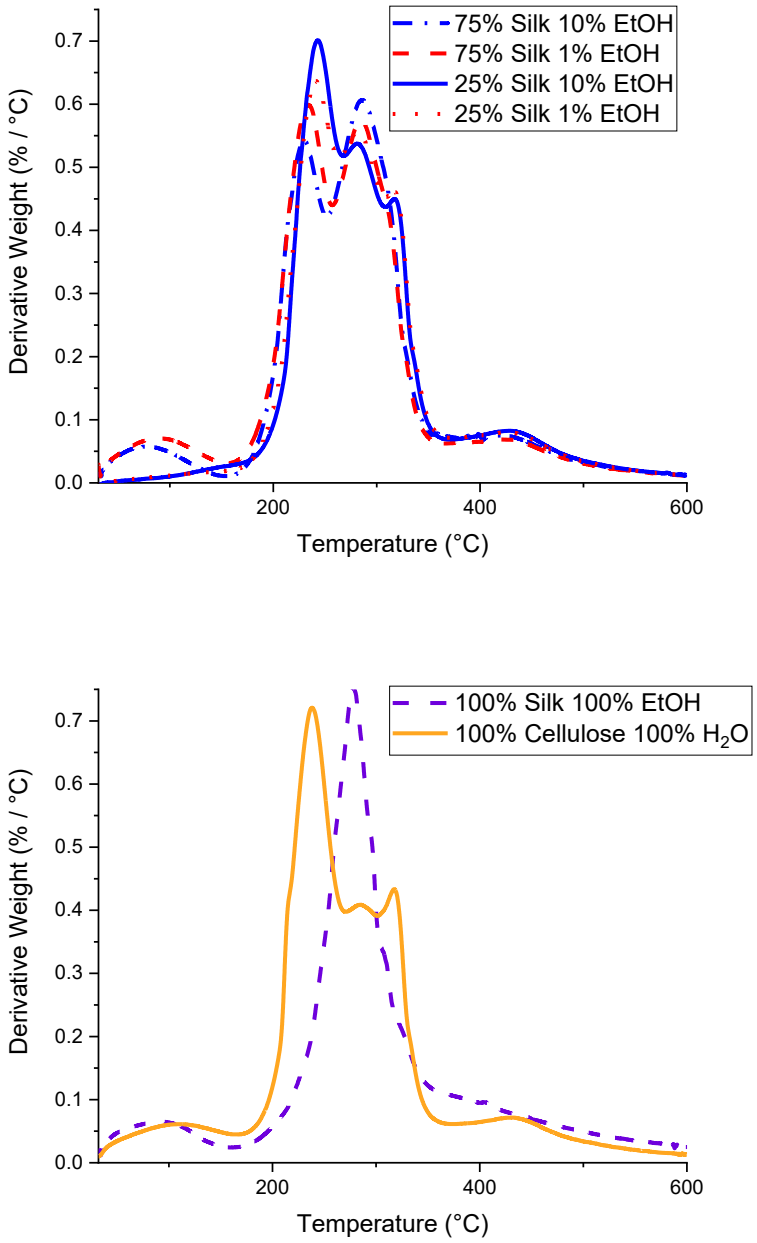

Figure 2.4. *Derivative weight-loss percentage plots of the varied composition biocomposite films as well as 100% regenerated samples, used to determine* $T_{\Delta Max}$ *as well as other characteristic temperatures.*

Table 2.2. *Start and end temperatures, total weight-loss percentage, and the maximum temperature of the derivative are used to characterize TGA results of the 100% regenerated samples and varied composition samples.*

Composition	**Coagulation**	T_{Onset} (°C)	T_{End} (°C)	*Wt. Loss (%)*	$T_{\Delta Max}$ (°C)
75/25 Silk-Cellulose	10% EtOH	225.8	319.6	67.95	229.5, 285.8
75/25 Silk-Cellulose	1% EtOH	213.8	310.2	67.63	233.4, 285.0
25/75 Silk-Cellulose	10% EtOH	223.4	305.6	65.95	243.3, 281.2, 317.0
25/75 Silk-Cellulose	1% EtOH	219.2	314.5	67.86	240.9, 280.7, 316.9
100 Silk	100% EtOH	251.5	305.4	53.48	278.1
100 Cellulose	100% H_2O	219.9	295.0	64.74	238.2, 285.3, 317.5

2.3.4. Differential Scanning Calorimetry

Standard DSC scans for all six samples of either uniform or varying biopolymer percentages are shown in **Figure 2.5**. It is interesting to see the crystallization peaks match up relatively closely among the same composition. For example, the crystallization peak for the 75% silk film coagulated with 10% ethanol seems to be around approximately the same temperature as the 75% silk film coagulated with 1% ethanol. This trend holds for the 25% silk samples as well. The 75% silk 10% ethanol sample has this peak at approximately 241 °C compared to 244 °C for the 75% silk 1% ethanol sample. The 25% silk samples both have their peaks at about 256 °C. These peaks are slightly shifted higher in temperature from the 75% silk films. The 100% regenerated cellulose sample has a crystallization peak at approximately 250 °C, but there is no observable crystallization peak

for the 100% silk sample. Instead, it contains an endothermic peak at around 269 °C, which could correspond to interface loss in the sample, including its degradation. In addition to observational comparisons, these DSC graphs were analyzed to determine the glass transition temperatures listed in **Table 2.3**. The 100% regenerated silk sample has the highest glass transition temperature compared to the other five samples, but not by a drastic amount. All samples seemed to have similar glass transition temperatures. This could be due to the coagulation agents in the different composition samples being only slightly different, enough to produce only subtle effects on the system. The 75% silk samples only differ by 0.52 °C, whereas the 25% silk samples have a more significant difference of 5.77 °C. In a later section, ionic conductivity data is normalized using these glass transition temperatures.

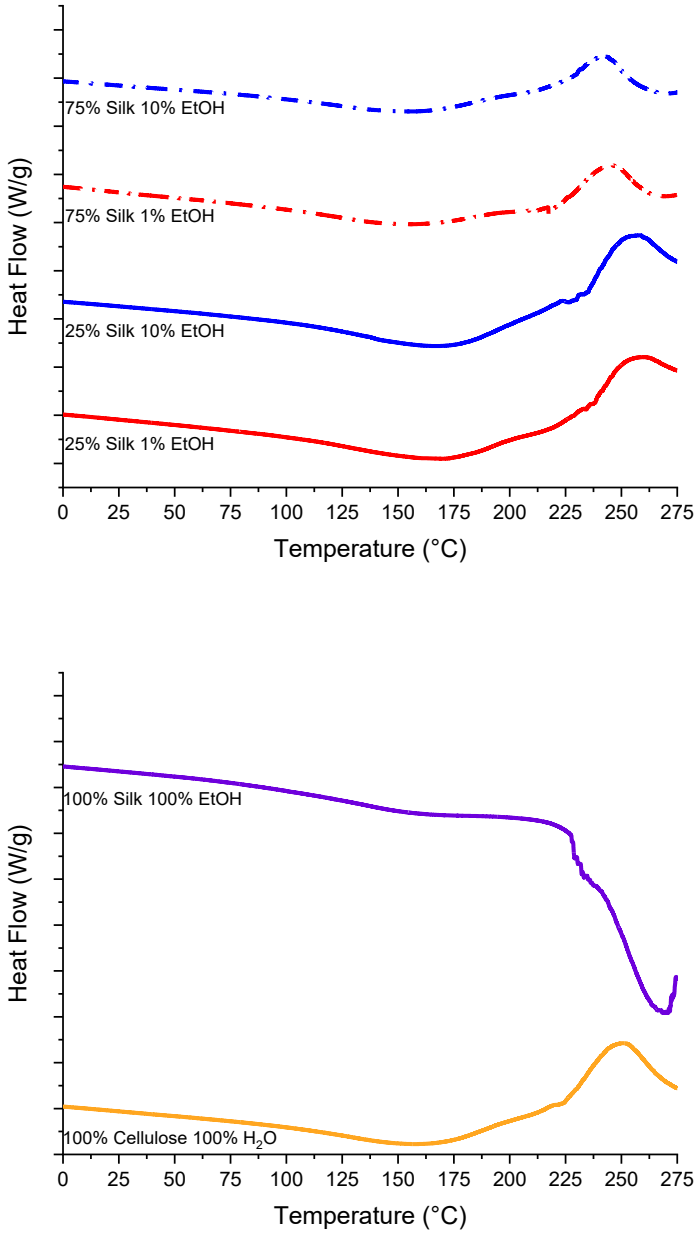

Figure 2.5. *DSC heat flow scans of the varied composition silk/cellulose biocomposite films and 100% regenerated samples used to determine the glass transition temperatures.*

Table 2.3. *Glass transition temperatures of varied composition films and 100% regenerated samples, determined by DSC in degrees Celsius and Kelvin.*

Composition	***Coagulation***	***T_g (°C)***	***T_g (K)***
75/25 Silk-Cellulose	10% EtOH	128.58	401.73
75/25 Silk-Cellulose	1% EtOH	129.10	402.25
25/75 Silk-Cellulose	10% EtOH	133.07	406.22
25/75 Silk-Cellulose	1% EtOH	127.30	400.45
100 Silk	100% EtOH	137.98	411.13
100 Cellulose	100% H_2O	128.68	401.83

2.3.5. X-ray Scattering

Figure 2.6 shows the X-ray scattering curves for regenerated pure samples and four biocomposites coagulated in two coagulation agents. The scattering vector and correlation distances for all six samples are recorded in **Table 2.4** and **Table 2.5**. For 100% regenerated silk in water, the scattering profile shows six scattering peaks. Within the various scattering peaks, the scattering vector, q_a = 5.46 nm^{-1}, corresponds to the average of both inter-sheet distances between β-sheets and the size of the β-sheets in the lateral direction. The correlation distance (*d*-spacing) for this peak is calculated by using the $d=2\pi/q$ formula and was found to be equal to 1.16 nm. The broadness of this peak extended from 2.96 to 8.16 nm^{-1} (0.77 to 2.12 nm). The scattering peaks at 14.45, 17.67, 22.52, 28.66, and 31.40 nm^{-1} correspond to the correlation distances between β-strands and primary structure, especially the silk II crystalline spacings as a result of being modified during dissolution and regeneration [70-76]. In the 100% regenerated cellulose sample, seven scattering peaks are

observed. The first scattering peak is the nanophase separation related to the microfibril located at a scattering vector of q_g = 1.31 (4.80 nm). The cellulose crystallite lateral size is located at q_h = 8.78 (0.72 nm) and the monoclinic unit cell of cellulose I_β equatorial lattice planes and its periodicity (14.32, 15.66, 20.56, 24.9 and 29.6 nm^{-1}). The correlation distances for these scattering vectors are 0.44, 0.40, 0.30, 0.25 and 0.21 nm [77-81].

The scattering profiles for the biocomposite samples are also located in **Figure 2.6**. The 2D scattering profiles (not shown here) showed isotropic rings for all biocomposites. **Table 2.5** shows each scattering vector with its correlation distance. Qualitatively, the X-ray scattering profiles are very similar for each biocomposite. Only slight changes are observed as a function of increasing silk content. For example, the scattering peak located at q_1 = 8.45 nm^{-1} increases to 8.83 nm^{-1} as the silk content increases. Also, the broadness of this peak increases. This means that the spacing in between the silk and cellulose carbon chain domains, which is related to the molecular intercalation, increases from 0.71 to 0.75 nm [62]. There is no observable change as a function of the coagulation agent. Interestingly, the higher scattering vector region does not show any nanophase separation. All X-ray scattering profiles show a 45-degree curve. This could mean that the overall system might be separated by distinct interfaces, as similarly reported in the TGA section. The scattering vectors q_2, q_3, q_4, *and* q_5, are related to the cellulose unit cell spacing and the distance between silk β-strands; this region includes the silk I spacings which is a mixture of alpha-helices, β-sheets, and random coils. As expected, as the silk content increases, the sharpness of these peaks also increases.

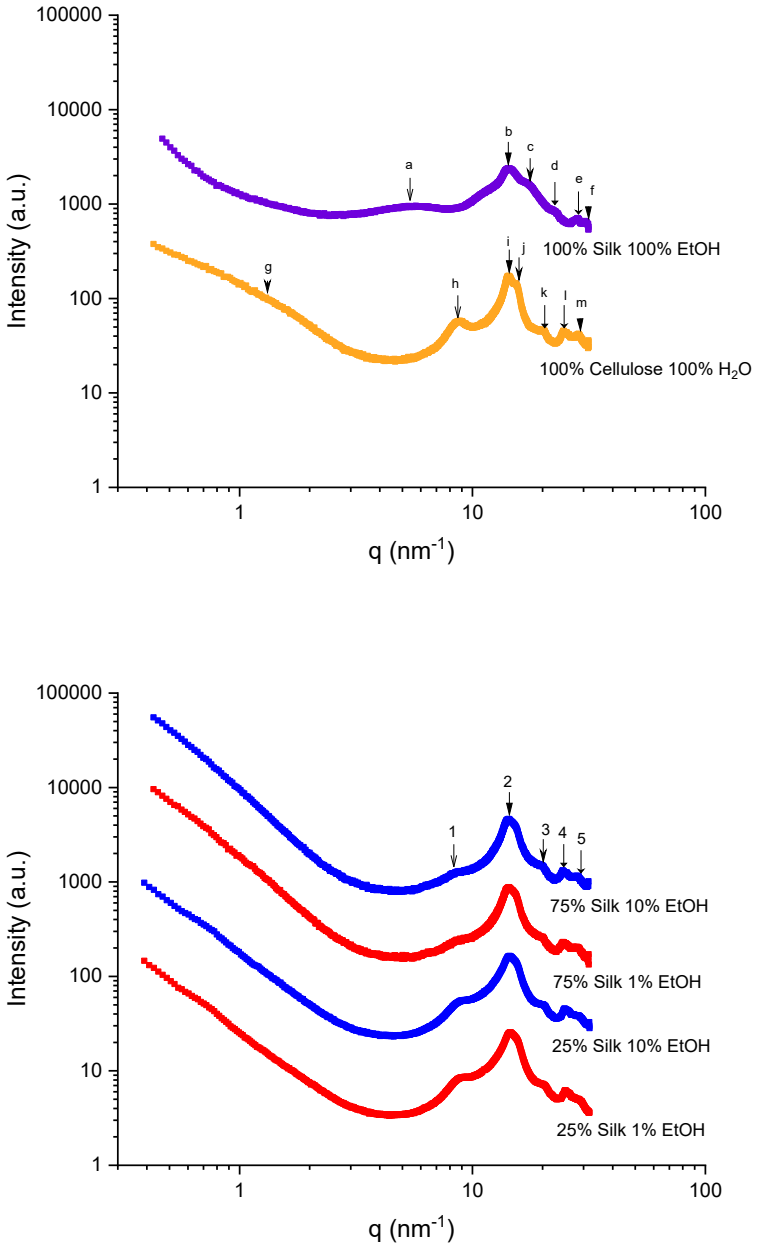

Figure 2.6. *X-ray scattering profiles for 100% regenerated silk and cellulose samples and varied composition biocomposites.*

Table 2.4. *Scattering vector and correlation distances for regenerated 100% cellulose and 100% silk samples coagulated with water and ethanol, respectively.*

Peak Position	**q (nm^{-1}) d (nm)**	Sample	Peak Position	**q (nm^{-1}) d (nm)**	Sample
a	5.42 1.16	Regenerated 100% Silk	g	1.31 4.80	Regenerated 100% Cellulose
b	14.45 0.44		h	8.78 0.72	
c	17.67 0.36		i	14.32 0.44	
d	22.52 0.28		j	15.66 0.40	
e	28.66 0.22		k	20.56 0.30	
f	31.40 0.20		l	24.9 0.25	
			m	29.66 0.21	

Table 2.5. *Scattering vector and correlation distances for two varied composition silk/cellulose biocomposites coagulated with two different coagulation agents.*

Peak Position	**q (nm^{-1}) d (nm)**			
	25/75 Silk-Cellulose		75/25 Silk-Cellulose	
	1% EtOH	10% EtOH	1% EtOH	10% EtOH
1	**8.83 0.71**	**8.83 0.71**	**8.40 0.75**	**8.40 0.75**
2	14.40 0.44	14.40 0.44	14.40 0.44	14.40 0.44
3	20.27 0.31	20.27 0.31	20.27 0.31	20.27 0.31
4	**25.15 0.25**	**25.15 0.25**	**24.79 0.23**	**24.79 0.23**
5	29.43 0.21	29.43 0.21	29.43 0.21	29.43 0.21

2.3.6. Atomic Force Microscopy (Nanoindentation)

The elastic modulus of silk/cellulose biocomposites of 25% and 75% silk were measured at 120 °C (near the glass transition temperature) and determined by fitting the load-indentation curves to the JKR model. In samples of both compositions of silk and cellulose, the elastic modulus increases as the percentage of ethanol is increased from 1% to 10%, as seen in **Figure 2.7**. The samples of 25% silk show an increase in the mean elastic modulus from 26 MPa to 676 MPa, while the 75% silk samples show an increase from 163 MPa to 362 MPa.

It is interesting to note that the coagulation bath, which has the two highest onset temperatures in TGA, also has a higher elastic modulus. These are both the 10% ethanol samples of 25% silk and 75% silk with onset temperatures of 223.4 °C and 225.8 °C, respectively. Also, certain determining factors of conductivity relate to these mechanical properties. This includes β-sheet content and semicrystallinity of cellulose, due to cellulose content. First, it is seen that the coagulant with higher β-sheet content in each ratio has a higher elastic modulus. When comparing both 25% silk samples, the 10% ethanol sample has a higher β-sheet content and ultimately has a higher elastic modulus. When looking at both 75% silk samples, the 10% ethanol sample also has a higher β-sheet content, and again a higher elastic modulus. β-sheets are considered to be semicrystalline regions within the silk fiber, so this would make sense; as the β-sheets increase, the elastic modulus does as well, resulting in less flexible and more rigid samples.

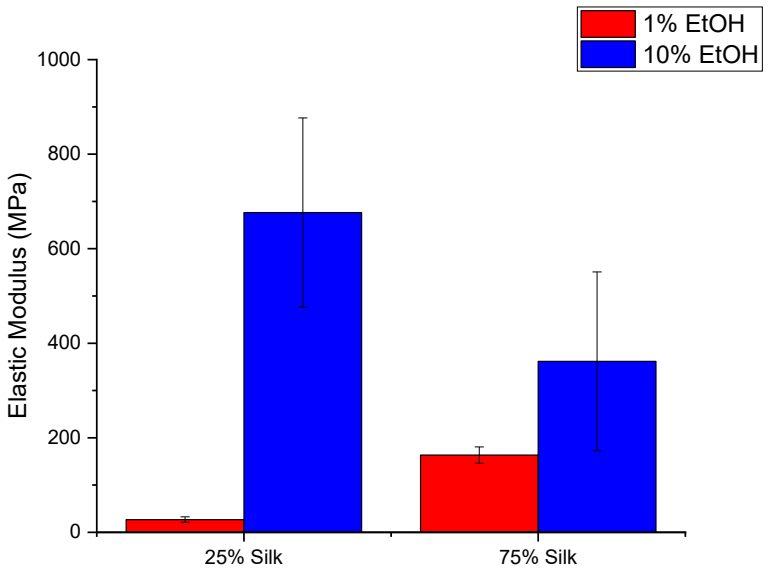

Figure 2.7. *The elastic modulus of the two sets of varied composition silk/cellulose biocomposites coagulated with two different percentages of ethanol.*

2.3.7. Dielectric Relaxation Spectroscopy

The ionic conductivities of the six different samples calculated at various temperatures are shown in **Figure 2.8**. A negative slope indicates that conductivity increases with temperature. The ionic conductivity was calculated from the measured resistance and physical dimensions of the sample by the following relationship, $\sigma = {}^{L}/_{AR}$; where σ is the ionic conductivity, L is the distance between the two inner electrodes, A is the cross-sectional area of the polymer film, and R is the resistance at each temperature calculated using the Nyquist plot. When creating this plot, there will be a semicircle with two *x*-intercepts, one at lower values on the *x*-axis versus higher values. In this case, the *x*-intercept at the high value on the *x*-axis is equal to the resistance [51]. Looking at **Figure 2.8**, the ionic conductivity of the 75% silk film coagulated with 10% ethanol is highest,

followed by 75% silk coagulated with 1% ethanol, 25% silk coagulated with 1% ethanol and finally 25% silk coagulated with 10% ethanol. The trend in this data can be explained with not only β-sheet content but also X-ray scattering data and elastic modulus measurements obtained from AFM. First, it was previously discussed that higher β-sheet content corresponded to higher ionic conductivity [50, 62]. Although, in general, this may be true, the conductivity is not just a function of β-sheet content but also other morphological properties, and therefore these samples do not strictly obey this rule. The 75% silk film coagulated with 10% ethanol does have the highest β-sheet content with 20.56%, and this is followed by the 75% silk film coagulated with 1% ethanol with 18.24%. The film with the next lowest ionic conductivity based on β-sheet content should be the 25% silk film coagulated with 10% ethanol, which has a β-sheet content of 17.12%. However, this is not the case since this sample has the lowest ionic conductivity. As a result, these observations may be described by the relative silk and cellulose content. In **Figure 2.8** containing the 100% regenerated silk and cellulose samples, it is seen silk is more conductive than cellulose. As a result, when silk dominates in the mixture, the β-sheet content is the determining factor in ionic conductivity. Also, when looking at the 75% silk samples, the sample coagulated with 10% ethanol has a higher conductivity, as well as a higher elastic modulus as compared to 1% ethanol, meaning the sample is more rigid. One would expect this would lead to a decrease in conductivity, possibly due to the decrease in segmental motion within the sample, but the opposite is observed [82]. This may be because the mechanical properties are not as crucial in a sample where silk dominates. Instead, the β-sheet content becomes more critical in determining conductivity trends.

When cellulose dominates in the film, this is not the case, and instead, cellulose semicrystallinity may play an important part as well as mechanical properties. It is essential to note the 75% silk samples follow the β-sheet content trend, but the 25% silk samples are flipped, meaning the 1% ethanol film with only 13.97% β-sheets has a higher ionic conductivity than the film coagulated with 10% ethanol and 17.12% β-sheets. When silk is the dominant component in the mixture, better ionic conductivity is seen compared to samples where cellulose dominates. It is also interesting to note that 25% silk films are more semicrystalline, according to the X-ray scattering profiles in **Figure 2.6**. Another possibility is due to an increase in spacing (from 0.71 to 0.75 nm) between the silk and cellulose carbon chains as a function of silk content. This increase in spacing can cause an increase in segmental motion resulting in higher ionic conductivity. For this reason, one could assume this becomes a more critical aspect of morphology in determining conductivity than β-sheet content, perhaps. Also, as discussed in the previous section, the elastic modulus may be an important property that drives the conductivity trend. When looking at the 25% silk samples, the sample coagulated with 10% ethanol has a higher elastic modulus, but a lower conductivity compared to the 1% ethanol sample. This may be due to the fact that since silk does not dominate, and rather cellulose does, the β-sheet content is no longer the only driving factor in conductivity. Instead, the mechanical properties are more critical. The film, which has a higher elastic modulus, more rigidity, and less flexibility, has lower ionic conductivity compared to the opposite. This makes sense as it would be more difficult for ions to move throughout a film where there is less flexibility. It is interesting to see how the composition changes factors that ultimately impact ionic conductivity. The findings suggest that when more silk is present, β-sheet

content is the more important characteristic, but when more cellulose is present, β-sheet content does not dictate, and rather mechanical properties do.

Because the glass transition temperatures are very similar for all samples in this study, the use of a T_g-normalized graph is not necessary since it would show nearly the same pattern as **Figure 2.8**. According to Ye et al., this T_g-normalized graph is important in determining the effect morphology has on the system, if any [83]. If all data points from each sample collapse onto one line, this would mean the only contributing factor in the system for ionic conductivity was the glass transition temperature. However, since this is not observed in **Figure 2.8**, it can be assumed other contributing factors are affecting the ionic conductivity [83]. These factors can include morphology, which would affect the segmental motion of the polymer chains or ion hopping within the system [50-51]. As discussed previously, the data suggests samples with higher silk content follow the β-sheet content trend formerly addressed in two other papers, including a recent publication by Pereira et al. [50], which suggested β-sheets enhanced ion mobility. Also, the samples containing a higher content of cellulose exhibited higher cellulose semicrystallinity and followed the same trend as seen in the elastic modulus of the samples. Similarly, it can be observed for the 100% regenerated samples. This data combined suggests there is a strong correlation between the ionic conductivity and morphology of the systems, as illustrated in **Figure 2.9**. This schematic helps to illustrate why there is a difference in conductivity. When there is a higher silk content, resulting in less semicrystallinity of the polysaccharide, the ions can take a more direct path with fewer steps, resulting in ions moving more efficiently and faster through the solid biocomposite, which also results in higher conductivity. However, the opposite is true when there is lower silk content. In this

biocomposite, there are more semicrystalline regions, and as a result, the ions cannot take a direct path like in the 75% silk films. This results in a slower movement of ions and a lower conductivity.

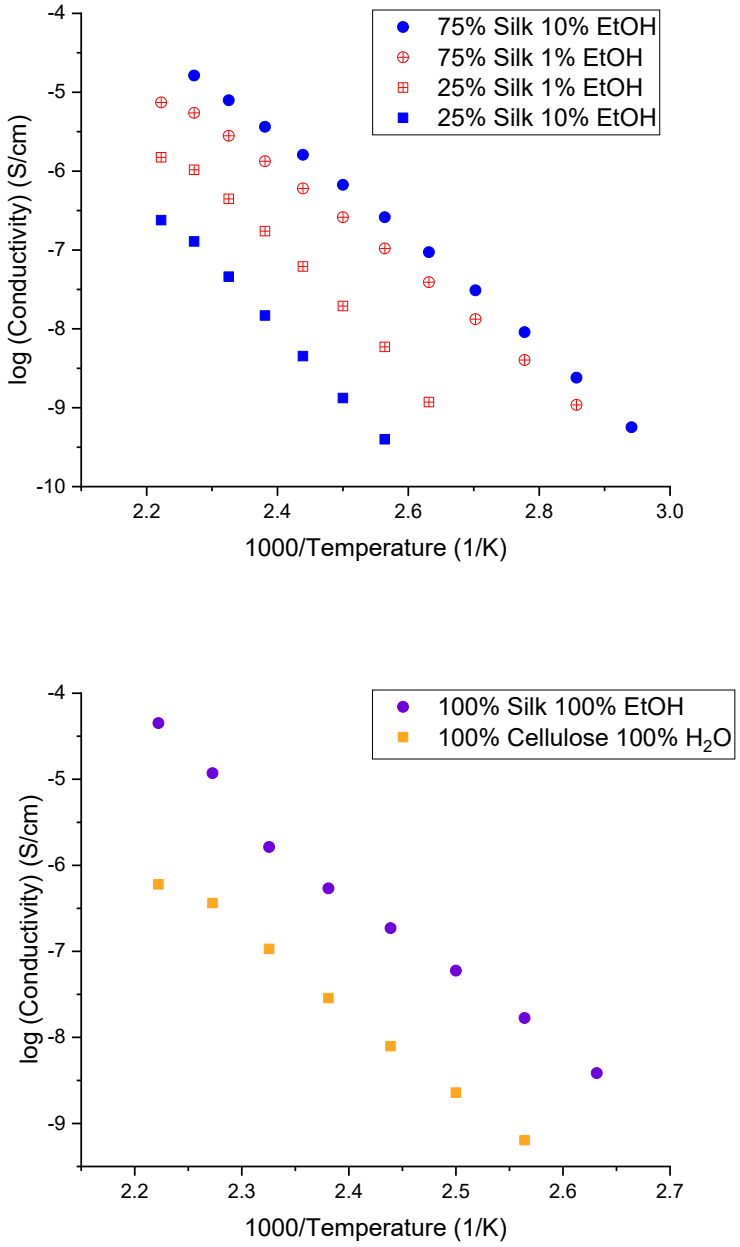

Figure 2.8. *Ionic conductivity versus temperature of the two sets of varied composition silk/cellulose biocomposites as well as 100% regenerated silk, and 100% regenerated cellulose samples.*

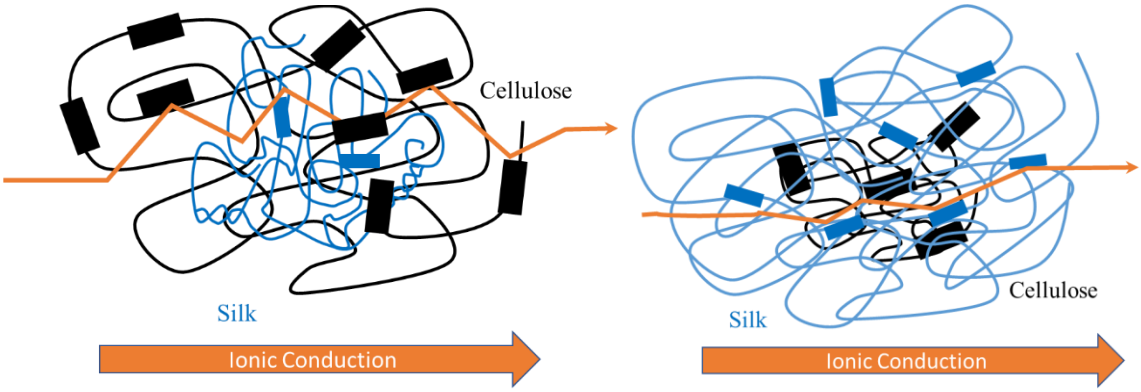

Figure 2.9. *Schematic representation of ion diffusion in a solid electrolyte based on two different compositions of silk/cellulose biocomposites. The left represents 25% silk, and the right represents 75% silk.*

2.4. Conclusion

Systematic variation of silk/cellulose ratios and coagulation agents provided evidence to suggest a direct relationship between ionic conductivity and morphology. Specifically, the morphological, thermal, mechanical, and ionic conductivity properties of the samples were altered. Secondary structure differences are seen as results of FTIR, with the two samples coagulated with 10% ethanol having the highest β-sheet content among compositions, followed by the 1% ethanol samples. When investigating thermal properties, it is seen that the 100% regenerated silk sample has the highest thermal stability in terms of its onset temperature, end temperature, and weight-loss percentage. The other samples all had very similar onset temperatures as well as weight-loss percentages. It was interesting to see that when the composition varied, the thermogram showed a tendency to have a comparable number of peaks to the dominating biopolymer. Films where cellulose dominated showed a trimodal thermogram, similar to the 100% regenerated cellulose film, and films with more silk showed a bimodal thermogram, which was one peak more than

the single peaked thermogram seen in the 100% regenerated silk sample. This illustrates the influence of composition on the system. Glass transition temperatures obtained from DSC were all very similar. This could be explained since all the films other than the regenerated samples were coagulated with similar percentages of coagulants. Changes of 1 to 10% may not have been drastic enough to see significant differences in this data. In addition, X-ray scattering data showed samples with only 25% silk and 75% cellulose were more semicrystalline than those with a higher percentage of silk. This suggests the semicrystallinity of the system is affected by silk versus cellulose content. The nanoindentation results provided an interesting correlation between the elastic modulus of the materials and their ionic conductivity in which a higher elastic modulus corresponds to lower ionic conductivity in 25% silk samples. The results from X-ray scattering, AFM based nanoindentation, and FTIR correlate with the ionic conductivity of the silk/cellulose biocomposite films. The ionic conductivity related to not only β-sheet content but also the amount of silk or cellulose present. When silk was no longer the higher percentage, but rather the cellulose was, the β-sheet content was no longer the most influential factor in determining the order of ionic conductivity. Because cellulose was present in 75%, the semicrystallinity of the films was more important along with the elastic modulus and made it that the film with the higher β-sheet content from these two samples had a lower ionic conductivity. This demonstrates the effect of morphology on the system. When there is higher silk content, there are fewer semicrystalline regions from cellulose, and therefore ions can move more directly through the structure leading to higher conductivity. The opposite is true, where a higher cellulose content leads to more semicrystalline regions, not allowing ions to move as efficiently through the biocomposite. This leads to lower

conductivity. Future studies will need to be completed to investigate this trend further. However, this work demonstrates that ionic conductivity can be tuned for specific needs in biocomposite films, which may be necessary for modern materials science as well as medicine.

Chapter 3

Morphology and Ionic Conductivity Relationship in Silk/Cellulose Bio-composites

Previously published: Blessing, B.; Trout, C.; Morales, A.; Rybacki, K.; Love, S. A.; Lamoureux, G.; O'Malley, S. M.; Hu, X.; Salas-de la Cruz, D., Morphology and ionic conductivity relationship in silk/cellulose biocomposites. *Polymer International* **2019,** *68* (9), 1580-1590. This chapter has been published in Polymer International.

Copyright © 2019 by John Wiley & Sons, Inc. (Granted permission to use this material.)

3.1. Introduction

Recently, biomaterials have become of great importance in material sciences, medicine, and bioengineering [4-5]. The interest in this class of materials stems from its numerous advantageous properties that include abundance, biocompatibility, low cost, and tunable physical and morphological properties [25]. These materials have been used to create scaffolds for tissue growth as well as capsules used for drug delivery systems [5]. Creating implantable batteries using natural biomaterials has become significant in various medical applications [6]. Having the ability to control the properties of these biomaterial-based batteries, including morphological, thermal, and mechanical properties, is essential in creating devices that are minimally harmful in the human body and are advantageous in the medical field. In previous studies, it has been shown that the morphology of biocomposites can be changed as a function of ionic liquid and composition [25, 43, 45]. This is important because it can induce changes in physicochemical properties of the natural-based material, which can lead to specificity in application.

Biocomposites, from a mixture of proteins and polysaccharides, are ideal for creating bio-electrolyte membranes that can exhibit high biocompatibility in the human body and adjustable conductivity. One such protein includes *Bombyx mori* silk fibroin. It is produced by *Bombyx mori* silkworms in the form of fibers coated with sericin proteins with a repeat unit of $[GAGAGS]_n$ and properties, which include high toughness and tensile strength [7]. Within this protein, there are crystalline structures that can consist of β-sheet secondary structures. These secondary structures can be deliberately changed from alpha helices or random coils to β-sheets when using alcohol-based solutions [7, 11].

Among the materials used to form a composite with silk are polysaccharides such as cellulose. The *Bombyx mori* silk has amino acids with functional groups that are eligible to form hydrogen bonding with hydroxyl groups in microcrystalline Avicel cellulose. Cellulose is a natural biopolymer found in numerous sources, including plants, generally, in the form of cellulose I, and more rarely can be found (or regenerated) as cellulose II with anti-parallel sheets [16, 23]. Within cellulose, there is a complex hydrogen bonding network with intermolecular and intramolecular hydrogen bonds [13, 20]. The short-distance chain packing and stiffness of cellulose, partially from the complex hydrogen-bonding network, makes it challenging to break down and fully dissolve in common organic solvents or water [26]. Instead, ionic liquids are used to complete the dissolution process for cellulose and silk [26]. These ionic liquids have advantageous properties, including a wide electrochemical window, good thermal stability, and high ionic conductivity [29]. The ionic liquid cation and anion associate with the oxygen and hydrogen of the cellulose hydroxyl groups, respectively, disturbing hydrogen bonding and causing dissolution [26-27]. Silk chains will undergo a similar process. In solution, cellulose and silk will interact through electrostatic,

hydrogen bonding, and hydrophobic-hydrophobic interactions [25, 42]. After the dissolution, a coagulation agent such as water, hydrogen peroxide, or alcohol is added to wash out the ionic liquid. During this phase, the anions migrate from the biopolymer blend to the coagulant. Evidence for this is based upon the nearly complete absence of residual ionic liquid in the final blend, as seen through different technical characterizations such as Fourier transform infrared spectroscopy. As the anions are essential to keeping the biomolecules separated, the polymer chains can aggregate in their absence. However, the coagulation agent rapidly replaces the anions once embedded in or next to the biopolymers, so that there is competition between coagulant molecules and other biopolymers in forming hydrogen bonds. This leads to phase separation with the formation of a hydrogel (biopolymer and water) and a liquid phase (water and ionic liquid) [43]. The final step consists of the removal of the coagulation agent and the formation of the intercalated protein-polysaccharide solid biocomposite. Combining the protein blend with polysaccharides helps to enhance physicochemical properties [25].

When the materials are regenerated using different coagulation agents, the properties can vary in terms of morphological, thermal, and mechanical properties. These differences can also lead to changes in ionic conductivity. Two mechanisms, ion dissociation and ion diffusion, directly affect the ionic conductivity of homogeneous solid polymer electrolytes [46]. It is possible to calculate the ion diffusion process by the Vogel-Fulcher-Tammann (VFT) equation and the ion dissociation process by the Arrhenius equation [46]. The equation below gives the ionic conductivity [47],

$$\sigma = q\rho_{\infty}\mu_{\infty} exp\left(-\frac{E_a}{\bar{R}T}\right) exp\left(-\frac{B}{(T-T_0)}\right)$$

where q is the charge of the ions, ρ_∞ is the total ion density, μ_∞ is ion mobility, E_a is the activation energy, T is the temperature, $\bar{R}$ is the universal gas constant, B is an energy barrier constant, and T_0 is the Vogel temperature [46-48]. The ion diffusion process also includes the hopping of ions as well as the segmental motion of polymer chains [48-49, 84]. All of these processes are related to the morphology of the solid material, which can partially be expressed by the energy constant, B, in the above equation. According to the equation, $B = B_{seg} + B_h$, B can be written in terms of two contributions: B_h , the energy barrier of ion hopping and B_{seg}, the energy barrier for segmental motion. Therefore, it is possible to observe that this constant is directly related to changes in morphology [46]. As a result, when the morphology changes, it causes changes in B, which results in modifications in the ionic conductivity. A previous study in which silk fibroin separators were prepared showed data to suggest that higher β-sheet content is correlated with higher ionic conductivity [50]. Therefore, this study will investigate how the ionic conductivity of silk/cellulose biocomposites varies according to a change in the structural and morphological properties within the films.

In this study, 1-ethyl-3-methylimidazolium acetate (EMIMAc) and 1-ethyl-3-methylimidazolium chloride (EMIMCl) ionic liquids are used to dissolve the silk and cellulose biomaterials, which are then regenerated with aqueous solutions of either 25% hydrogen peroxide or 25% ethanol. The use of two different ionic liquids allows for the comparison of ionic conductivities based on changing just the anion in the ionic liquid structure. This small difference leads to morphological, thermal, mechanical, and electrical property variations. Also, morphological changes, as well as ionic conductivity modifications, are seen between the two coagulation agents. The focus of this study is to

determine how the formation of β-sheet and cellulose crystallinity, induced by the fabrication methods, dictates changes in the ionic conductivity of a 50% silk and 50% cellulose film.

3.2. Experimental Section

Materials

Ionic Liquid

1-Ethyl-3-methylimidazolium acetate (95%) and 1-Ethyl-3-methylimidazolium chloride (98%) were both purchased from Sigma-Aldrich. The ionic liquids were pretreated by placing them in a vacuum oven (30 inHg) at 50 °C for 24 hours to remove any water in the liquid.

Cellulose

Avicel microcrystalline cellulose pf 250 μm (Techware: Z26578-0) was acquired from Analtech. Before using the cellulose, it was placed in a vacuum oven (30 inHg) at 50 °C for 24 hours.

Silk

Bombyx mori silk cocoons were purchased from Treenway Silks (Lakewood, CO). The silkworm cocoons were boiled in a 0.02M $NaHCO_3$ (Sigma-Aldrich) solution for 15 minutes to remove the sericin coating on the fibers. Deionized water was used to thoroughly rinse the cocoon fibers three times to ensure the sericin was entirely removed.

The degummed fibers were air-dried overnight and then put into a vacuum oven (30 inHg) at room temperature. This removed moisture on the surface of the fibers.

Dissolution of the Protein and Polysaccharide

The protein, (silk), and polysaccharide, (cellulose), were measured to make up 10% by mass of the biocomposite film, while the ionic liquid was measured to make up the remaining 90% by mass. The 10% solid mass of the film was broken down, so silk and cellulose each account for 50% by mass. The two pretreated ionic liquids were measured into individual vials and placed into a silica oil bath on a hot plate at 80 °C. The bath was used to ensure there was an even amount of heat distributed to the vials. The silk was first added to the vial followed by the cellulose once silk dissolution was complete. When the dissolution of both silk and cellulose was completed for each ionic liquid, the solution was allowed to mix for 24 hours on the hot plate at the designated temperature.

Preparation of Regenerated Biofilm

The gel solution formed from the dissolution was transferred, after 24 hours, to 3-D printed molds made of polylactic acid with dimensions of 12 mm × 12 mm × 1 mm. Heated to 75 °C, 1 mL micropipette tips were used when pipetting the solution into the molds to ensure the solution did not solidify when transferring from vial to mold. The molds were placed in a 250 mL beaker filled with 100 mL of coagulation agent and sealed with parafilm for 48 hours to regenerate the materials and remove as much ionic liquid as possible from the film. After 48 hours, the molds were removed, rinsed three times with distilled water to ensure removal of residual ionic liquid, and transferred to a Teflon Petri

dish. Upon which, the films were placed in a low-pressure desiccator under 4 inHg of vacuum for 72 hours to allow drying.

Characterization

3.2.1. Scanning Electron Microscopy

Scanning Electron Microscopy (SEM) was performed using the JEOL JCM-6000 SEM, and images obtained from this were used to determine the topography of the films. Images were acquired with a magnification of 200x and presented with a scaling bar of 100 μm. The films were approximately 5 mm in width and put into a DII-29010SCTR Smart Coater at vacuum level 4 Pa to deposit a conductive film on the sample that mitigates the buildup of surface charge. Deposition of Au-Pt coating took place for 60 seconds, and then the samples were ready for imaging.

3.2.2. Fourier Transform Infrared Spectroscopy

Bruker's ALPHA-Platinum ATR-FTIR Spectrometer with Platinum-Diamond sample module was used to perform the Fourier Transform Infrared Spectroscopy (FTIR) analysis. 4000 cm^{-1} to 400 cm^{-1} was the spectra range used to collect data of the films. 128 background scans were performed along with 32 sample scans in 6 different locations of the film. Acetone was used to clean the FTIR diamond and hammer before the background scans were run, as well as between each sample. Fourier self-deconvolution was used to study the amide I region (1595 cm^{-1}-1705 cm^{-1}). The Lorentzian line shape, with a 26.4 cm^{-1} half-bandwidth and a noise reduction factor of 0.3, was used for performing deconvolution. Gaussian profiles were utilized to allow for fitting results and then

integrated to find the area relating to a specific wavelength. All analyses were performed using Opus 7.2 software. The data was normalized from 4000 cm^{-1} to 400 cm^{-1} using min-max normalization. This was used to show functional groups in the spectra better.

3.2.3. Thermogravimetric Analysis

Thermogravimetric analysis (TGA) was performed using TA Instruments Discovery TGA system with 5 mg samples. All samples were under a nitrogen gas purge of 25 mL/minute and started at 30 °C. They underwent an isothermal period of one minute and then ramped to 10 °C per minute to 600 °C. In between each run, the furnace was cooled to 30 °C. Step transition analyses and derivative plots were utilized to determine the onset of decomposition (T_{Onset}), the weight-loss percentage of the sample, and the temperature, which corresponds to the decomposition of the sample at the highest rate ($T_{\Delta Max}$).

3.2.4. Differential Scanning Calorimetry

TA Instruments Differential Scanning Calorimetry (DSC) equipped with a refrigerated cooling system under a nitrogen gas flow of 50 mL per minute was utilized to analyze 5 mg samples contained in an aluminum Tzero pan. The DSC calibration was performed with indium for heat flow and temperature. The DSC measurements were taken at an equilibration of room temperature, isothermal for 10 minutes, ramp 10.00 °C per minute to 120 °C, isothermal for 10 minutes to remove bound solvents, ramp 10.00 °C per minute back to -30 °C, isothermal for another 10 minutes, and ramp 10.00 °C per minute to 300 °C. Calibration of the heat flow and heat capacity were performed using aluminum and sapphire references.

3.2.5. X-ray Scattering

X-ray scattering was performed with the Dual Source and Environmental X-ray Scattering (DEXS) at the University of Pennsylvania at room temperature and under vacuum. The Xeuss 2.0 by XENOCS has a Cu X-ray source, computer-controlled focusing and transmission incident sample geometries, a 1M pixel Pilatus detector (2D), and a smaller detector for simultaneous SAXS and WAXS. A high flux collimation was used with a slot of 1.2 mm × 1.2 mm. Each sample was run for 600 seconds. The intensity reported is not the absolute intensity and, thus, is reported in arbitrary units (a.u.). All samples were placed in a desiccator prior to running and subsequently cut into squares to span across the sample holder before X-ray scattering characterization. The X-ray scattering profiles were evaluated using Foxtrot 3.4.9; the isotropic 2-D scattering patterns were azimuthally integrated to yield intensity versus scattering vector.

3.2.6. Atomic Force Microscopy (Nanoindentation)

The elastic modulus and hardness of the silk/cellulose biocomposites were investigated by atomic force microscopy (AFM) based nanoindentation. Samples were adhered to microscope slides by the sparse application of a cyanoacrylate-based adhesive and left to dry in a fume hood to mitigate settling of the adhesive's vapor onto the sample's surface. Prior to mounting the samples in the Asylum Research MFP-3D AFM, they were kept in a dehydrated state via storage in a vacuum desiccator. Nanoindentation was performed under ambient conditions using spherical indenters of radius 40 nm (Nanotools Biosphere B40-FM). The inverse optical lever sensitivity and spring constant of the cantilevers were calibrated using the microscope slide as an infinitely hard surface. This allows for an accurate relationship between cantilever deflection and the force applied by

the indenter to the sample. A topological map was scanned over a 20 μm × 20 μm area, and 25 load-displacement curves were recorded for each sample. In order to account for the adhesive forces between the indenter and the biocomposite, the Johnson-Kendall-Roberts (JKR) model was used to extract both the elastic modulus and hardness. The JKR approach is a modification of the Hertzian model that takes into account the attractive forces between the indenter and the sample surface [65]. It is regarded as a more accurate model when measuring soft-materials where adhesion can have a stronger influence on the as-determined elastic modulus values [66]. Notbohm et al., states that the JKR model is more appropriately applied to the loading curve, as opposed to the unloading, when nanoindentation is performed on an AFM-based system [67].

3.2.7. Dielectric Relaxation Spectroscopy

The ionic conductivity of the biocomposites made with different ionic liquids and coagulation agents was measured using Dielectric Relaxation Spectroscopy (DRS) at the University of Pennsylvania. Solartron Modulab XM materials test system was employed in a frequency range of 0.1 Hz to 1 MHz, and the samples were tested in a temperature range of 300 K – 450 K (26.85 – 176.85 °C). The film was placed between two stainless steel electrodes, with the top plate having a diameter of 6 mm. When conductivity measurements were being taken, the sample was in a Janis VPF-100 cryostat under vacuum [68]. The measurements began at the temperature of 450 K (176.85 °C) to ensure no excess water was left in the sample and then decreased by 10 K at each measurement.

3.3. Results and Discussion

The quantitative and qualitative data obtained from varying coagulation agents and ionic liquids while keeping the biomaterial compositions constant shows morphological, thermal, and mechanical property changes, as well as changes in ionic conductivity. Films regenerated using hydrogen peroxide were more brittle than those regenerated with ethanol. These distinct differences in morphology ultimately correlated with changes in the ionic conductivity of the biocomposite films. The following characterization tests provide more details about how varying the type of ionic liquid, and coagulation agent causes changes in the structural, morphological, thermal, and mechanical properties.

3.3.1. Scanning Electron Microscopy

Scanning Electron Microscopy (SEM) was employed to examine the morphological and topographical properties of the regenerated silk/cellulose films, as seen in **Figure 3.1**. All the films synthesized using different ionic liquids and coagulation agents look different at the surface level. The EMIMAc film regenerated with ethanol has ridges running through the entire surface of the film. This differs from all the other films which do not have this distinct characteristic. The EMIMCl film regenerated with ethanol is relatively smooth, with one larger ridge running down the middle of the entire film's surface. The films regenerated with hydrogen peroxide both seem to have a few shallow spheres on the surface. Specifically, the EMIMAc hydrogen peroxide film has one shallow sphere and has longer ridges running over almost the entire surface of the film. This differs from the EMIMCl hydrogen peroxide film, which is much smoother than the EMIMAc hydrogen peroxide film. There are only a few shallow spheres on the surface, but

surrounding areas are devoid of any large ridges like the rest of the films. From these images, it is possible to see the effect of various ionic liquids and coagulation agents on the topography of the different films.

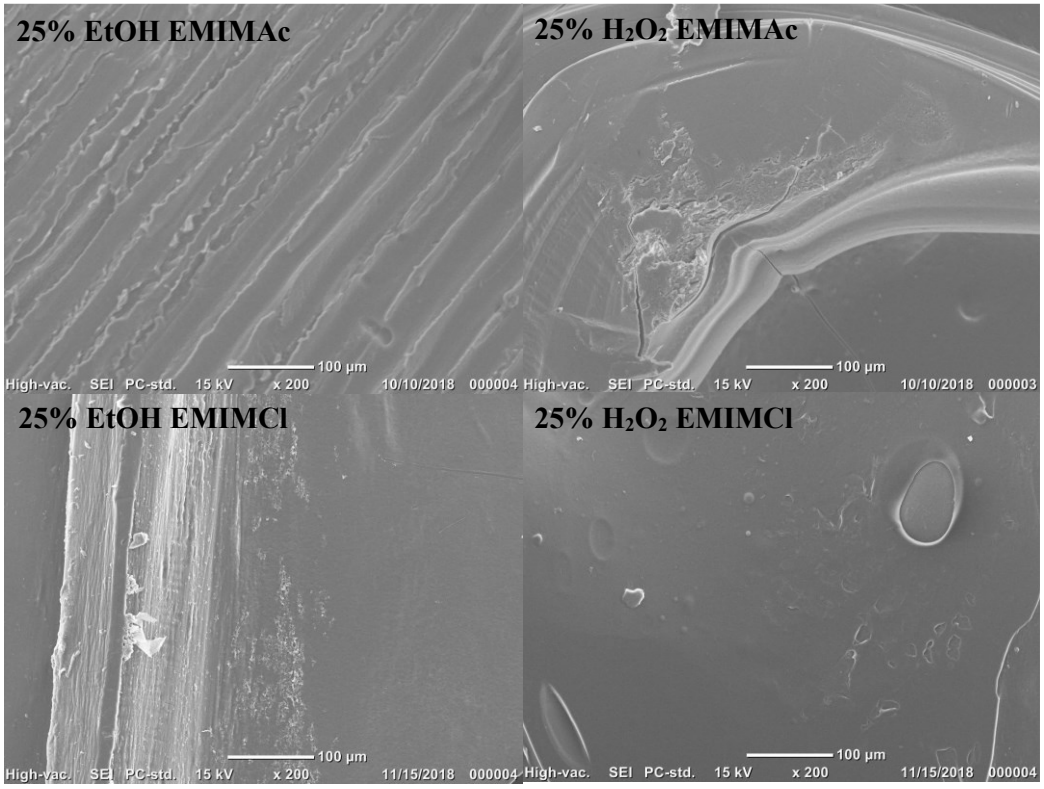

Figure 3.1. *SEM images of the 50% silk and 50% cellulose regenerated films using various ionic liquids and coagulation agents.*

3.3.2. Fourier Transform Infrared Spectroscopy

Fourier Transform Infrared Spectroscopy (FTIR) was used to ensure proper blending of the materials, as well as to calculate the secondary protein structures within the regenerated materials, as seen in **Figure 3.2**. The IR spectra were normalized to compare peak breadth and location of the various samples. In all of the spectra, the O-H group can be seen from approximately 3550 to 3000 cm^{-1}. The hydrogen peroxide films show this

peak as being rounder than the ethanol films, which have a more pronounced linewidth point. This peak can come from the O-H groups of cellulose as well as any leftover coagulation agent. The next peak seen in all the spectra is at approximately 2900 cm^{-1}. This corresponds to a C-H stretch seen in cellulose. Amide regions I, II, and III are present in most biocomposites, which suggests the silk is indeed present. These regions have similar wavenumbers in the films treated with ethanol and the films treated with hydrogen peroxide. However, the amide II region is missing from the EMIMCl film regenerated with hydrogen peroxide. The large main peak seen at approximately 1030 cm^{-1} corresponds to the C-O stretch in cellulose. The small shoulder peak at about 1160 cm^{-1} corresponds to the C-N stretch from the imidazolium ring in the ionic liquid. The low absorption of this C-N stretch peak possibly indicates a minimal amount of ionic liquid remains in the films after using the coagulation agent.

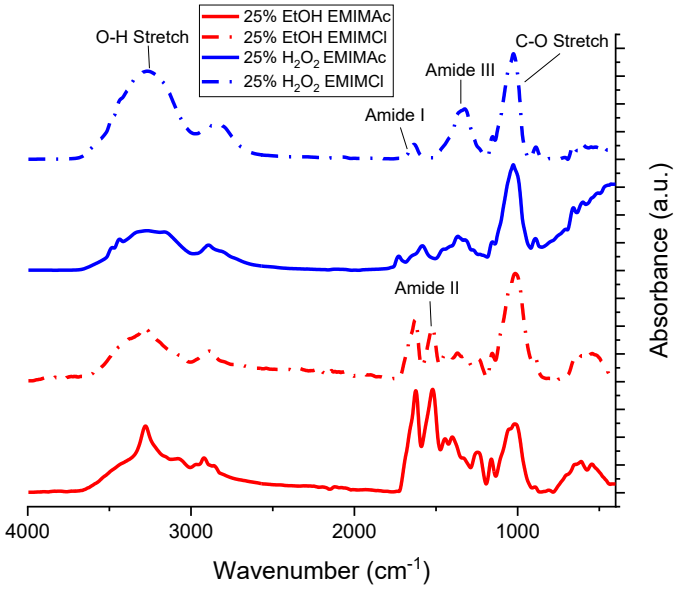

Figure 3.2. *FTIR spectra of the 50% silk and 50% cellulose regenerated films using various ionic liquids and coagulation agents.*

Fourier Self-Deconvolution was used to analyze the amide I region from 1705 cm^{-1} to 1595 cm^{-1} [69], and the secondary structure content is summarized in **Table 3.1**. The side chains in all samples vary by a maximum of 5.9%. The hydrogen peroxide films do not differ at all since both have no side chains in the biocomposite films, whereas the ethanol films differ by 4.0% between ionic liquids. Turns have nearly the same value for ethanol samples but vary more in hydrogen peroxide films. There is only a 2.4% difference in turns for films coagulated with ethanol, whereas the hydrogen peroxide films vary by 11.1% with the EMIMAc films having a higher amount of turns. Random coils are more consistent among the ethanol coagulation agent when compared to the hydrogen peroxide coagulation agent. Specifically, the ethanol films vary by 5.2% compared to the hydrogen peroxide films, which vary by 9.3%. When looking at alpha helices, ethanol samples vary less between ionic liquids than hydrogen peroxide films again. Specifically, samples made with EMIMCl have a 1.6% greater number of alpha helices than EMIMAc samples. Conversely, hydrogen peroxide films vary more between ionic liquids, precisely 13.6%. The EMIMAc hydrogen peroxide film has 11.6% more alpha helices than the EMIMAc ethanol film. The EMIMCl hydrogen peroxide film has 3.6% fewer alpha helices than the EMIMCl ethanol film. This shows there is not only a difference between ionic liquids but also coagulation agents. Finally, the β-sheet content differs between samples and is connected to the ionic conductivity, discussed in the later section. The β-sheet content for hydrogen peroxide samples is exceptionally different, with the EMIMCl film having 34.2% more β-sheets than the EMIMAc film. This is different from ethanol films, which do not differ vastly. There is only a 5.2% difference in β-sheet content, with the EMIMCl sample having a higher

percentage than EMIMAc. Overall, the EMIMCl hydrogen peroxide sample has the highest β-sheet content of the three samples.

Table 3.1. *Secondary structure contents of 50% silk and 50% cellulose biocomposites created using various ionic liquids and coagulation agents.*

Composition	Coagulation	Side Chains	β-Sheets	Random Coils	Alpha Helices	Turns
50/50 Silk-Cellulose from EMIMAc	25% H_2O_2	0.0%	14.3%	39.8%	21.2%	24.6%
50/50 Silk-Cellulose from EMIMCl	25% H_2O_2	0.0%	48.5%	30.5%	7.6%	13.5%
50/50 Silk-Cellulose from EMIMAc	25% EtOH	5.9%	41.0%	20.5%	9.6%	23.0%
50/50 Silk-Cellulose from EMIMCl	25% EtOH	1.9%	46.2%	15.3%	11.2%	25.4%

3.3.3. Thermogravimetric Analysis

Figure 3.3 shows the thermograms obtained from TGA analysis of the four different biocomposite films. In contrast, **Figure 3.4** shows the derivate weight-loss percentage thermograms, which help determine the maximum temperature of decomposition. These thermograms were used to determine the onset and end temperatures, as well as the weight-loss percentage and $T_{\Delta Max}$. **Table 3.2** displays the resulting values of the analyses using both of these figures. The films made using EMIMAc demonstrate a bimodal thermogram compared to the EMIMCl films. In this case, the

biocomposites generated with EMIMCl show fewer interfaces than the samples made with EMIMAc. Previously, it was discussed that the bimodal result as compared to pure material is strongly related to the number of interfaces formed during the mixing process [43]. Looking at the thermograms, differences are also seen in the onset, end, and $T_{\Delta Max}$ temperatures. The difference between the onset temperatures for the hydrogen peroxide films varied by 38.5 °C. This is a slightly smaller difference compared to the ethanol films, which differed by 49.4 °C. The onset temperature for the EMIMAc ionic liquid was highest in the hydrogen peroxide sample, while the EMIMCl ionic liquid had the highest onset temperature for the ethanol film. The onset temperature of the ethanol film in EMIMCl is approximately 15.0 °C higher than the hydrogen peroxide film in EMIMAc. The ethanol film also has a higher percentage of β-sheets than the hydrogen peroxide film, about 32%, which could increase the onset temperature of the film. Again, the end temperature for EMIMAc coagulated with hydrogen peroxide is higher than that of the EMIMAc coagulated with ethanol by 14.1 °C. However, EMIMCl coagulated with hydrogen peroxide has a lower end temperature than EMIMCl coagulated with ethanol by 12.4 °C. This difference is slightly smaller than the difference in end temperatures between the EMIMAc films. When looking at the weight-loss percentage of the samples, the EMIMCl sample coagulated with ethanol had one of the lowest weight-loss percentages of 46.7%, only 1.7% greater than the EMIMCl sample coagulated with hydrogen peroxide. The EMIMCl ethanol film also corresponds to the highest onset temperature. Both samples using EMIMAc show a more significant difference in weight-loss percentage than the EMIMCl films, which show relatively similar weight-loss percentages, with the film coagulated with ethanol only having 1.7% more weight loss than that of the hydrogen

peroxide film. The hydrogen peroxide films showed an 11.0% difference in weight loss from the EMIMAc film to the EMIMCl film. This is different from the ethanol films, which showed a greater difference in the weight-loss percentage. Specifically, the EMIMAc film coagulated with ethanol lost 20.6% more of its weight than the EMIMCl sample. The $T_{\Delta Max}$ is highest for the EMIMAc film coagulated with hydrogen peroxide, while the lowest corresponds to the EMIMCl film coagulated with hydrogen peroxide. There is very little difference between the ethanol samples, 2.1 °C, while the hydrogen peroxide films vary by 50.2 °C, a much more significant difference than the ethanol films. It is also interesting to note that the EMIMCl film coagulated with hydrogen peroxide had more water retention than all the other samples. These results show how much the anion of the ionic liquid, as well as the coagulation agent, can affect the thermal stability of the silk/cellulose biocomposites.

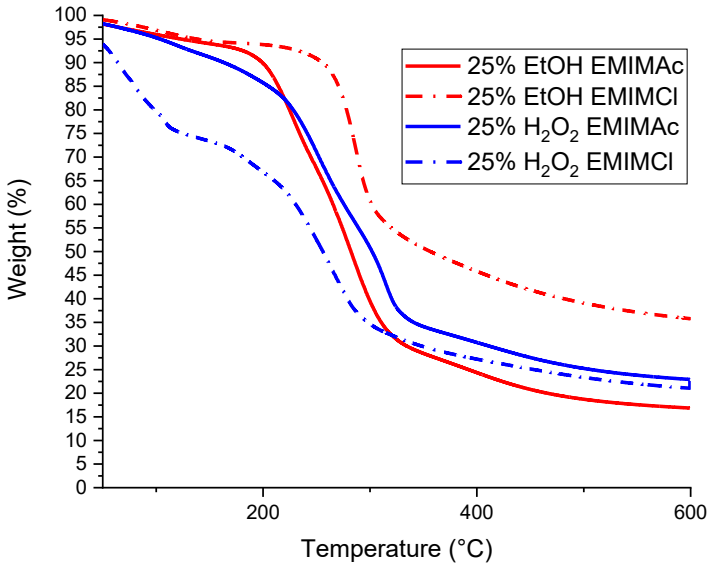

Figure 3.3. *Thermograms of different 50% silk and 50% cellulose biocomposites regenerated using various ionic liquids and coagulation agents.*

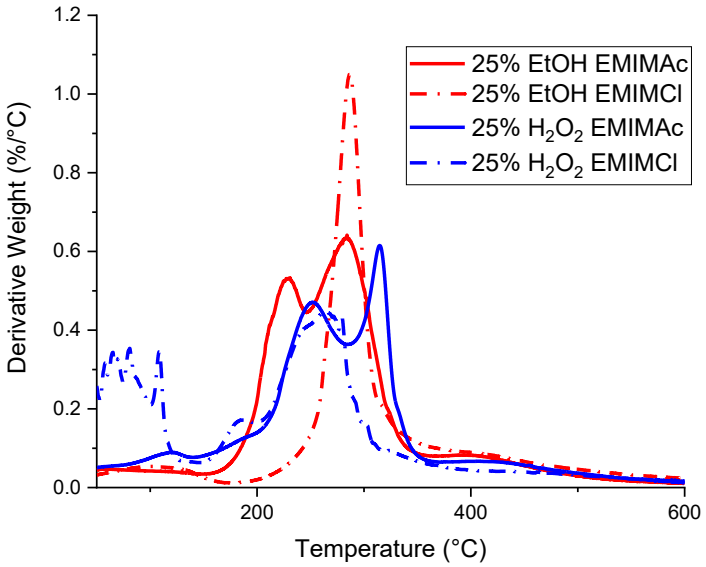

Figure 3.4. *Derivative weight-loss percentage plots of the 50% silk and 50% cellulose biocomposite films used to determine* $T_{\Delta Max}$.

Table 3.2. *Start and end temperatures, total weight-loss percentage, and the maximum temperature of the derivative representing when maximum weight loss occurred are used to characterize TGA results of the 50% silk and 50% cellulose biocomposites.*

Composition	Coagulation	T_{Onset} (°C)	T_{End} (°C)	Wt. Loss (%)	$T_{\Delta Max}$ (°C)
50/50 Silk-Cellulose from EMIMAc	25% H_2O_2	251.1	325.7	56.0	314.7
50/50 Silk-Cellulose from EMIMCl	25% H_2O_2	212.6	290.2	45.0	264.5
50/50 Silk-Cellulose from EMIMAc	25% EtOH	216.7	311.6	67.3	284.2
50/50 Silk-Cellulose from EMIMCl	25% EtOH	266.1	302.6	46.7	286.3

3.3.4. Differential Scanning Calorimetry

Figure 3.5 shows standard DSC scans for the four different samples of biocomposites using ethanol, hydrogen peroxide, EMIMAc, and EMIMCl as coagulation agents and ionic liquids, respectively. The EMIMAc hydrogen peroxide sample has a crystallization peak at approximately 537 K (263.85 °C) while the EMIMCl hydrogen peroxide sample has a crystallization peak at around 523 K (249.85 °C), 14 K lower. The film prepared using EMIMCl has a much more defined, sharp crystallization peak as compared to the film made with EMIMAc. The same is true of the films coagulated with ethanol. The EMIMCl film coagulated with ethanol has a sharp crystallization peak at approximately 552 K (278.85 °C), higher than both hydrogen peroxide samples as well as

the other ethanol film. The EMIMAc film coagulated with ethanol seems to have two crystallization peaks, with the peak at the highest temperature being 515 K (241.85 °C). This is lower than all other samples. This sample also seems to have an endothermic peak at approximately 542 K (268.85 °C). This peak could correspond to additional interface loss in the sample after the first two crystallization peaks. The DSC graphs were also analyzed to determine the glass transition temperatures of the films, as seen in **Table 3.3**. Samples coagulated with hydrogen peroxide had much lower glass transition temperatures than those coagulated with ethanol. Specifically, the EMIMAc sample coagulated with hydrogen peroxide had a temperature 60.7 K lower than that of the EMIMAc sample coagulated with ethanol. Similarly, the EMIMCl sample coagulated with hydrogen peroxide had a temperature 98.9 K lower than that of the EMIMCl sample coagulated with ethanol. It is also possible to see films created using ethanol varied less between samples than the hydrogen peroxide films. Ethanol films only vary by 9.5 K, with the EMIMCl film having a higher glass transition temperature. This is different from the hydrogen peroxide samples, which vary by 28.7 K, and the EMIMAc film has a higher glass transition temperature. These glass transition temperatures are later used to normalize the ionic conductivity data that was collected.

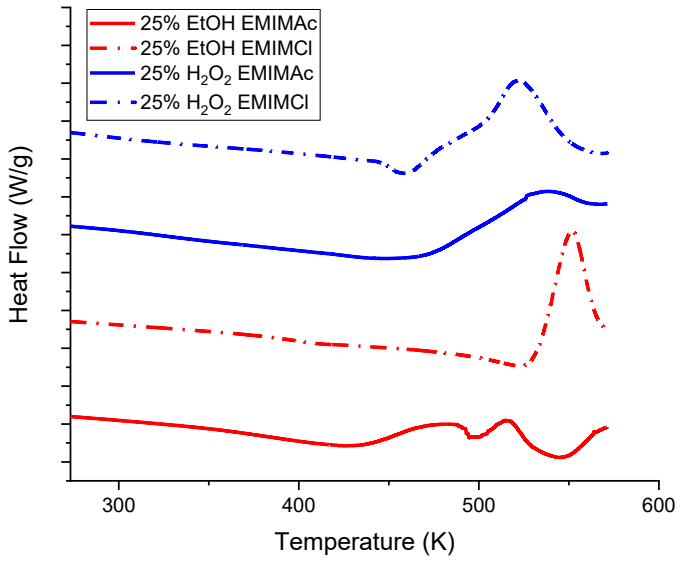

Figure 3.5. *DSC heat flow scans of the 50% silk and 50% cellulose biocomposite films used to determine the glass transition temperatures.*

Table 3.3. *Glass transition temperatures of 50% silk and 50% cellulose biocomposites created using various ionic liquids and coagulation agents, determined by DSC in degrees Celsius and Kelvin.*

Composition	***Coagulation***	***T_g (°C)***	***T_g (K)***
50/50 Silk-Cellulose from EMIMAc	25% H_2O_2	56.3	329.4
50/50 Silk-Cellulose from EMIMCl	25% H_2O_2	27.6	300.7
50/50 Silk-Cellulose from EMIMAc	25% EtOH	117.0	390.1
50/50 Silk-Cellulose from EMIMCl	25% EtOH	126.5	399.6

3.3.5. X-ray Scattering

The morphological investigation is initiated by looking at distinct spacing observed in the pure materials (e.g., silk fiber and cellulose powder) [25]. For the silk fibers in **Figure 3.6**, six scattering peaks are observed moving from high to low scattering vector regions. The peaks are located at q_1=1.34 nm^{-1}, q_2=6.53 nm^{-1}, q_3=14.80 nm^{-1}, q_4=17.60 nm^{-1}, q_5=23.46 nm^{-1}, and q_6=28.88 nm^{-1}. The *d*-spacing for each peak is calculated by using the $d=2\pi/q$ formula, and are d_1=4.69 nm, d_2=0.96 nm, d_3=0.42 nm, d_4=0.36 nm, d_5=0.27 nm, and d_6=0.22 nm, respectively. The *d*-spacing observed at 0.42, 0.36, 0.27, and 0.22 nm corresponds to the distance between β-strands and primary structure; especially, the silk II crystalline spacings, the distance at 0.96 nm corresponds to the inter-sheet distance between β-sheets, and the distance at 4.69 nm corresponds to the size of the β-sheets in the lateral direction [70-76]. In cellulose powder, three distinct spacings are observed. The microfibril distance related to crystal size is at q_1=16.10 nm^{-1} (3.58 nm). The other spacings in cellulose can be attributed to its monoclinic unit cell of cellulose I_β equatorial lattice planes (q_2=16.10 nm^{-1} and q_3=10.90 nm^{-1}). Between q_1 and q_2, there are two small peaks at q_a=14.29 nm^{-1} and q_b= 12.42 nm^{-1}. The calculated *d*-spacings are d_2= 0.39 nm, d_3= 0.57 nm, d_a= 0.44 nm, and d_b= 0.50 nm. The other scattering peaks (q_4=20.75 nm^{-1}, q_5=24.71 nm^{-1}, and q_6=29.67 nm^{-1}) are related to the cellulose crystallinity spacings. In support of the data, Vainio et al. reported crystalline monoclinic cellulose of Avicel with a scattering vector and reflection values of 15.7 nm^{-1} (200), 11.84 nm^{-1} (110), and 10.5 nm^{-1} ($1\bar{1}0$) [85]. The 0.6 nm index is related to the longer side of the square structure, which is always parallel to a side of the crystal. Helbert et al. suggest that the cellulose microfibrils could be the packing of several sheets of the 0.6-nm lattices [16]. The crystal size estimation for the

Avicel using the Scherrer equation is 3.97 nm, which matched published data of related systems [77-81].

The scattering profile for the silk/cellulose biocomposites is shown in **Figure 3.7**. The 2D scattering profiles (not shown here) showed isotropic rings for all biocomposites. Independent of the type of ionic liquid used as a solvent, the data shows that the films coagulated with hydrogen peroxide are more semicrystalline than the samples coagulated with ethanol. The semicrystalline regions of the sharp peak are associated with the regions of cellulose rather than silk. To demonstrate this effect, 100% cellulose films were regenerated using EMIMAc as the solvent and coagulated with hydrogen peroxide and ethanol. **Figure 3.8** shows the X-ray scattering profile for these two samples. As the X-ray scattering profile demonstrates, hydrogen peroxide increases the cellulose semicrystallinity, while ethanol does not. A coagulation agent in the form of alcohol induces changes in the protein β-sheets formation, as previously demonstrated [44]. In continuation with the silk/cellulose biocomposites, the attention is moved to look into the morphological effect as a function of coagulation agents and type of ionic liquid upon various correlation distances. The peak position, scattering vector (q), and d-spacing calculated using the $d=2\pi/q$ formula are reported in **Table 3.4** and **Table 3.5**. Peak *1* represents the minimum scattering vector observed in the X-ray scattering. This peak was observed in both biocomposites, which were dissolved using EMIMAc, independent of the coagulation agent; however, it is dependent on the type of ionic liquid. Interestingly, the d-spacing increases from 5.28 to 13.4 nm as the coagulation agent changes from ethanol to hydrogen peroxide, respectively. This peak is related to the average microfibril-cross sectional dimension [25] and dependent on the composition of the materials and type of ionic

liquids, as previously published [45]. The diameter of microfibrils is known to range from about 2 to 20 nm [86]. Peak *2* is indicative of the existence of an intercalation structure with the insertion of either silk into cellulose or cellulose into silk [25]. This peak intensity increases with hydrogen peroxide; however, the *d*-spacing remained constant, independent of solvent and coagulation agent, at an average of 0.73 nm. In pure silk, this region is related to the distance between β-sheets. It is now possible to confirm that the cellulose strands can directly affect its formation. Peaks *3* and *4* are attributed to the cellulose unit cell spacing and to the distance between silk β-strands, which depend on the solvent and coagulation agent. This region includes the silk I spacings which is a mixture of alpha-helices, β-sheets and random coils. In **Tables 3.4** and **3.5**, it can be seen that the samples regenerated with EMIMAc have slightly higher spacing than the ones regenerated with EMIMCl. This is due to inter- and intramolecular interactions between the acetate anion oxygen receptors and the hydroxide groups in natural fibers and in cellulose molecules, which are higher than the chloride ion. This is important because it is now possible to suggest that backbone to backbone spacing between molecules is affected by the type of anion in the ionic liquid solvent. Peaks *5* to *15* are related to the crystalline periodicity of cellulose, but it also included correlation distances from the silk II structures as previously shown in **Figure 3.6**.

In summary, the X-ray scattering profiles show a semicrystalline structure for all samples coagulated with hydrogen peroxide, which is independent of the solvent type. It can be confirmed the level of disruption of the β-sheet formation and cellulose microfibril can be affected by the type of ionic liquid. The various results demonstrate that inter- and intramolecular interactions between the silk and cellulose molecules can be controlled with

the kind of coagulation agent, which causes changes in the thermal, mechanical, and ionic conductivity properties.

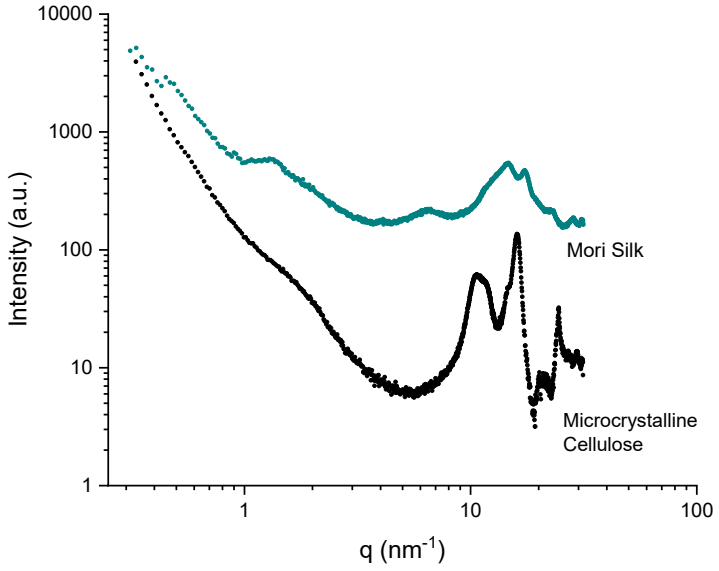

Figure 3.6. *X-ray scattering profiles for Mori silk and microcrystalline cellulose.*

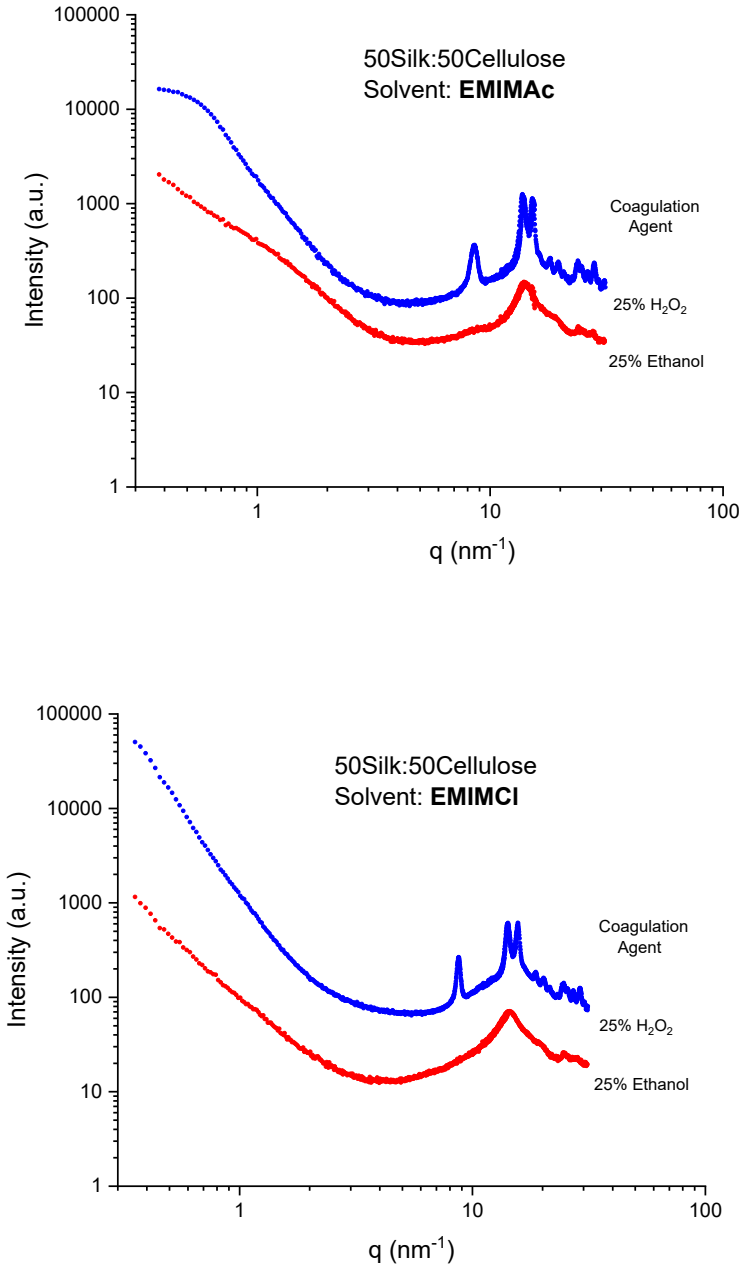

Figure 3.7. *X-ray Scattering profiles for 50% silk and 50% cellulose biocomposites as a function of coagulation agent and ionic liquid type.*

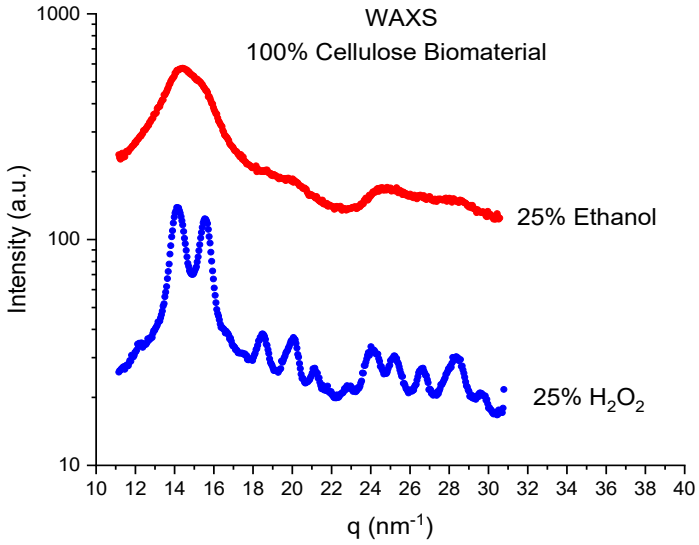

Figure 3.8. *X-ray scattering profiles for 100% cellulose films as a function of coagulation agent.*

Table 3.4. *Scattering vector and correlation distances for 50% silk and 50% cellulose biocomposites dissolved in EMIMAc and coagulated with two different coagulation agents.*

	EMIMAc	
Peak Position	***q* (nm^{-1})/*d* (nm)**	
	H_2O_2	**Ethanol**
1	0.47/13.4	1.19/5.28
2	8.6/0.73	8.6/0.73
3	13.8/0.46	14.2/0.44
4	15.3/0.41	-
5	16.4/0.38	-
6	18.1/0.35	19.3/0.32
7	19.7/0.32	-
8	20.7/0.30	-
9	21.6/0.29	-
10	22.4/0.28	23.9/0.26
11	23.9/0.26	-
12	24.8/0.25	-
13	26.2/0.24	-
14	28.0/0.22	27.8/0.22
15	29.4/0.21	-

Table 3.5. *Scattering vector and correlation distances for 50% silk and 50% cellulose biocomposites dissolved in EMIMCl and coagulated with two different coagulation agents.*

	EMIMCl	
Peak Position	***q* (nm^{-1})/*d* (nm)**	
	H_2O_2	**Ethanol**
1	-	-
2	8.8/0.71	-
3	14.2/0.44	14.4/0.44
4	15.8/0.40	-
5	16.8/0.37	-
6	18.7/0.33	20.0/0.31
7	20.2/0.31	-
8	21.4/0.29	-
9	23.2/0.27	-
10	24.6/0.25	25.0/0.25
11	25.7/0.24	-
12	27.2/0.23	-
13	29.00/0.22	-
14	30.4/0.21	-
15	31.2/0.20	-

3.3.6. Atomic Force Microscopy (Nanoindentation)

AFM-based nanoindentation was carried out on biocomposite samples formed by each of the four ionic liquid/coagulant combinations. The measured load-indentation curves were fit to the JKR model by way of the analysis tool accompanying the Asylum MFP-3D software package (v31). The maximum indentation depth was, on average, 30 nm, where only the initial 10 nm was fit to avoid nonlinearities. As seen in **Figure 3.9**, the use of hydrogen peroxide in place of ethanol results in a significant (t-test, 0.35) increase in the elastic modulus from 54 to 139 MPa for EMIMAc; in the case of EMIMCl, the noticeable increase is far less significant (t-test, 0.064) with a change from 178 to 199 MPa. The sample hardness follows a similar trend where H_2O_2 results in a large increase for EMIMAc. However, between ionic liquids, coagulation with H_2O_2 results in a similar hardness of 28 MPa. This data correlates with the X-ray scattering profiles, as shown above, where the degree of crystallinity was dependent on the coagulant (i.e., films regenerated with hydrogen peroxide are more crystalline) but independent of the ionic liquid.

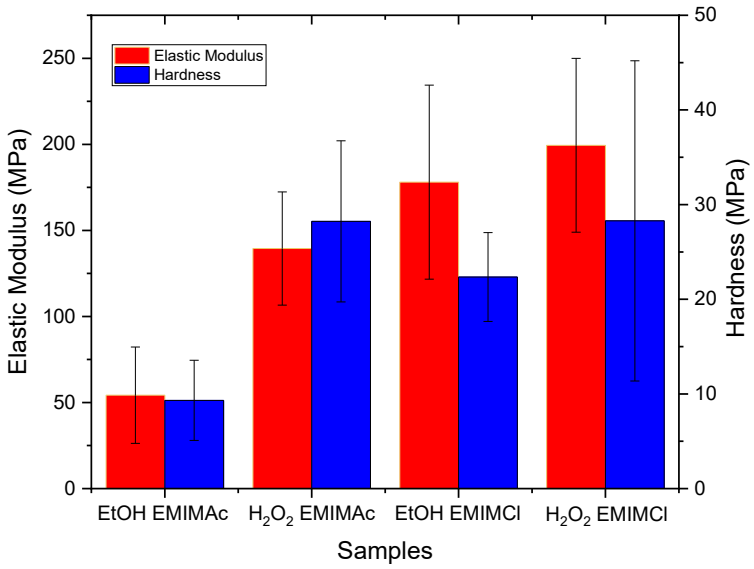

Figure 3.9. *Elastic modulus and hardness for 50% silk and 50% cellulose biocomposites as a function of coagulation agent and ionic liquid type.*

3.3.7. Dielectric Relaxation Spectroscopy

Figure 3.10 shows the ionic conductivities of the biocomposite films calculated at various temperatures. The results are reported with *1000/T* on the *x*-axis and the logarithm of the conductivity on the *y*-axis. To calculate the conductivity, the following relationship was used, $\sigma = {}^{L}/_{AR}$, where A is the cross-sectional area of the polymer film, and L is the distance between the two inner electrodes. R is the resistance calculated at each temperature using the Nyquist plot. The high *x*-intercept of the semi-circle is equal to the resistance [51]. Using all of this information, the ionic conductivity is calculated at each temperature. Shown in **Figure 3.10**, the EMIMCl sample coagulated with hydrogen peroxide has the highest ionic conductivity, followed by the EMIMCl sample coagulated with ethanol, EMIMAc sample coagulated with ethanol, and finally, EMIMAc sample coagulated with

hydrogen peroxide. It is important to note that the ionic conductivities of the films coagulated with ethanol are almost identical and collapse onto one line. The EMIMCl hydrogen peroxide sample has an ionic conductivity much higher than that of the EMIMAc hydrogen peroxide sample. This can be connected to the β-sheet content in the films. The EMIMCl sample has 48.5% β-sheets, while the EMIMAc sample only has 14.3%. The higher β-sheet content corresponds to the higher ionic conductivity of the sample. While the hydrogen peroxide samples differ in conductivity, the ethanol samples have nearly the same conductivity. Specifically, the EMIMCl ethanol sample has a slightly higher ionic conductivity than that of the EMIMAc ethanol sample. This can also be connected to the differences in the β-sheets. The EMIMCl ethanol sample has 46.2% β-sheets, while the EMIMAc ethanol sample has 41.0% β-sheets. This small difference in β-sheets could change the ionic conductivity of the samples. Again, the sample with the higher β-sheet content has a higher ionic conductivity when compared with the corresponding coagulation agent sample.

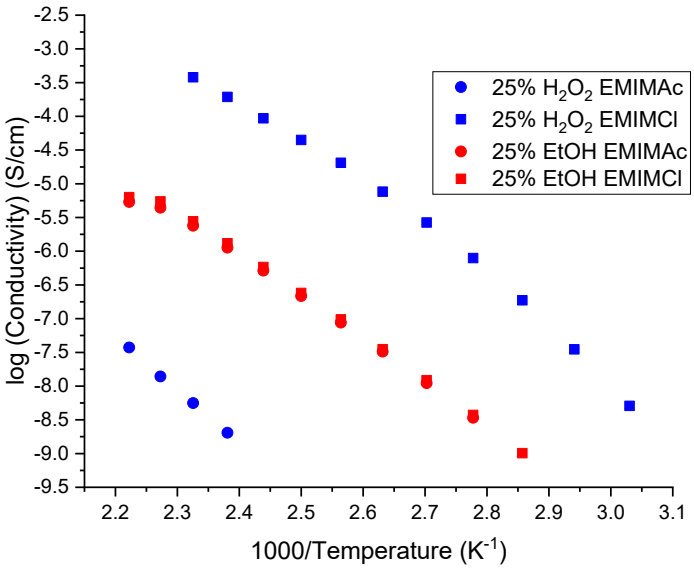

Figure 3.10. *Ionic conductivity of the 50 % silk and 50% cellulose biocomposites versus temperature.*

As shown in **Figure 3.11**, the T_g-normalized ionic conductivity corrects for the segmental motion of the macromolecules, making it possible to demonstrate the effect of morphology. If all of the data points had collapsed onto one curve or one line, the glass transition temperature would be the only contributing factor in the differences in ionic conductivity. However, since this did not occur, it is reasonable to assume other factors are affecting the ionic conductivity, such as the morphology, which will affect the differences in ion hopping or segmental motion of the polymer chains [51, 83]. The samples coagulated with hydrogen peroxide, which have the highest cellulose semicrystallinity, have the lowest ionic conductivity. Curiously, the data suggests that the samples with the highest β-sheet content have a higher ionic conductivity independent of the coagulation agent. The higher the β-sheet content, the greater the ionic conductivity. This type of phenomenon was

observed in a recent publication by Pereira et al. [50]. In this research, the ionic conductivity of silk fibroins increased with an increase in β-sheet content. The study also suggested that the β-sheets enhanced ion mobility. Considering these results, the data provide evidence to suggest a strong relationship between morphology and ionic conductivity; especially, the relationship between cellulose semicrystallinity and silk β-sheet formation is shown to have a direct effect upon ionic conductivity. In the schematic representation in **Figure 3.12**, the anion diffusion is dependent on protein β-sheet size and orientation, and cellulose semicrystallinity. For the results, it is possible to conclude that β-sheets can enhance ionic conductivity.

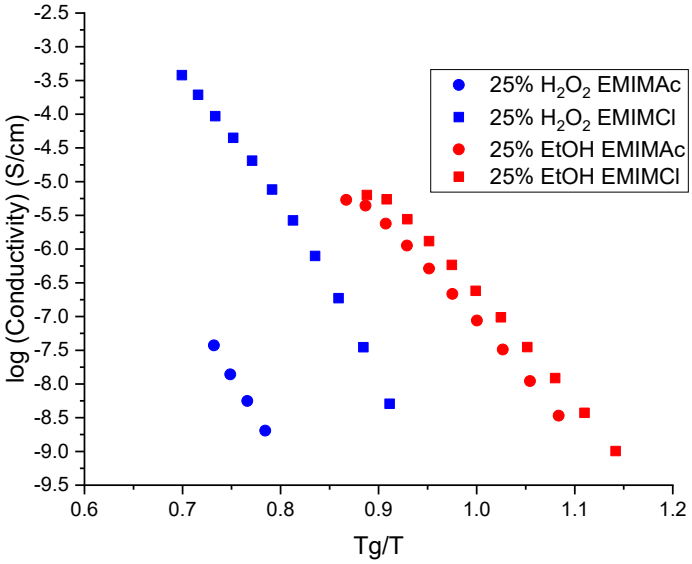

Figure 3.11. *Ionic conductivity data normalized using the glass transition temperatures of the 50% silk and 50% cellulose biocomposites.*

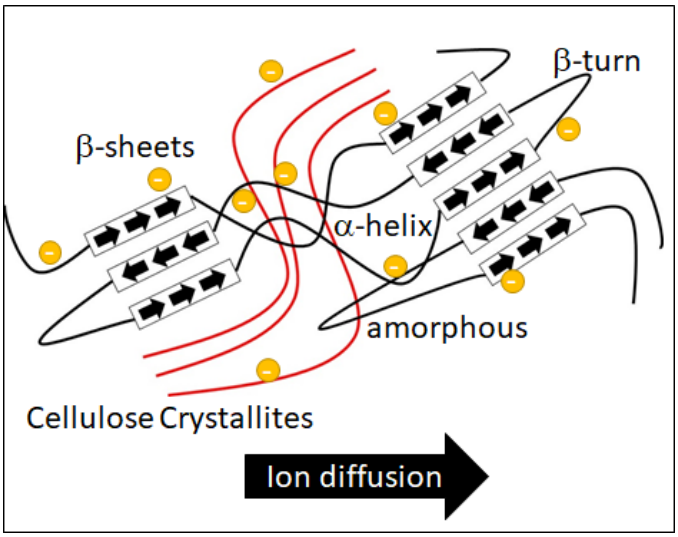

Figure 3.12. *Schematic representation of ion diffusion in a solid electrolyte based on silk/cellulose biocomposites.*

3.4. Conclusion

Varying ionic liquids and coagulation agents of the silk/cellulose biocomposites altered the morphological, thermal, mechanical, and ionic conductivity properties of the samples. The results of FTIR reveal distinct differences in secondary structures in the amide I region. Specifically, the EMIMCl sample coagulated with hydrogen peroxide had the highest β-sheet content, followed by the ethanol samples, and finally, the EMIMAc sample coagulated with hydrogen peroxide had the lowest β-sheet content. The measurement of thermal properties shows distinct differences between the various ionic liquids and coagulation agents. In terms of thermal stability, the EMIMCl sample coagulated with ethanol shows the highest onset temperature and one of the lowest weight-loss percentages. This connects to the glass transition temperatures obtained from DSC, where the EMIMCl ethanol sample exhibits the highest transition temperature. Compared to the ethanol samples, the hydrogen peroxide films have much lower glass transition

temperatures. Furthermore, the X-ray scattering showed that the samples coagulated with hydrogen peroxide are more semicrystalline than the ones coagulated with ethanol, and the morphology is independent of ionic liquids. The nanoindentation results also confirmed, by the mechanical properties, that the samples coagulated with hydrogen peroxide had the highest hardness. All these results ultimately correlate with the ionic conductivity of the biocomposite films. The ionic conductivity related to the β-sheet content. The EMIMCl hydrogen peroxide film had the highest ionic conductivity as well as the highest β-sheet content, followed by the EMIMCl and EMIMAc ethanol samples, which had the next lowest β-sheet content, and the EMIMAc hydrogen peroxide sample having the lowest ionic conductivity along with the lowest β-sheet content. This work confirms what has been suggested by others, that higher β-sheet content leads to higher ionic conductivity [50]. While further investigations will be needed to understand this phenomenon fully, this work shows that new biocomposite films in which the ionic conductivity can be tuned for specific needs are possible. This is particularly promising for the development of new technologies that utilize natural biomacromolecules as bio-electrolytes.

Chapter 4

Morphology and Ionic Conductivity Study of Silk and Cellulose Bio-composites as a Function of Ionic Liquid Concentration

4.1. Introduction

The field of biomaterials, while having been around since the 1960s, is currently gaining tremendous interest for its ability to replace devices and systems now in place that are harmful to the environment, as well as humans [87]. This interdisciplinary field combining biology, medicine, tissue engineering, chemistry, materials science, and physics is used for critical applications in these disciplines, including drug delivery capsules, scaffolds, and bio-electrolyte membranes [5-6, 88]. These novel applications are created by the blending of polymers, which are considered biomaterials because they interact with biological systems [5]. The design process to create these biomaterial devices is difficult since they must be compatible in such ways that they are non-allergenic, non-carcinogenic, and non-toxic, easily reproduced for manufacturing purposes, and contain the desired physical and mechanical properties [87]. One challenge when designing the biomaterial devices is deciding which materials to use. In the case of this study, silk, a natural protein, and cellulose, a natural polysaccharide will be used.

Silk is a natural structural protein that has both semicrystalline and amorphous regions. This protein is created by the *Bombyx mori* silkworm, an insect that spins the silk fibers coated in sericin. The fibroin is made up of three amino acids, which include serine, glycine, and alanine. These amino acids repeat in the order of $[GAGAGS]_n$, forming long chains that bond together in different formations [7]. These formations, some random while

others ordered, are called secondary structures of the protein. They include random coils, turns, β-sheets, alpha helices, and side chains. These structures are important because they contribute to the overall properties of the silk, which can include slow degradability, high tensile strength, toughness, and high biocompatibility [7, 11]. Often, this results from the crystalline regions within the silk experiencing hydrogen bonding of the amino acids, including the N-H and C-O groups, sometimes in an antiparallel direction [58-59]. As a result of these crystalline regions and extensive hydrogen bonding, the processing of this protein is often difficult.

Cellulose, a natural polysaccharide, is considered to be the most abundant polysaccharide on earth [20]. It is created by the connection of several glucose monomers through a β-(1–4) glycosidic link [56]. This polymer comes from different trees and plants, and as a result, comes in various forms. The cellulose used in this study is Avicel cellulose, a microcrystalline form referred to as cellulose I. Several other forms of cellulose can exist, including II and III, through the use of processing conditions and regeneration of the material [23, 57]. When this occurs, the resulting cellulose form is often more amorphous and has a different arrangement of chains. Like silk, this natural polysaccharide is extremely difficult to break down due to the extensive inter- and intramolecular hydrogen bonding throughout the molecule [13, 23].

As a result, ionic liquids are used to dissolve the silk and cellulose so they can eventually be turned into the desired form of a biocomposite without altering the molecular weight of the polymers [25, 43, 45, 62]. Ionic liquids are one of few solvents to be able to break apart the hydrogen bonding of cellulose by associating its cation and anion with the oxygen and hydrogen of the hydroxyl groups, respectively, as well as silk in a similar way [26-27].

After the electrostatic interactions, hydrogen bonding, and hydrophobic-hydrophobic interactions take place between the polymers, an aqueous coagulation agent is added to remove the ionic liquid, so a hydrogel and liquid phase may be created [25, 42]. The final biocomposite is formed after the coagulation agent is removed through drying so the polymers can aggregate in its place [25, 43, 45, 63]. The way in which this process takes place depends on the ionic liquid, polymer choices, polymer ratio, and coagulation agent chosen. Changing the thermal, conductive, and morphological properties based on this is possible, yet difficult to predict.

Ionic liquids are entirely ionic species that are considered to be green solvents with several desirable properties, including no emission of volatile organic compounds, negligible vapor pressure, and high thermal stability [26, 28-30]. These liquids are also researched for battery applications with some findings, including use as a substitution for electrolytes in lithium batteries, as well as the enhancement of operation of lithium-metal electrodes [89-91]. As a result of all these desirable properties, these liquids are essential for the dissolution process of polymers like silk and cellulose. They also contribute to the conductivity of the biocomposites due to their effect on morphology and the residual ions trapped in the biocomposites after coagulation takes place. Conductivity is related to two main processes in solid polymer electrolytes, ion diffusion, and dissociation. These two conditions are directly affected by the physicochemical properties of the biocomposites, which may include morphology [46].

Therefore, any morphological changes that occur when ionic liquid is added to the biocomposite will likely change the ionic conductivity. As a result, this study will investigate the effects of adding additional ionic liquid to the biocomposites, 10% by

weight of the sample, on conductivity, as well as other morphological and thermal properties. All samples are made from the same 50% silk and 50% cellulose ratio, dissolved in two ionic liquids: 1-ethyl-3-methylimidazolium acetate and 1-ethyl-3-methylimidazolium chloride, as well as coagulated in 1% and 25% ethanol and hydrogen peroxide. Samples with no additional ionic liquid were created using the same ionic liquid and coagulant for comparison purposes. It is clear from the data that the extra 10% by weight of ionic liquid into the biocomposite results in morphological and thermal changes as well as higher conductivity.

4.2. Experimental Section

Materials

Ionic Liquid

1-ethyl-3-methylimidazolium acetate and 1-ethyl-3-methylimidazolium chloride were used in the dissolution process of all biopolymers in this study. Before the dissolution process, pretreatment of the ionic liquids took place by putting a measured amount into the vacuum oven (30 inHg) at 50 °C for 24 hours to ensure residual water was removed. These ionic liquids were purchased from Sigma-Aldrich.

Cellulose and Silk

Prior to mixing, the cellulose was placed in the same vacuum oven (30 inHg) as the ionic liquid at 50 °C to remove residual water before mixing with *Bombyx mori* silk. The specific type of cellulose used to create this biocomposite was Avicel microcrystalline cellulose pf 250 μm (Techware: Z26578-0) purchased from Analtech.

Bombyx mori silk was used to mix with the abovementioned Avicel microcrystalline cellulose. The cocoons were purchased from Treenway Silks (Lakewood, CO). To degum the silk fibers, the cocoons were boiled in a 0.02M $NaHCO_3$ (Sigma-Aldrich) solution for 15 minutes, followed by using deionized water to rinse the fibers three times. This ensured all sericin was removed entirely. The fibers then air-dried overnight and were additionally placed in the vacuum oven (30 inHg) at room temperature. This ensured all residual water and moisture was removed from the fiber surface.

Dissolution of the Protein and Polysaccharide

Specific percentages were used to create the correct resulting biocomposite ratio. First, the ionic liquid was measured to comprise 90% of the total mass, and the protein and polysaccharides accounted for the other 10%. Specifically, this 10% was broken down to 50% protein, silk, and 50% polysaccharide, cellulose. As a result, both silk and cellulose accounted for 5% of the total mass. Once the solids were massed out to the correct proportion, the pretreated ionic liquid was pipetted into a vial and placed in a silica oil bath on a hot plate at 80 °C. The oil bath ensured the solution was heated evenly throughout the dissolution process of adding silk first and then cellulose. Once both polymers wholly dissolved, the solution mixed at 80 °C for 24 hours on the hot plate.

Preparation of Regenerated Biofilm

3-D printed molds made from polylactic acid with the dimensions of 12 mm x 12 mm x 1 mm for each of the four squares were used to transfer the gel solution after 24 hours of mixing was completed. Preheated to a temperature of 75 °C to ensure the gel did not solidify inside, 1 mL micropipette tips were used to transfer the solution to the molds.

The mold was placed on a balance and tared. After this, the solution was pipetted into each square, and the mass was kept consistent in each of the four squares contained in the mold by taring after the addition of solution to each. After pipetting, the mold was placed into a 250 mL beaker filled with 100 mL of coagulation agent and then sealed with parafilm for 48 hours. The coagulation agent helps to regenerate the materials and also remove as much ionic liquid as possible. Since the mass of solution put into each beaker was nearly identical, the amount of ionic liquid left in each film should also be almost the same. After 48 hours, distilled water was used to rinse the molds three times to remove as much residual ionic liquid on the surface of the film as possible. Following this, the molds were put into Petri dishes, which were then transferred to a low-pressure desiccator to dry.

Procedure of Adding 10% by Weight Ionic Liquid

For the eight films prepared in this study, the additional ionic liquid was placed on the top surface and allowed to distribute throughout the sample. Specifically, an extra 10% ionic liquid by weight was added to each sample. A 10-microliter syringe was used to transfer the small amount of additional ionic liquid on the surface. After 96 hours to ensure ample time to allow the ionic liquid to dry in, several characterization tests were performed on the samples.

Characterization

4.2.1. Fourier Transform Infrared Spectroscopy

Bruker's ALPHA-Platinum ATR-FTIR Spectrometer with Platinum-Diamond sample module was employed to complete Fourier Transform Infrared Spectroscopy (FTIR) analysis in the spectra range of 4000 cm^{-1} to 400 cm^{-1}. 128 background scans were

performed after cleaning the diamond and hammer thoroughly with acetone. Following this, 6 different locations of the biocomposite were analyzed with 32 sample scans. An average file was created and used to examine the amide I region (1595 cm^{-1}-1705 cm^{-1}) using Fourier self-deconvolution, which included parameters of a half-bandwidth of 26.4 cm^{-1}, Lorentzian line shape, and a noise reduction factor of 0.3. Gaussian profiles were used when fitting and integrating to find the correlation between specific wavelengths and area. Following this analysis, the data were smoothed using 25-point smoothing, and min-max normalization was used to enhance the functional group peaks throughout the spectra. All of this analysis was performed using Opus 7.2 software.

4.2.2. Differential Scanning Calorimetry

TA Instruments Differential Scanning Calorimetry (DSC) equipped with a refrigerated cooling system was used to find the glass transition temperatures of all samples. Indium was used for heat flow and temperature calibration, and aluminum and sapphire were used for the heat flow and heat capacity calibration. Tzero aluminum pans were used to encapsulate 5 milligrams of each sample. These samples were measured using a 50 mL per minute nitrogen gas flow. The samples were equilibrated at -40 °C, had a modulation period of one minute with a temperature amplitude of 0.318 °C, isothermal for three minutes, and then had a heating rate of 2.000 °C per minute up to 400 °C. The samples with only residual ionic liquid and 25% coagulation agents used a standard DSC procedure mentioned in chapter 3 methods.

4.2.3. X-ray Scattering

X-ray scattering was performed at room temperature and under vacuum at the University of Pennsylvania utilizing the Dual Source and Environmental X-ray Scattering (DEXS). The Xeuss 2.0 by XENOCS has several parts, including a 1M pixel Pilatus detector (2D), a Cu X-ray source, focusing and transmission incident sample geometries controlled by a computer, and a small detector for simultaneous SAXS and WAXS. A high flux collimation was utilized with a 1.2 mm x 1.2 mm slot. Samples were placed in a desiccator prior to testing, and squares were cut from each sample and taped to cover the sample holder. All samples had a running time of 600 seconds. The resulting measured intensity is not the absolute intensity and, therefore, is reported in arbitrary units (a.u.). In order to evaluate the X-ray scattering profiles, Foxtrot 3.4.9 was used. Intensity versus scattering vector was generated by azimuthally integrating the isotropic 2-D scattering patterns.

4.2.4. Dielectric Relaxation Spectroscopy

Dielectric Relaxation Spectroscopy (DRS) was performed at the University of Pennsylvania to determine the ionic conductivity of the biocomposites made with additional ionic liquid, precisely 10% by weight extra per sample, as well as residual ionic liquid. Two stainless steel electrodes were used to place the film between, with the top electrode having a diameter of 6 mm. This system was then placed into a Janis VPF-100 cryostat under vacuum [68]. The Solartron Modulab XM materials test system was used in a frequency range of 0.1 Hz to 1 MHz, as well as a temperature range of 300 K – 450 K (26.85 – 176.85 °C) [68]. This ensured the sample was tested above and below the glass transition temperature. To ensure there was no residual water left in the sample when

testing, temperature measurements were started at 450 K (176.85 °C). Following this, the temperature decreased by 10 K after each measurement.

4.3. **Results and Discussion**

Adding additional ionic liquid to the samples had significant effects on the morphological properties as well as ionic conductivity, seen in the qualitative and quantitative data listed below. The biocomposites with the extra ionic liquid were less brittle than those with residual ionic liquid only.

4.3.1. Fourier Transform Infrared Spectroscopy

Figure 4.1 shows the spectra of various samples with only residual ionic liquid as well as the extra ionic liquid added by mass obtained by Fourier Transform Infrared Spectroscopy (FTIR). This method was used to calculate secondary structures within the protein and to ensure the materials were correctly blended. All spectra were compared based on peak location and peak breadth, and this was done more easily after normalization of all spectra. In the spectra of all sixteen samples, the amide I and II regions are present, except for the EMIMCl sample coagulated with 25% hydrogen peroxide and residual ionic liquid. The appearance of these amide regions suggests the silk is indeed present as part of these biocomposites. Another functional group that is important in this analysis is found at approximately 1160 cm^{-1}. This corresponds to the C-N stretch from the imidazolium ring in the ionic liquid. In all of the eight samples with no additional ionic liquid, this peak shows a low absorption, which suggests there is only a small amount of residual ionic liquid left in the sample after the fabrication method. This differs from the samples with additional

ionic liquid added. In some of the samples, like the EMIMCl samples coagulated with 25% hydrogen peroxide and 1% hydrogen peroxide, this shoulder peak became much more pronounced. The C-O stretch in cellulose is seen at approximately 1030 cm^{-1}, and in some of the additional ionic liquid samples, this is nearly absent. Two samples that show the most drastic results pertaining to this are the EMIMAc sample coagulated with 25% ethanol as well as the EMIMCl sample coagulated with 25% hydrogen peroxide. In the case of the ethanol film, this functional group looks to be nearly absent or drastically reduced. Finally, from approximately 3550 to 3000 cm^{-1}, the O-H stretch can be seen in all of the samples. It is interesting to see that in nearly all extra ionic liquid samples, this peak becomes less gaussian-like. The EMIMAc sample coagulated with 25% ethanol and the EMIMCl sample coagulated with 25% hydrogen peroxide again show the most drastic results for this functional group.

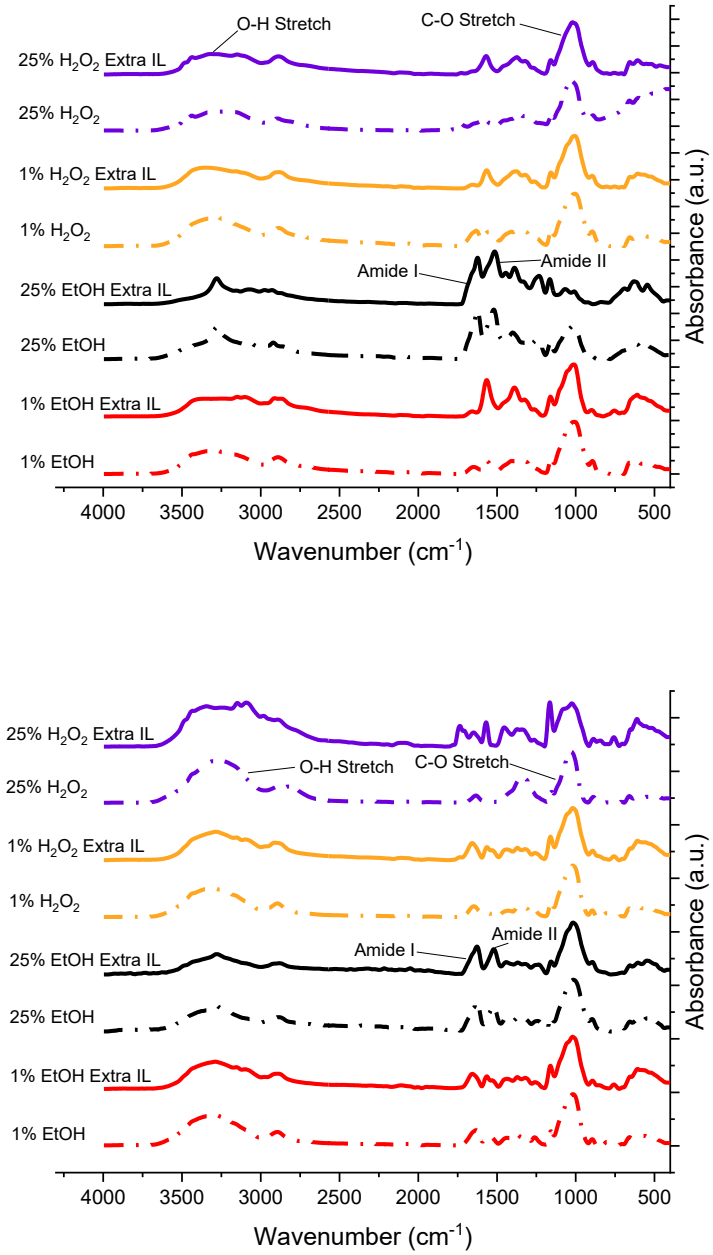

Figure 4.1. *FTIR spectra of 50% silk and 50% cellulose samples containing additional or residual ionic liquid. The graph on the top corresponds to samples made with the solvent EMIMAc, while the bottom corresponds to solvent EMIMCl.*

In **Table 4.1**, the secondary structure content of the sixteen samples is summarized. The amide I region was analyzed from 1705 cm^{-1} to 1595 cm^{-1} using Fourier Self-Deconvolution [69]. When looking at the data for both sets of ionic liquid films, the side chains do not vary drastically. Even when the ionic liquid was added to the sample, no drastic changes are observed. The turns increased when adding ionic liquid to the EMIMAc sample group. Each film coagulated with a different percentage of ethanol and hydrogen peroxide all showed an increase in turns. The most significant difference was seen in the 1% ethanol samples with a 32.4% increase in turns when adding ionic liquid. This same trend does not hold for the EMIMCl sample group. These samples seem to be random, with some pairs increasing in turns and others decreasing. Random coils again seem to be arbitrary in the EMIMAc sample group compared to the EMIMCl sample group, where they decrease when ionic liquid is added. The most substantial difference of 7.0% is seen in the 25% hydrogen peroxide samples. The alpha helices again seem to be random in both ionic liquid groups. There are slight differences in each sample set, but there are no consistent trends among the data. Finally, when looking at each of the sets, the β-sheet content differs. When looking at the EMIMAc sample set, both the 1% ethanol and 1% hydrogen peroxide showed a much more significant change than the 25% ethanol and hydrogen peroxide samples. Specifically, there was a 27.8% difference in β-sheet content among the 1% hydrogen peroxide samples and a 19.4% difference among the 1% ethanol samples. This compares to only a 1.8% difference in the 25% hydrogen peroxide samples and a 4.6% difference in the 25% ethanol samples. This may suggest the 1% coagulation agent samples are acting more like water, where secondary structures are random, and not controlling morphology in any drastic manner like the 25% coagulation agent samples can.

When looking at the EMIMCl sample set, the 1% ethanol samples again show the most considerable difference in β-sheet content. Specifically, there is a 10.4% difference compared to the second-largest difference of 6.3% seen in the 25% ethanol samples. Overall, the changes in secondary structures when adding additional ionic liquid by mass seemed to be random, but essential. This data, coupled with the FTIR spectra suggests the extra ionic liquid has a substantial effect on morphology.

Table 4.1. *Secondary structure contents of 50% silk and 50% cellulose samples with additional or residual ionic liquid.*

Ionic Liquid	Coagulant	10% IL by Mass	Side Chains	β-Sheets	Random Coils	Alpha Helices	Turns
EMIMAc	25% H_2O_2	Yes	3.0%	16.1%	18.5%	18.4%	44.1%
EMIMAc	25% H_2O_2	No	0.0%	14.3%	39.8%	21.2%	24.6%
EMIMAc	1% H_2O_2	Yes	0.3%	9.4%	25.4%	19.7%	45.2%
EMIMAc	1% H_2O_2	No	1.3%	37.2%	19.0%	25.6%	16.8%
EMIMAc	25% EtOH	Yes	6.3%	45.6%	12.9%	10.3%	24.9%
EMIMAc	25% EtOH	No	5.9%	41.0%	20.5%	9.6%	23.0%
EMIMAc	1% EtOH	Yes	1.2%	6.3%	24.5%	18.0%	50.1%
EMIMAc	1% EtOH	No	0.5%	25.7%	23.0%	33.0%	17.7%
EMIMCl	25% H_2O_2	Yes	5.4%	49.7%	23.5%	10.4%	11.0%
EMIMCl	25% H_2O_2	No	0.0%	48.5%	30.5%	7.6%	13.5%
EMIMCl	1% H_2O_2	Yes	4.1%	29.6%	17.3%	14.1%	34.9%
EMIMCl	1% H_2O_2	No	2.9%	31.3%	24.2%	20.3%	21.2%
EMIMCl	25% EtOH	Yes	1.3%	52.5%	12.4%	17.6%	16.2%
EMIMCl	25% EtOH	No	1.9%	46.2%	15.3%	11.2%	25.4%
EMIMCl	1% EtOH	Yes	2.2%	29.6%	16.9%	27.8%	23.6%
EMIMCl	1% EtOH	No	2.7%	40.0%	17.1%	22.2%	18.1%

4.3.2. Differential Scanning Calorimetry

Standard DSC scans for the sixteen samples with both residual and additional ionic liquid are shown in **Figure 4.2.** Twelve of the sixteen samples were performed using modulated DSC, so crystallization and degradation peaks are more easily seen. When looking at the graphs, it is clear the additional ionic liquid had a large impact on the thermal properties of the samples. For example, when looking at the EMIMAc sample coagulated

with 1% hydrogen peroxide and only residual ionic liquid, there seem to be approximately four crystallization peaks throughout the DSC heat flow scan. When the ionic liquid is added, two of these crystallization peaks are no longer present, and instead, two more pronounced crystallization peaks are formed. In the EMIMCl sample also coagulated with 1% hydrogen peroxide and only residual ionic liquid, a degradation peak is followed by a crystallization peak. However, when the ionic liquid is added, the degradation peak is no longer present, and instead, an additional crystallization peak appears. These two samples highlight the effects the extra ionic liquid in the biocomposites has not only on the thermal properties of the samples but also on the morphology.

Figure 4.3 shows the reversing heat capacities of all 1% ethanol and hydrogen peroxide, as well as the additional ionic liquid samples coagulated with 25% ethanol and hydrogen peroxide. The 25% coagulation agent samples containing only residual ionic liquid were not included because these samples were run previously using the standard mode rather than modulated. **Figure 4.3** was used to determine the glass transition temperatures of the twelve films not previously reported. These glass transition temperatures are listed in **Table 4.2**. When looking at all eight sample pairs, it is interesting to note the samples coagulated with 25% ethanol or hydrogen peroxide show an increase in the glass transition temperature when ionic liquid is added, compared to the 1% ethanol or hydrogen peroxide samples which show a decrease in the glass transition temperature when the ionic liquid is added. Also, the difference in these glass transition temperatures seems to be random. One particularly fascinating sample set is the 1% hydrogen peroxide samples of both EMIMAc and EMIMCl. When looking at the difference between the samples with and without additional ionic liquid in respective ionic liquids, both of these

glass transition temperatures decrease by 15.3 K exactly. All other differences between sample sets are random. Finally, when comparing the ionic liquids, the glass transition temperatures generally are higher when EMIMCl is used compared to EMIMAc. There are only two exceptions to this trend, and they are the 25% hydrogen peroxide sample with no additional ionic liquid and the 1% ethanol sample with extra ionic liquid. These two sets show a decrease in temperature when using EMIMCl. Overall, there was no clear trend when looking at the glass transition temperatures of all the samples. Ionic conductivity data is later normalized using these glass transition temperatures to demonstrate the effect of morphology on the samples.

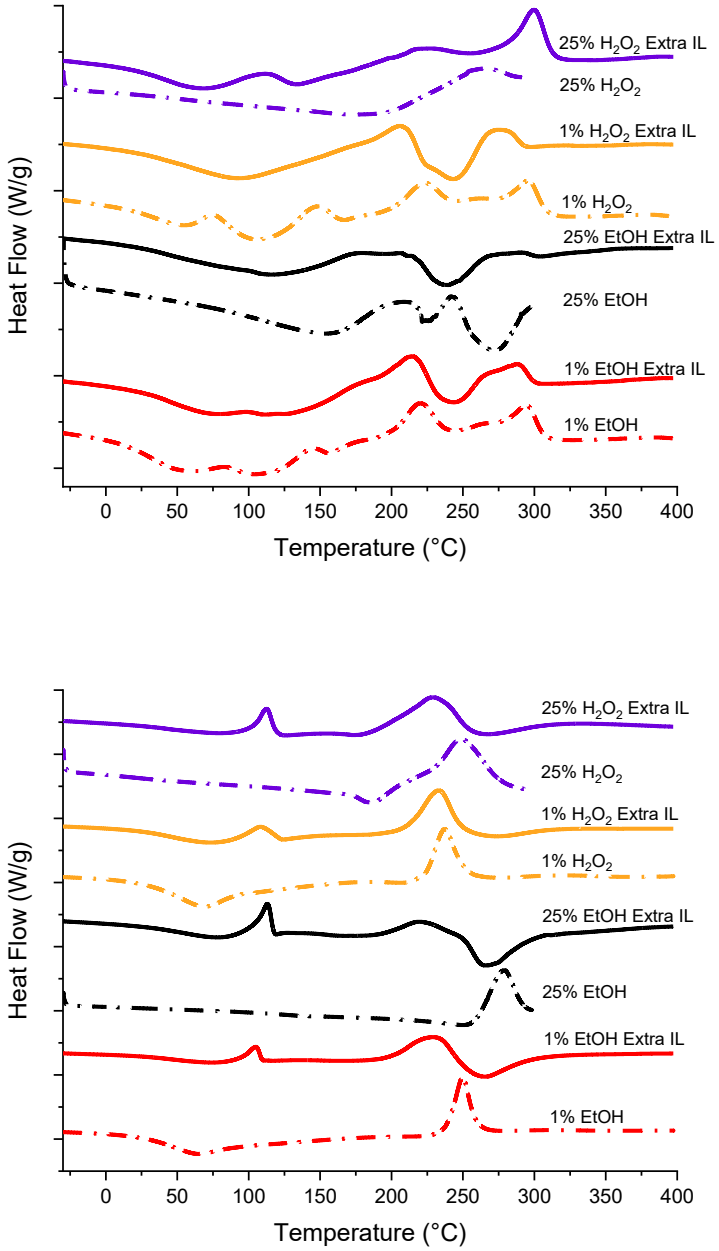

Figure 4.2. *Standard DSC heat flow scans of the 50% silk and 50% cellulose biocomposites containing either additional or residual ionic liquid. Crystallization and degradation peaks in the samples are illustrated. The top graph corresponds to EMIMAc samples, while the bottom graph corresponds to EMIMCl samples.*

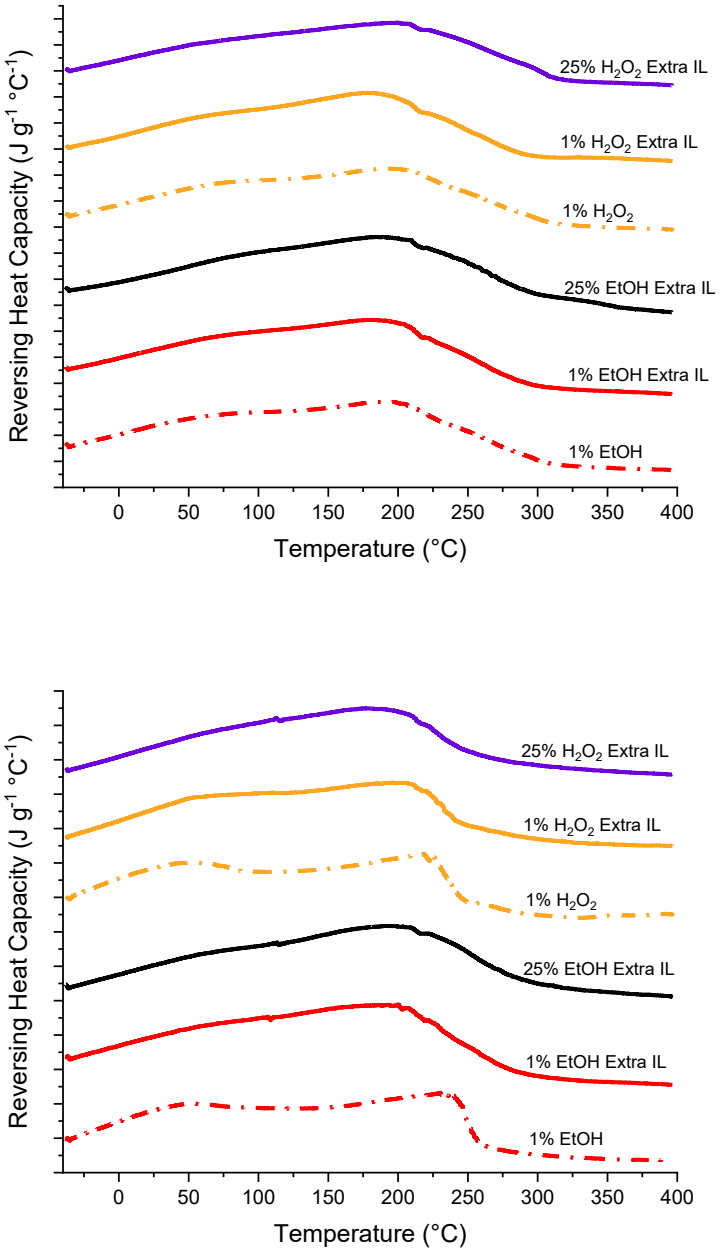

Figure 4.3. *DSC reversing heat capacities of 50% silk and 50% cellulose biocomposites containing either additional or residual ionic liquid. The glass transition temperatures of all samples were determined using this information. The top graph corresponds to EMIMAc samples, while the bottom graph corresponds to EMIMCl samples.*

Table 4.2. *Glass transition temperatures of 50% silk and 50% cellulose biocomposites containing additional or residual ionic liquid, determined by DSC in degrees Celsius and Kelvin.*

Ionic Liquid	***Coagulant***	***10% IL by Mass***	***T_g (°C)***	***T_g (K)***
EMIMAc	25% H_2O_2	Yes	124.4	397.6
EMIMAc	25% H_2O_2	No	56.3	329.4
EMIMAc	1% H_2O_2	Yes	140.9	414.1
EMIMAc	1% H_2O_2	No	156.2	429.4
EMIMAc	25% EtOH	Yes	151.0	424.1
EMIMAc	25% EtOH	No	117.0	390.1
EMIMAc	1% EtOH	Yes	154.5	427.6
EMIMAc	1% EtOH	No	157.8	431.0
EMIMCl	25% H_2O_2	Yes	145.8	419.0
EMIMCl	25% H_2O_2	No	27.6	300.7
EMIMCl	1% H_2O_2	Yes	155.9	429.0
EMIMCl	1% H_2O_2	No	171.2	444.3
EMIMCl	25% EtOH	Yes	152.2	425.4
EMIMCl	25% EtOH	No	126.5	399.6
EMIMCl	1% EtOH	Yes	145.9	419.0
EMIMCl	1% EtOH	No	184.8	457.9

4.3.3. X-ray Scattering

The X-ray scattering profiles in **Figure 4.4** show the different morphological features between the samples containing residual and 10% additional ionic liquid. First, attention is focused on less complex samples and then gradually moved to the more complex samples. Specifically, the biocomposites regenerated in EMIMCl and coagulated with 1 and 25% ethanol are examined first. For the biocomposite coagulated with 1% ethanol containing residual ionic liquid, the scattering profile shows five distinct scattering peaks at a scattering vector, q (d-spacing) of 8.87 nm^{-1} (0.71 nm), 14.31 nm^{-1} (0.44 nm), 15.82 nm^{-1} (0.40 nm), 19.65 nm^{-1} (0.32 nm) and 24.88 nm^{-1} (0.25 nm). As mentioned in previous chapters, the d-spacing at 0.71 nm corresponds to the molecular intercalation between silk chains and cellulose carbon chains. This correlation distance also includes the distances between the β-strands and primary structure, especially the silk II crystalline spacings as a result of being modified during dissolution and regeneration. The d-spacing at 0.44, 0.40, 0.32, and 0.25 nm is related to the cellulose unit cell spacing and the distance between silk β-strands; this region includes the silk I spacings which is a mixture of alpha-helices, β-sheets, and random coils. The shape of the scattering peak shows that the overall structure is somewhat semicrystalline. It is interesting to note that when the additional ionic liquid is added to the biocomposite coagulated with 1% ethanol, the scattering profile changes. For example, the X-ray scattering profile shows four distinct scattering peaks at a scattering vector, q (d-spacing) of 0.73 nm^{-1} (8.60 nm), 4.70 nm^{-1} (1.33 nm), 16.48 nm^{-1} (0.38 nm), and 24.88 nm^{-1} (0.25 nm). The d-spacing at 8.60 nm is evidence of microphase separation possibly related to the spacing between ionic clusters or spacing between rich domains of cellulose, silk, and ionic clusters. The lack of periodicity prevents a detailed

morphology from being provided; however, this is important because it delivers information that can be linked to ionic conductivity and mechanical properties. The same scattering peak is observed for the biocomposite coagulated with 25% ethanol with the additional ionic liquid. The *d*-spacing at 1.33 nm suggests an increase in the correlation distances between cellulose crystal domains and the β-strands and primary structure, especially the silk II crystalline spacings. This is the result of the added ionic liquid, which forms hydrogen bonds and electrostatic attraction between the hydroxide bonds and amide groups in cellulose and silk, respectively. This interaction between the structure of the ionic liquid and the biocomposite causes the scattering peak at 16.48 nm^{-1} to broaden as compared with the biocomposite with residual ionic liquid. This scattering peak is indicative of an amorphous morphology. When the coagulation agent concentration increases from 1% to 25% ethanol, the scattering profile also changes. Increasing the ethanol concentration is known to affect the formation of β-sheet structures in silk [62]. The X-ray scattering profile for the sample coagulated with 25% ethanol and residual ionic liquid shows four distinct scattering peaks at *q* of 14.60 nm^{-1} (0.43 nm), 20.05 nm^{-1} (0.31 nm), 24.88 nm^{-1} (0.25 nm) and 28.51 nm^{-1} (0.22nm). The scattering peak shape at 14.60 nm^{-1} is indicative of an amorphous structure; however, it suggests that the electron density of the amide group from the silk is higher than the cellulose hydroxide groups due to an increase in β-sheet content. The peak correlation distances include the cellulose unit cell spacing and the distance between silk β-strands; also, this region includes the silk I spacings, which is a mixture of alpha-helices, β-sheets, and random coils whereas the β-sheet secondary structure dominates. The FTIR spectra and the calculated secondary structure provides evidence of such. Upon the addition of the ionic liquid, the biocomposite

coagulated with 25% ethanol exhibits five scattering peaks. Curiously, this sample exhibits the formation of a new scattering peak at a q of 0.73 nm^{-1} (8.60 nm) and an increase in broadness for the peak at 20.05 nm^{-1} (0.31 nm). For the latter, the gaussian-like curve in this region is not asymmetrical as it results from the interaction between the silk chains and the ionic liquids, which changes the β-sheets inter-spacing. For the former, it is similar to the samples coagulated with 1% ethanol with the additional ionic liquid. The *d*-spacing is the same at 8.60 nm, and it provides evidence of microphase separation possibly related to the spacing between ionic clusters or spacing between rich domains of cellulose, silk, and ionic clusters. In summary, the change in coagulation agent concentration and the addition of ionic liquid causes dramatic modifications in the morphology of the biocomposites coagulated with ethanol.

Now, the focus is on biocomposites coagulated with hydrogen peroxide. Previously, it has been demonstrated the morphology of the cellulose can be modified without affecting the morphology of the silk when a blend of cellulose and silk are coagulated in various concentrations of hydrogen peroxide. Especially, it was shown that the cellulose crystal size increases linearly with hydrogen peroxide concentration [63]. The scattering profile for the samples coagulated with 1% hydrogen peroxide and residual ionic liquid shows six scattering peaks. Five of them are similar to the samples coagulated with 1% ethanol, with the exception of the peak located at *q* of 0.88 nm^{-1} (7.13 nm). This scattering peak is evidence of microphase separation. In this case, it is not related to the ion clusters, but it is related to cellulose crystals forming perhaps a lamellar morphology separated by an amorphous region just as the morphology of polypropylene [92]. The shape of the scattering peaks at *q* of 14.31 nm^{-1} (0.44 nm) and 15.82 nm^{-1} (0.40 nm), shows that

the overall structure is semicrystalline. When the ionic liquid is added to the samples coagulated with 1% hydrogen peroxide, the semicrystalline structure changes to amorphous, and the peak located at the lower scattering vector decreases to a q of 0.81 nm^{-1} (7.75 nm); however, the gaussian-like curve broadens. This is important because this correlation distance now includes the ion cluster spacing and the cellulose crystal lamellar spacing. Peculiarly, if the average distance is taken between the ion cluster of the samples coagulated with 1% ethanol of 8.60 nm and the new distance of 7.13 nm for the samples coagulated with 1% hydrogen peroxide, the result is 7.86 nm which is 1.40% different than the *d*-spacing for the samples coagulated with 1% hydrogen peroxide with the additional ionic liquid. For the 25% hydrogen peroxide with residual ionic liquid, the scattering profile shows sharp scattering peaks in the high scattering vector region as in comparison to the 1% hydrogen peroxide. This change is indicative of a change in crystallization, especially changes in the cellulose crystal size [62-63]. Three main scattering peaks are observed at a q of 8.74 nm^{-1} (0.72 nm), 14.02 nm^{-1} (0.45 nm), and 15.74 nm^{-1} (0.40 nm). The last two peaks are related to the change in the crystallization of cellulose from cellulose I to cellulose II. FTIR demonstrated that silk is present in these samples, too, so the typical cellulose II reflections are slightly skewed. The location of these two reflections barely changes as a function of hydrogen peroxide concentration. However, their intensity decreases when ionic liquid is added to the sample. This means that the crystal size did not increase with an increase in hydrogen peroxide concentration as a result of its interactions with the added ionic liquids. The reflections observed at a q of 8.65 nm^{-1} and higher are indicative of the crystalline structure periodicity combined with the silk I structures possibly separated in rich domain areas. Contrary to the other biomaterials with added ionic

liquids, the low scattering vector peak is not observed at q of 0.81 nm^{-1}. Only a 45-degree curve is observed. This could mean that the overall system might be separated by distinct interfaces. Another possibility is that the correlation distance between crystallite size and ionic clusters is higher than 15 nm.

In continuation of the analysis, X-ray scattering profiles for the biocomposites regenerated in EMIMAc are studied. As a quick comparison, the X-ray scattering profiles look very similar to the biocomposites regenerated in EMIMCl. The main differences are that mostly the samples exbibit microphase separation with the exception of the biocomposite coagulated with 1% ethanol, despite the fact of the addition of ionic liquid. This means that the ionic liquid can change the overall morphology of the biocomposites. At 1% ethanol, six scattering peaks are observed at q of 8.75 nm^{-1} (0.72 nm), 14.16 nm^{-1} (0.44 nm), 15.67 nm^{-1} (0.40 nm), 20.01 nm^{-1} (0.31 nm), 24.53 nm^{-1} (0.26 nm) and 29.04 nm^{-1} (0.22 nm). The d-spacing changes slightly as compared to the samples regenerated in EMIMCl because the acetate ion is bigger than the chloride, and its basicity is much lower. When the ionic liquid is added, similarly as before, the scattering peak broadens. However, a new scattering peak is observed at a q of 1.15 nm^{-1} (5.46 nm). This d-spacing is smaller as compared with the EMIMCl. Perhaps this is due to the distribution of ion clusters as a result of the size of the acetate ion. As the concentration of ethanol increases, the morphology also changes. In this case, the 25% ethanol samples exhibit microphase separation with a scattering peak of q of 1.30 nm^{-1} (4.83 nm). All other scattering peak positions are like the 1% ethanol sample. As mentioned before, this is the result of an increase in β-sheet content due to an increase in ethanol concentration. When the ionic liquid is added to this sample, the scattering peak in the low scattering region decreases to

0.73 nm^{-1} (8.60 nm). This value is similar to the biocomposite regenerated in EMIMCl and coagulated with 25% ethanol with the additional ionic liquid. The main difference is located at q of 5.41 nm^{-1} (1.16 nm), which was not observed in that sample. As before, this scattering peak is related to correlation distances between cellulose crystal domains and the β-strands and primary structure, especially the silk II crystalline spacings.

Samples regenerated in EMIMAc and coagulated with hydrogen peroxide at different concentrations is now the focus of attention. The X-ray scattering profiles show a somewhat similar profile as the previous samples regenerated in EMIMCl for both conditions. The main difference is that correlation distance related to the microphase separation changes. For 1% and 25% hydrogen peroxide, this scattering peak is located at q of 0.60 nm^{-1} (10.46 nm) and 0.84 nm^{-1} (7.47 nm), respectively. The addition of ionic liquid into the samples decreases this correlation distance, as previously stated. The ionic cluster correlation distances are smaller for acetate ions. As before, the correlation distance between cellulose crystal domains and the β-strands and primary structure, especially the silk II crystalline spacings, increases from 0.73 nm to 1.16 nm. When the hydrogen peroxide increases to 25%, the cellulose crystallinity and crystal size also increase dramatically. The sharpness of the scattering profiles is bigger than the samples regenerated in EMIMCl. This is indicative of an increase in cellulose crystallites. This X-ray scattering profile also shows microphase separation at q of 0.57 nm^{-1} (11.0 nm) for the samples coagulated in 1% hydrogen peroxide. This correlation distance seems to increase for 25%; however, it is beyond the detection point of the system. This suggests the change in anion has a drastic effect on the correlation distance related to the microphase separation.

In summary, the various X-ray scattering profiles as a function of ionic liquid type, coagulation agent, and additional ionic liquid revealed drastic morphological changes that could impact the material's physicochemical properties and ionic conductivity. The change in ionic liquid type and the addition of ionic liquid cause microphase separation. The change in the coagulation agent causes changes in the protein secondary structures and cellulose structure.

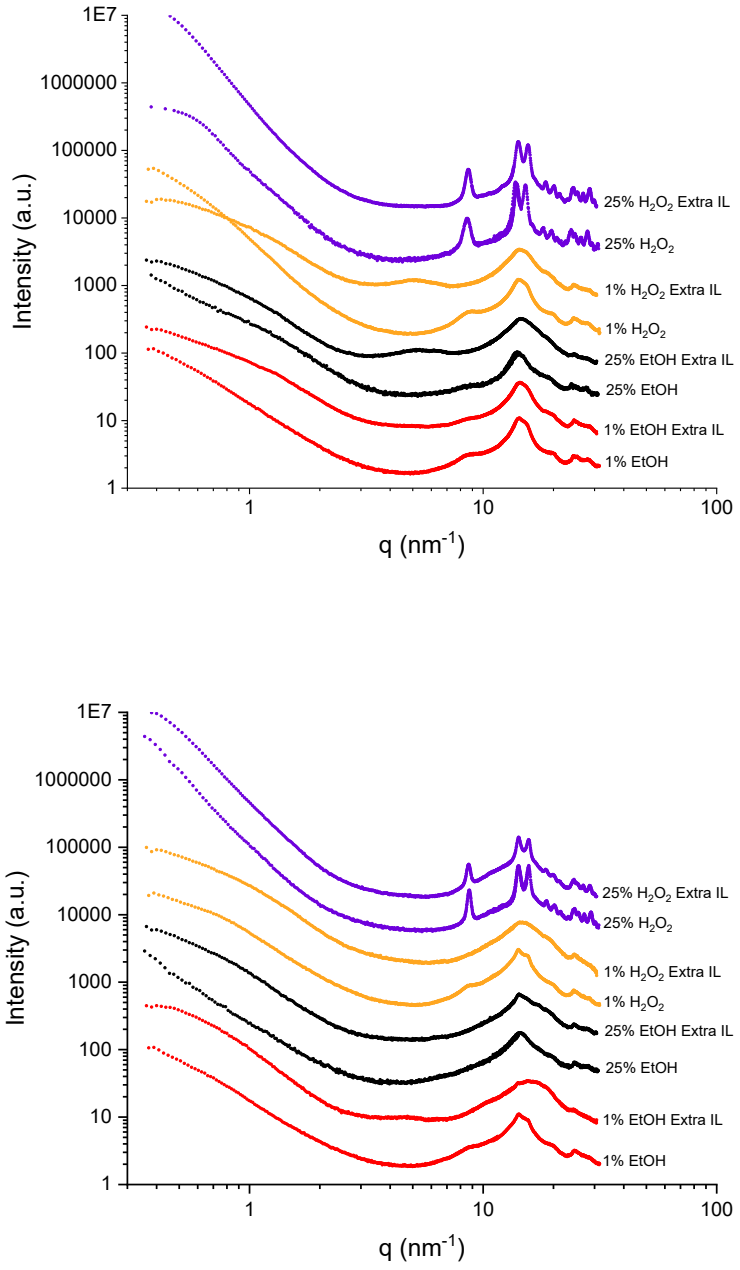

Figure 4.4. *X-ray Scattering profiles for 50% silk and 50% cellulose biocomposites containing either additional or residual ionic liquid. The top graph corresponds to EMIMAc samples, while the bottom graph corresponds to EMIMCl samples.*

4.3.4. Dielectric Relaxation Spectroscopy

The ionic conductivity at various temperatures of each of the sixteen biocomposites sorted by ionic liquid is shown below in **Figure 4.5**, and all of the samples with the additional ionic liquid only stacked on one graph for comparison purposes is shown in **Figure 4.6**. In order to calculate the conductivity, the equation $\sigma = {}^{L}/_{AR}$ was used, where *R* is the resistance calculated at each temperature using the Nyquist plot, *L* is the distance between the two inner electrodes, and *A* is the cross-sectional area of the polymer film. Specifically, the resistance is found using the high *x*-intercept of the semi-circle, which is equal to this value [51] In both of these figures, the logarithm of the conductivity is on the *y*-axis and 1000/Temperature in Kelvin is on the *x*-axis. When looking at the samples made with EMIMAc, all the films with additional ionic liquid had a higher conductivity than those with just residual ionic liquid in the system. It is interesting to note that they follow the same trend as their partners with residual ionic liquid. Specifically, the ionic conductivity is highest for 25% ethanol, followed by 1% hydrogen peroxide, 1% ethanol, and 25% hydrogen peroxide, for the additional ionic liquid EMIMAc samples. This pattern is the same for the EMIMAc samples with residual ionic liquid. These residual ionic liquid samples follow the trend that has been discussed in previous chapters, where increasing β-sheet content also corresponds with higher ionic conductivity. However, when looking at the samples with additional ionic liquid, this trend does not hold. This is most likely due to the high concentration of ionic liquid in the sample, as predicted by the VFT equation. When looking at the EMIMCl samples, again, the samples with additional ionic liquid all had higher ionic conductivity, with the exception of the 25% hydrogen peroxide sample, which seems to have about the same conductivity as the residual sample. When looking at

the residual samples without additional ionic liquid, they follow the β-sheet content trend, with the 1% hydrogen peroxide and ethanol samples being close in conductivity. However, again, when the ionic liquid is added, this trend does not hold. This could mean that there are two parameters that dominate the ionic conduction: ionic concentration and morphology. In the X-ray scattering section, it was noticed that the morphology also changes between the residual and the additional ionic liquid samples, suggesting a possible change in semicrystallinity and the formation of phase separation between silk, cellulose, and the added ionic liquid in the matrix.

Figure 4.6 is used to compare the samples with additional ionic liquid only. In three of the four sample sets, the EMIMAc samples have a higher conductivity than the EMIMCl sample using the same coagulation agent. The only sample set that does not follow this is the 1% ethanol samples. The EMIMCl sample is higher in this case. This could be explained by morphology. In the X-ray scattering section, it was demonstrated that the ionic liquid type has a strong influence on the structure. In this case, the samples with 1% ethanol in EMIMCl displayed a morphology very similar to the samples with EMIMAc. It was the only samples in this set that behave like this, showing a correlation structure with a distance of 1.33 nm. This structure could be related, as mentioned previously, to the interaction of the biomacromolecules with the ionic liquid, which could be strong in this particular sample. Another possibility is that it could be related to the β-sheet content. When comparing the β-sheet content between the 1% ethanol samples with EMIMAc and EMIMCl, a difference of 23.3% was observed, with the 1% ethanol in EMIMCl having the higher β-sheet content. For the other samples, it is the opposite, where the lower β-sheet content has a higher conductivity than the sample with higher β-sheet content. In addition,

one interesting thing to note when looking at the graph is that both 25% ethanol samples are similar in conductivity values, and both 25% hydrogen peroxide samples nearly overlap, suggesting they have nearly the same conductivity as well. Yet, when looking at both 1% ethanol samples, they are far apart and vary in conductivity, and both 1% hydrogen peroxide samples are also much farther apart, again, suggesting they vary in conductivity. This, again, may be related to morphology. The 1% samples showed a larger change in β-sheet content when altering ionic liquid, with the exception of the 25% hydrogen peroxide samples. β-sheet content is known to affect ionic conductivity, and for this reason could be assumed this is one possible reason for the similarity and difference between the 25% samples and 1% samples, respectively.

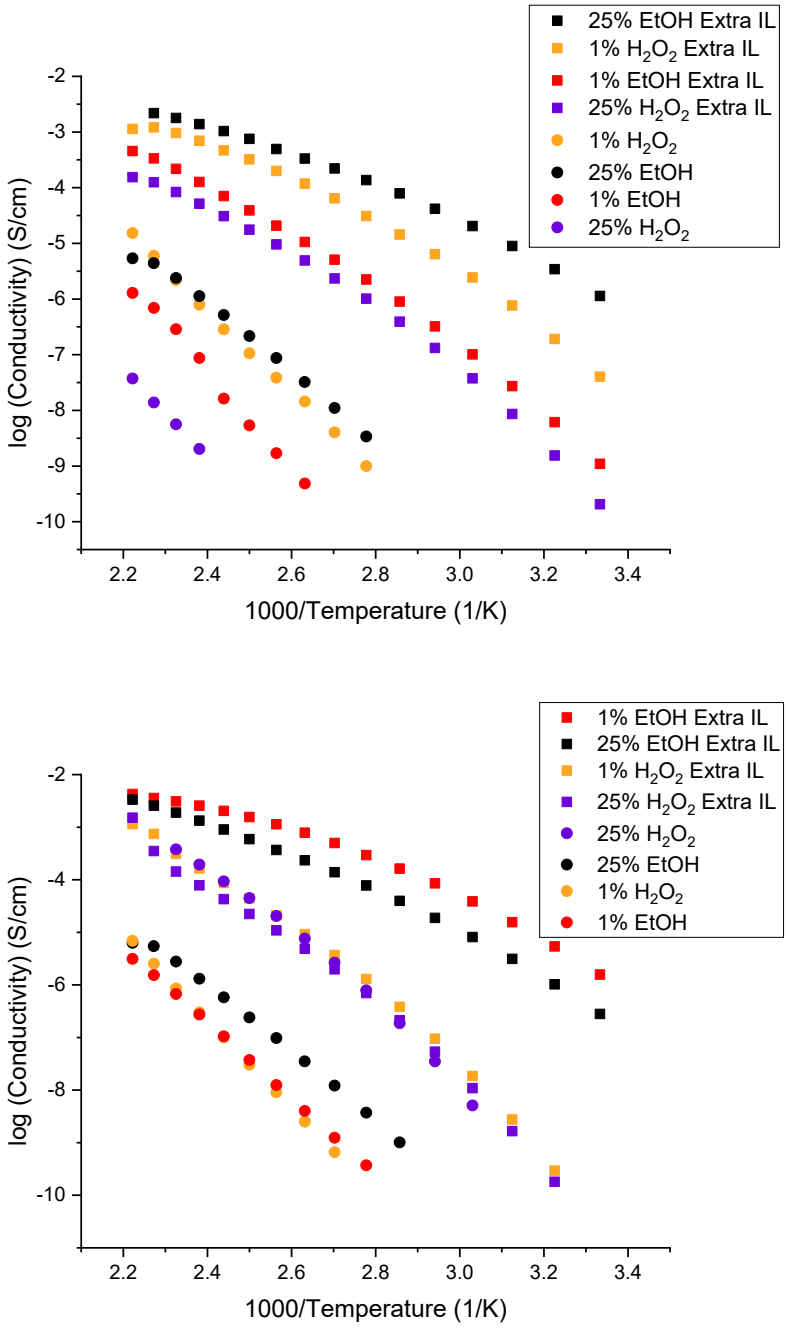

Figure 4.5. *Ionic conductivity versus temperature of the 50% silk and 50% cellulose samples with additional or residual ionic liquid. The top graph corresponds to EMIMAc samples, while the bottom graph corresponds to EMIMCl samples.*

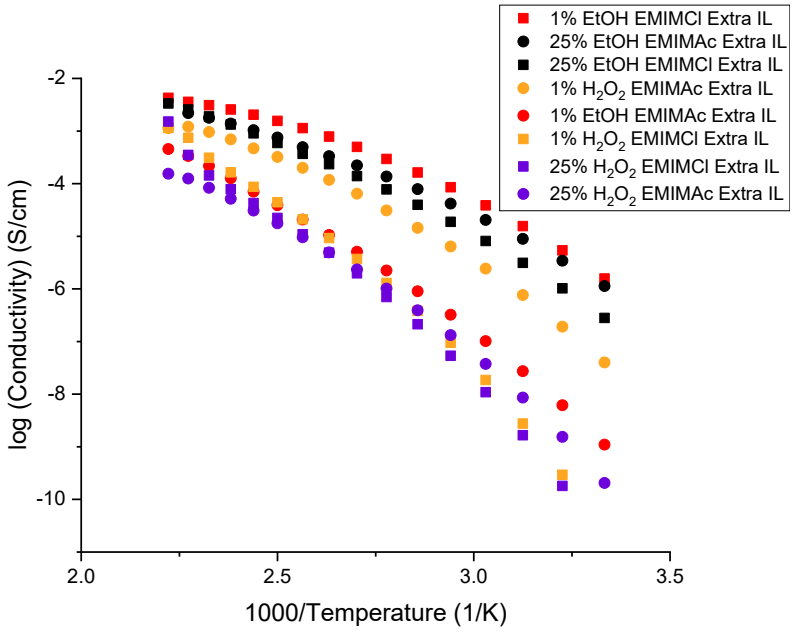

Figure 4.6. *Ionic conductivity versus temperature of all the 50% silk and 50% cellulose samples with only 10% by mass additional ionic liquid added to the sample.*

Figure 4.7 shows T_g/T on the *x*-axis rather than 1000/Temperature. These graphs make it possible to show the effect of morphology on the conductivity. The segmental motion of the macromolecules is corrected with the T_g-normalized ionic conductivity data. When using this graph, it is possible to see if the conductivity data is only driven by changes in the glass transition temperature, or if there is possibly something else occurring within the morphology that can account for changes. Specifically, when all samples collapse onto one line, the glass transition temperature is known to be the only factor in conductivity differences. However, this did not happen for either EMIMAc or EMIMCl samples. Therefore, it is possible to assume other morphological factors are affecting the conductivity, such as β-sheet content, the semicrystallinity of the polysaccharide, cellulose, and even mechanical properties (not included in this study) [51, 83]. Curiously, β-sheet content

did not become an apparent driving force in determining the conductivity trends of these samples with additional ionic liquid. In the X-ray scattering profiles, it is seen the samples become slightly more amorphous than the same samples with only residual ionic liquid. This will enhance conductivity. The reason this may be occurring is because of the disruption of hydrogen bonds within the samples, with differences seen between chloride and acetate ions. This effect is examined in both **Figure 4.8** and **Figure 4.9**. In **Figure 4.8**, samples coagulated with ethanol are explored, and it is apparent the hydrogen bonding between both silk-silk and silk-cellulose interfaces may be interrupted when the additional ionic liquid is added. The anion, chloride ion, is able to bond with the available hydrogen bond donors and disrupt this hydrogen bonding complex. In **Figure 4.9**, samples coagulated with hydrogen peroxide are explored. It is known hydrogen peroxide affects the semicrystallinity of the cellulose. As a result, it is believed the hydrogen bonding of cellulose-cellulose structures is affected, and the chloride anion can instead bond with the hydroxyl groups, interrupting the intermolecular hydrogen bonding within this structure. When the anion is changed with the acetate ion, the correlation distance between the backbones increases, resulting in an increase in ionic conduction. Due to these factors, the structures become more amorphous, which may be a reason for the large increase in conductivity in nearly all the samples. In addition, the nanophase separation was observed in most of the samples with the additional ionic liquid in the X-ray scattering profiles. This could indicate that the ions may be arranged in some type of high ordered structure, such as clusters, as shown in these two schematics. Considering all the results in the figures above, the data suggests morphological properties are crucial to the conductivity, but require further understanding and additional studies to clearly see the patterns not readily

as visible when the additional ionic liquid is added to the samples. For these reasons, it is possible to conclude the addition of ionic liquid changes the morphology and enhances the conductivity.

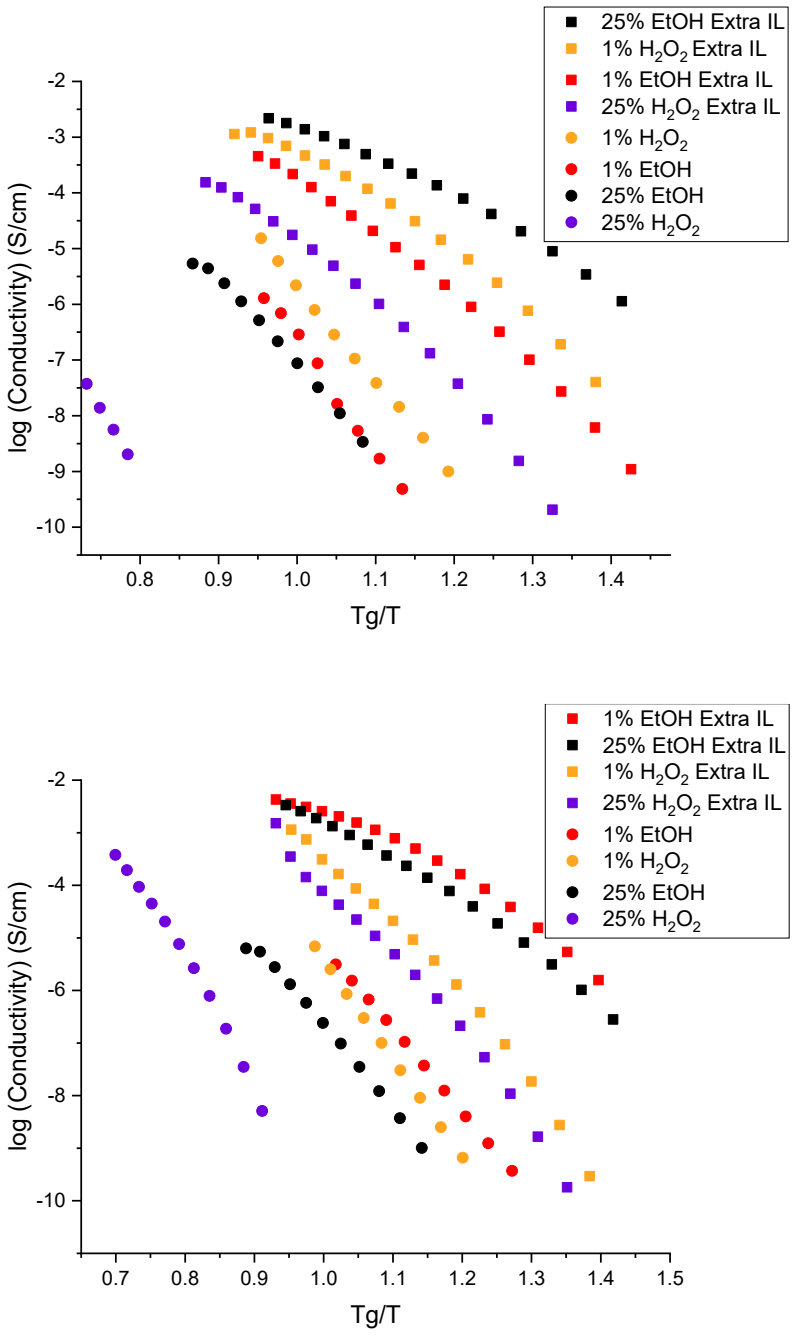

Figure 4.7. *Ionic conductivity data normalized using the glass transition temperatures of the 50% silk and 50% cellulose biocomposites containing additional or residual ionic liquid. The top graph corresponds to EMIMAc samples, while the bottom graph corresponds to EMIMCl samples.*

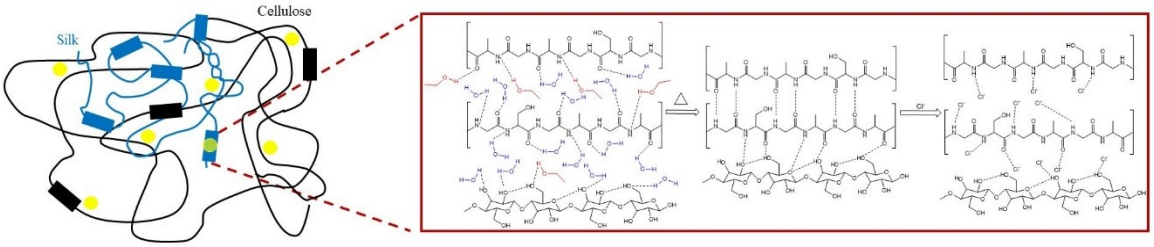

Figure 4.8. Schematic representation of the disruption of hydrogen bonding upon the addition of extra ionic liquid within the biocomposite coagulated with ethanol. The chloride anion, in this example, disrupts the hydrogen bonding between cellulose-cellulose and silk-cellulose interfaces. Also, it shows a possible higher-order structure forms by the ions in clusters.

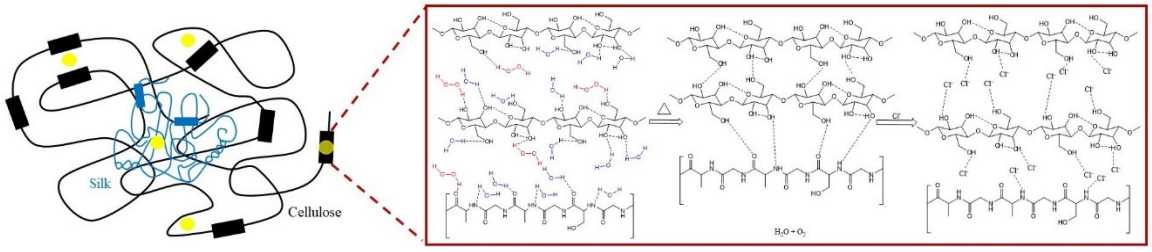

Figure 4.9. Schematic representation of the disruption of hydrogen bonding upon the addition of extra ionic liquid within the biocomposite coagulated with hydrogen peroxide. The chloride anion, in this example, disrupts the hydrogen bonding between cellulose-cellulose interfaces. Also, it shows a possible higher-order structure forms by the ions in clusters.

4.4. Conclusion

The morphological, thermal, and ionic conductivity properties of the biocomposites in this study were altered by adding additional ionic liquid to samples. Every film in this study was made of the composition 50% silk and 50% cellulose. Varying coagulation

agents and ionic liquids were used, and 10% by mass additional ionic liquid was added to each sample and then compared to a sample with the same characteristics, but only with residual ionic liquid. The results of FTIR reveal large differences in not only the secondary structures in the amide I region but also the spectra. The C-N stretch from the imidazolium ring in the ionic liquid increases in absorbance when additional ionic liquid is added, as expected. When the ionic liquid was added to the samples, the secondary structure calculations were random, even when looking at β-sheet content, which is eventually is connected to ionic conductivity. This data, coupled with the FTIR spectra and morphology, suggests that the additional ionic liquid in the biocomposite has a large effect on morphology. Thermal properties investigated through DSC show distinct differences between all the samples, especially those with additional ionic liquid versus residual of the same ionic liquid and coagulant. It was seen that the addition of ionic liquid leads to changes in the glass transition temperature, crystallization peaks, and degradation peaks for each sample. These differences are examples of the changes in morphology upon the addition of the ionic liquid. The X-ray scattering profiles provided evidence of such changes. It is seen there is generally a slight decrease in semicrystallinity and nanophase separation in the samples with additional ionic liquid. Since it is known ionic liquid is efficient at disturbing the hydrogen bonding in both silk and cellulose, maybe this addition is breaking some of the hydrogen bonds formed between the polymer and polysaccharide, resulting in a more amorphous phase. All of these results are taken into account when looking at trends in ionic conductivity. Nearly all films with additional ionic liquid had a higher conductivity than the same film with only residual ionic liquid. However, these samples do not follow the β-sheet trend previously mentioned in other studies and chapters.

Instead, their conductivity is dependent on ion content and morphology. Further investigation into the full effects of the increase in ionic liquid concentration on the biocomposites is required to fully understand how morphology, thermal, and conductivity properties are interrelated. However, this work demonstrates that it is possible to enhance conductivity using small percentages of ionic liquid by mass. This could become useful when developing a device that requires high conductivity in applications as medical devices or bio-electrolytes as batteries.

Chapter 5

Conclusion and Future Studies

5.1. Conclusion

Throughout this entire investigation, different ionic liquids were used to dissolve cellulose and silk, both of which are difficult to break down under normal conditions. Different coagulation agents of different percentages and chemicals were also used to remove the ionic liquid and regenerate the materials. The first study in this investigation into morphology and conductivity focused on varying composition and coagulation agents while keeping ionic liquid the same and studying its effects on morphology, conductivity, thermal, and mechanical properties. FTIR results showed differences in secondary structure content, with the 10% ethanol samples having a higher β-sheet content than the 1% ethanol samples. When looking at thermal properties, TGA revealed the 100% regenerated silk sample had the highest thermal stability in terms of weight-loss percentage, end temperature, and onset temperature. When mixture composition varied, the thermogram displayed a closer number of peaks to the dominating polymer. Films made with 75% silk were bimodal, which correlates with 100% silk, which has one peak, and 25% silk samples were trimodal, corresponding to the trimodal derivative of 100% cellulose. DSC was used to find glass transition temperatures, and these temperatures were all very similar except for the 100% regenerated silk, which had a slightly higher glass transition temperature than the rest. X-ray scattering revealed samples made with 25% silk were more semicrystalline than 75% silk samples. AFM nanoindentation showed elastic moduli of the 25% silk samples could be used to relate to conductivity, with the higher

elastic modulus of these two samples relating to lower conductivity. Finally, conductivity was able to be related to the previously mentioned characterization tests. The conductivity of the 75% silk samples was higher than the 25% silk samples. These followed the β-sheet content trend, with higher β-sheet content correlating with higher ionic conductivity. However, 25% silk samples were flipped in this case; that is, cellulose is now the dominating material. The sample with higher β-sheet content had a lower conductivity. As a result, β-sheet content no longer is the crucial determinant in ionic conductivity when cellulose dominates in composition, but instead, semicrystallinity of the cellulose and mechanical properties are.

The second study focused on samples with equal composition rather than varied, as seen in the first study. As a result, the ionic liquid and coagulation agents are varied to determine their effect on the morphological, thermal, mechanical, and conductive properties of the biocomposites. Again, FTIR results were used to compare spectra and secondary structures of the four biocomposites. β-sheet content went from highest to lowest in the order of the EMIMCl sample coagulated with hydrogen peroxide, followed by the EMIMCl sample coagulated with ethanol, the EMIMAc sample coagulated with ethanol and finally, the EMIMAc sample coagulated with hydrogen peroxide. This trend becomes important later when looking at ionic conductivity. Thermal properties were measured using both TGA and DSC to look at thermal stability and glass transition temperatures, respectively. TGA revealed the EMIMCl sample coagulated with ethanol had the highest onset temperature, and one of the lowest weight-loss percentages. DSC showed this same sample also had the highest glass transition temperature. Also, when comparing coagulant baths, the ethanol samples had much higher glass transition temperatures than both

hydrogen peroxide samples. X-ray scattering showed hydrogen peroxide samples were more semicrystalline than ethanol samples, and this helped prove the morphology is dependent on the coagulation agent. AFM based nanoindentation revealed that hydrogen peroxide samples also had the highest hardness when compared to the ethanol samples. This makes sense since these samples are much more brittle than ethanol samples. Ultimately, β-sheet content was related to conductivity results. Conductivity went from highest to lowest in the order of the EMIMCl hydrogen peroxide film, EMIMCl and EMIMAc ethanol samples, and finally, the EMIMAc hydrogen peroxide sample. This is the same order in which the β-sheet content goes from highest to lowest. This study ultimately proved that higher β-sheet content resulted in higher ionic conductivity.

In the third and final study, the additional ionic liquid was added to samples, and the resulting morphological, thermal, and conductive properties are examined. All samples were created from a balanced composition of 50% silk and 50% cellulose, while two ionic liquids were used with four different coagulation agents. The ionic liquid was added as 10% of the mass of the biocomposite. Samples without additional ionic liquid, and instead only residual, were used for comparison purposes to see what the addition does to the sample. FTIR results showed differences in the spectra. Specifically, the C-O and O-H stretches were modified when adding the ionic liquid, with some becoming more prominent, rounder, or drastically lower in absorbance compared to the samples without added ionic liquid. Also, the shoulder peak related to the C-N stretch from the ionic liquid imidazolium ring grew larger in absorbance for some samples where the ionic liquid was added. Secondary structures were calculated for these samples, and no pattern was observed. It appeared as if the change in structures did not have a clear pattern when

looking at the difference in ionic liquid or coagulation agent. The only slight pattern observed was the more significant difference in β-sheet content in samples coagulated with 1% aqueous solutions compared to 25% solutions. The single sample that did not follow this trend was the EMIMCl sample coagulated with 1% hydrogen peroxide. The 1% aqueous solutions had strong morphological changes. DSC was used to investigate the thermal properties of the samples. When looking at the heat flow scans, crystallization, and degradation peaks changed with the addition of ionic liquid. Specifically, some peaks shifted, disappeared, or were formed. This was seen in all the heat flow scans, where some samples showed more drastic effects than others. Glass transition temperatures were also obtained using this characterization test. The differences in temperatures with and without additional ionic liquid were again generally random. However, it was seen the 1% coagulation agent samples showed a decrease in glass transition temperature with the addition of ionic liquid, while 25% coagulation agent samples showed an increase. X-ray scattering showed there was a slight increase in amorphous nature and nanophase separation when the ionic liquid was added. The samples with only residual ionic liquid were more semicrystalline than the additional ionic liquid samples; however, dramatic morphological changes were apparent when the extra ionic liquid was added. This could be due to the breakage of hydrogen bonds since the ionic liquid is known to be capable of destroying these bonds in both silk and cellulose. This breakage might cause the formation of ordered ionic structure into clusters. Finally, when looking at the ionic conductivity, it was seen that nearly all samples with additional ionic liquid were more conductive than those with residual ionic liquid. The previously used β-sheet content trend was not easily observed in these samples in connection with the ionic conductivity. Instead, the samples

are in completely random order and do not increase with increasing β-sheet content. This may be due to the high ion concentration, which causes morphological changes. The addition of ionic liquid becomes extremely important in conductivity changes, with morphological property changes needing further investigation to fully understand their connection to the conductivity when extra ionic liquid is added to samples.

5.2. Future Studies

Throughout this entire investigation, the purpose has been to connect ionic conductivity to morphological changes in the biocomposites. This has been successful through the use of several characterization tests exploring morphological, thermal, and mechanical properties. The data obtained from these tests are useful in connecting to conductivity at the nano and macro scales. There is a desire to learn more about how the properties at the nanoscale level impact the macroscale. For example, there is a desire to learn more about interfaces in the material between silk and cellulose, silk and silk, and cellulose and cellulose, and how they affect the conductivity. These interfaces can change the arrangement of materials and bonding between the polymers within the biocomposite, leading to possible new channels or ways for ions to move, either more or less efficiently throughout the material. Also, there is a need to understand how exactly β-sheet content leads to enhanced conductivity. In each of the studies presented here, this observation was seen. However, the reason for this phenomenon is not fully understood. Perhaps the β-sheets give the ions specific regions on which to travel more efficiently by gliding along the surface rather than getting trapped in the amorphous regions. Another possibility is that the β-sheets are enhancing phase separation. This is a phenomenon that needs to be investigated much more thoroughly to understand why these results are being seen.

Stemming from this, the way in which secondary structures are formed, along with semicrystalline regions within the sample, needs to be studied further. There are interactions between the polymer chains of both the protein and polysaccharide, but more understanding needs to be emphasized on how the hydroxide and amine groups assemble and result in the secondary structures and semicrystalline regions observed. Finally, it would be interesting to investigate precisely how to determine which morphological property would be the driving force in conductivity. For example, in each of the three chapters, different conditions for fabrication were used to create biocomposites with novel properties. Each of these samples resulted in specific morphological properties being the driving force in conductivity, including β-sheet content, cellulose semicrystallinity, mechanical properties, and ion content. More experiments need to be performed to determine which of these is the most important in specific cases.

A possible way to predict the molecular structure, resulting secondary structures, semicrystallinity of the system, as well as ionic conductivity, would be to use computational methods. Using CHARMM-GUI, the properties and structure of the elements forming the material may be simulated in this program and help predict the morphology of systems when using different ionic liquids, coagulation agents, temperature, relative humidity, and composition. This would allow for the understanding of how each component, polysaccharide and protein, influence the resulting matrix. Ultimately, the prediction of properties would allow for the creation of biocomposites based on necessary properties for distinct applications. For example, the prediction of ionic conductivity would allow for the production of batteries that are high enough in conductivity to fulfill specific jobs.

5.3 Contributors/Authors

- Research advisor and author on all papers: Dr. David Salas-de la Cruz, Associate Professor of Chemistry; Rutgers University-Camden
- Committee member and author on Chapter 2 and 3 papers: Dr. Guillaume Lamoureux, Associate Professor of Chemistry; Rutgers University–Camden
- Committee member and author on Chapter 2 and 3 papers: Dr. Sean M. O'Malley, Associate Professor & Chair of Physics; Rutgers University – Camden
- Author on Chapters 2-4 papers: Dr. Xiao Hu, Associate Professor of Physics and Astronomy and of Biomedical and Translational Sciences; Rowan University
- Author on Chapter 2 and 3 papers, AFM characterization testing and analysis: Cory Trout, Ph.D. Candidate in Applied Physics; Rutgers University Newark
- Author on Chapters 2-4 papers, X-ray scattering testing: Stacy Love, Ph.D. Student in Center for Computation and Integrative Biology; Rutgers University-Camden
- Author on Chapter 2-4 papers, assistance with characterization tests: Karleena Rybacki, Undergraduate Student of Center for Computational and Integrative Biology; Rutgers University-Camden
- Author on Chapter 2-4 papers, assistance with characterization tests: Abneris Morales, Undergraduate Student of chemistry; Rutgers University-Camden

5.4 Acknowledgments and Funding

We want to acknowledge the funding provided by the NSF-DMR-RUI (1809354 and 1809541) and NSF-MRI-CMMI (0922946), State of New Jersey ELF Grant to Rutgers-Chemistry, and Rutgers University-Camden Laboratory Start-up funds. NSF-REU

(DBI-1559868) was also used to fund Chapter 3 research partially. We would like to thank people working at the LRSM at the University of Pennsylvania, including Prof. Karen Winey, Prof. Paul Heiney, Benjamin Paren, and Lu Yan for the training and use of Dielectric Relaxation Spectroscopy equipment and X-ray Scattering equipment (DEXS). The DEXS is funded by ARO DURIP (W911NF-17-1-02822), NSF-MRI (17-25969), NSF-MRSEC (17-20530), and University of Pennsylvania. Xiao Hu was supported by the NSF Materials Eng. & Processing program (CMMI-1561966) and Rowan University Start-up Grants. We would also like to thank Sneha Seelam and Emily McDermott, both undergraduates at Rutgers University-Camden, for their help in this project.

5.5 Modifications to Chapter 3 Since Publication

Slight modifications were made to chapter 3 since its publication. These include the alteration of the SEM and X-ray Scattering characterization descriptions, the adjustment of the x-axis of Figures 3.6 and 3.7 to show less white space, and a few word changes throughout the text. In addition, the y-axis of Figure 3.9 was modified to say Elastic Modulus rather than Elasticity, and a few Figure and Title captions were reworded.

References

1. Ratner, B. D.; Hoffman, A. S.; Schoen, F. J.; Lemons, J. E., *Biomaterials science: an introduction to materials in medicine*. Elsevier: 2004.

2. Suh, H., Recent advances in biomaterials. *Yonsei Medical Journal* **1998,** *39* (2), 87-96.

3. Hasirci, V.; Hasirci, N., *Fundamentals of Biomaterials*. Springer: 2018.

4. Yin, J.; Luan, S., Opportunities and challenges for the development of polymer-based biomaterials and medical devices. *Regenerative biomaterials* **2016,** *3* (2), 129-135.

5. Pavlovic, M., What Are Biomaterials? In *Bioengineering: A Conceptual Approach*, Springer International Publishing: Cham, 2015; pp 229-244.

6. Jia, X.; Wang, C.; Zhao, C.; Ge, Y.; Wallace, G. G., Toward biodegradable Mg–air bioelectric batteries composed of silk fibroin–polypyrrole film. *Advanced Functional Materials* **2016,** *26* (9), 1454-1462.

7. Hu, X.; Cebe, P.; Weiss, A. S.; Omenetto, F.; Kaplan, D. L., Protein-based composite materials. *Mater. Today* **2012,** *15* (5), 208-215.

8. Altman, G. H.; Diaz, F.; Jakuba, C.; Calabro, T.; Horan, R. L.; Chen, J.; Lu, H.; Richmond, J.; Kaplan, D. L., Silk-based biomaterials. *Biomaterials* **2003,** *24* (3), 401-416.

9. Hu, X.; Kaplan, D.; Cebe, P., Dynamic protein− water relationships during β-sheet formation. *Macromolecules* **2008,** *41* (11), 3939-3948.

10. Kaplan, D.; Adams, W. W.; Farmer, B.; Viney, C., Silk: biology, structure, properties, and genetics. ACS Publications: 1994.

11. Zhou, L.; Wang, Q.; Wen, J.; Chen, X.; Shao, Z., Preparation and characterization of transparent silk fibroin/cellulose blend films. *Polymer* **2013,** *54* (18), 5035-5042.

12. Lin, N.; Huang, J.; Dufresne, A., Preparation, properties and applications of polysaccharide nanocrystals in advanced functional nanomaterials: a review. *Nanoscale* **2012,** *4* (11), 3274-3294.

13. Dumitriu, S., *Polysaccharides: structural diversity and functional versatility*. CRC press: 2004.

14. Zheng, Y.; Monty, J.; Linhardt, R. J., Polysaccharide-based nanocomposites and their applications. *Carbohydrate research* **2015,** *405*, 23-32.

15. Yu, Y.; Shen, M.; Song, Q.; Xie, J., Biological activities and pharmaceutical applications of polysaccharide from natural resources: A review. *Carbohydrate polymers* **2018,** *183*, 91-101.

16. Helbert, W.; Nishiyama, Y.; Okano, T.; Sugiyama, J., Molecular imaging ofhalocynthia papillosacellulose. *Journal of structural biology* **1998,** *124* (1), 42-50.

17. Sundberg, J.; Toriz, G.; Gatenholm, P., Effect of xylan content on mechanical properties in regenerated cellulose/xylan blend films from ionic liquid. *Cellulose* **2015,** *22* (3), 1943-1953.

18. Samayam, I. P.; Hanson, B. L.; Langan, P.; Schall, C. A., Ionic-liquid induced changes in cellulose structure associated with enhanced biomass hydrolysis. *Biomacromolecules* **2011,** *12* (8), 3091-3098.

19. Song, H.; Niu, Y.; Yu, J.; Zhang, J.; Wang, Z.; He, J., Preparation and morphology of different types of cellulose spherulites from concentrated cellulose ionic liquid solutions. *Soft Matter* **2013,** *9* (11), 3013-3020.

20. Agarwal, V.; Huber, G. W.; Conner Jr, W. C.; Auerbach, S. M., Simulating infrared spectra and hydrogen bonding in cellulose Iβ at elevated temperatures. *The Journal of chemical physics* **2011,** *135* (13), 10B605.

21. Yatsu, L.; Calamari Jr, T.; Benerito, R., Conversion of cellulose I to stable cellulose III. *Textile Research Journal* **1986,** *56* (7), 419-424.

22. Wada, M.; Heux, L.; Sugiyama, J., Polymorphism of cellulose I family: reinvestigation of cellulose IVI. *Biomacromolecules* **2004,** *5* (4), 1385-1391.

23. Cheng, G.; Varanasi, P.; Li, C.; Liu, H.; Melnichenko, Y. B.; Simmons, B. A.; Kent, M. S.; Singh, S., Transition of cellulose crystalline structure and surface morphology of biomass as a function of ionic liquid pretreatment and its relation to enzymatic hydrolysis. *Biomacromolecules* **2011,** *12* (4), 933-941.

24. Li, J.; Nawaz, H.; Wu, J.; Zhang, J.; Wan, J.; Mi, Q.; Yu, J.; Zhang, J., All-cellulose composites based on the self-reinforced effect. *Composites Communications* **2018,** *9*, 42-53.

25. Stanton, J.; Xue, Y.; Waters, J. C.; Lewis, A.; Cowan, D.; Hu, X.; Salas-de la Cruz, D., Structure–property relationships of blended polysaccharide and protein biomaterials in ionic liquid. *Cellulose* **2017,** *24* (4), 1775-1789.

26. Zhang, H.; Wu, J.; Zhang, J.; He, J., 1-Allyl-3-methylimidazolium chloride room temperature ionic liquid: a new and powerful nonderivatizing solvent for cellulose. *Macromolecules* **2005,** *38* (20), 8272-8277.

27. Pinkert, A.; Marsh, K. N.; Pang, S.; Staiger, M. P., Ionic liquids and their interaction with cellulose. *Chemical reviews* **2009,** *109* (12), 6712-6728.

28. Rogers, R. D.; Seddon, K. R., Ionic liquids--solvents of the future? *Science* **2003,** *302* (5646), 792-793.

29. Johnson, K. E., What's an ionic liquid? *Interface-Electrochemical Society* **2007,** *16* (1), 38-41.

30. Earle, M. J.; Seddon, K. R., Ionic liquids. Green solvents for the future. *Pure and applied chemistry* **2000,** *72* (7), 1391-1398.

31. Ohno, H., Functional design of ionic liquids. *Bulletin of the Chemical Society of Japan* **2006,** *79* (11), 1665-1680.

32. Sheldon, R. A.; Lau, R. M.; Sorgedrager, M. J.; van Rantwijk, F.; Seddon, K. R., Biocatalysis in ionic liquids. *Green Chemistry* **2002,** *4* (2), 147-151.

33. Seddon, K. R., A taste of the future. *Nature materials* **2003,** *2* (6), 363-365.

34. Chen, Y.; Cao, Y.; Sun, X.; Mu, T., Hydrogen bonding interaction between acetate-based ionic liquid 1-ethyl-3-methylimidazolium acetate and common solvents. *Journal of Molecular Liquids* **2014,** *190*, 151-158.

35. Green, M. D.; Long, T. E., Designing imidazole-based ionic liquids and ionic liquid monomers for emerging technologies. *Polymer Reviews* **2009,** *49* (4), 291-314.

36. Dupont, J., On the solid, liquid and solution structural organization of imidazolium ionic liquids. *Journal of the Brazilian Chemical Society* **2004,** *15* (3), 341-350.

37. Brehm, M.; Weber, H.; Pensado, A. S.; Stark, A.; Kirchner, B., Proton transfer and polarity changes in ionic liquid–water mixtures: a perspective on hydrogen bonds from ab initio molecular dynamics at the example of 1-ethyl-3-methylimidazolium acetate–water mixtures—Part 1. *Physical Chemistry Chemical Physics* **2012,** *14* (15), 5030-5044.

38. Dhumal, N. R.; Kim, H. J.; Kiefer, J., Molecular interactions in 1-ethyl-3-methylimidazolium acetate ion pair: a density functional study. *The Journal of Physical Chemistry A* **2009,** *113* (38), 10397-10404.

39. Skarmoutsos, I.; Dellis, D.; Matthews, R. P.; Welton, T.; Hunt, P. A., Hydrogen bonding in 1-butyl-and 1-ethyl-3-methylimidazolium chloride ionic liquids. *The journal of physical chemistry B* **2012,** *116* (16), 4921-4933.

40. Swatloski, R. P.; Spear, S. K.; Holbrey, J. D.; Rogers, R. D., Dissolution of cellose with ionic liquids. *Journal of the American chemical society* **2002,** *124* (18), 4974-4975.

41. Phillips, D. M.; Drummy, L. F.; Conrady, D. G.; Fox, D. M.; Naik, R. R.; Stone, M. O.; Trulove, P. C.; De Long, H. C.; Mantz, R. A., Dissolution and regeneration of

Bombyx mori silk fibroin using ionic liquids. *Journal of the American chemical society* **2004,** *126* (44), 14350-14351.

42. Freddi, G.; Romanò, M.; Massafra, M. R.; Tsukada, M., Silk fibroin/cellulose blend films: preparation, structure, and physical properties. *Journal of Applied Polymer Science* **1995,** *56* (12), 1537-1545.

43. Hadadi, A.; Whittaker, J. W.; Verrill, D. E.; Hu, X.; Larini, L.; Salas-de la Cruz, D., A Hierarchical Model To Understand the Processing of Polysaccharides/Protein-Based Films in Ionic Liquids. *Biomacromolecules* **2018,** *19* (10), 3970-3982.

44. DeFrates, K.; Markiewicz, T.; Callaway, K.; Xue, Y.; Stanton, J.; Salas-de la Cruz, D.; Hu, X., Structure–property relationships of Thai silk–microcrystalline cellulose biocomposite materials fabricated from ionic liquid. *International journal of biological macromolecules* **2017,** *104*, 919-928.

45. Stanton, J.; Xue, Y.; Pandher, P.; Malek, L.; Brown, T.; Hu, X.; Salas-de la Cruz, D., Impact of ionic liquid type on the structure, morphology and properties of silk-cellulose biocomposite materials. *Int. J. Biol. Macromol.* **2018,** *108*, 333-341.

46. Salas-de la Cruz, D. Morphology and ionic conductivity of polymerized ionic liquids. University of Pennsylvania, 2011.

47. Klein, R. J.; Zhang, S.; Dou, S.; Jones, B. H.; Colby, R. H.; Runt, J., Modeling electrode polarization in dielectric spectroscopy: Ion mobility and mobile ion concentration of single-ion polymer electrolytes. *The Journal of chemical physics* **2006,** *124* (14), 144903.

48. Lee, M.; Choi, U. H.; Colby, R. H.; Gibson, H. W., Ion conduction in imidazolium acrylate ionic liquids and their polymers. *Chemistry of Materials* **2010,** *22* (21), 5814-5822.

49. Chen, H.; Choi, J.-H.; Salas-de la Cruz, D.; Winey, K. I.; Elabd, Y. A., Polymerized ionic liquids: the effect of random copolymer composition on ion conduction. *Macromolecules* **2009,** *42* (13), 4809-4816.

50. Pereira, R. F.; Brito-Pereira, R.; Gonçalves, R.; Silva, M. P.; Costa, C. M.; Silva, M. M.; de Zea Bermudez, V. n.; Lanceros-Méndez, S., Silk fibroin separators: A step toward lithium-ion batteries with enhanced sustainability. *ACS applied materials & interfaces* **2018,** *10* (6), 5385-5394.

51. Salas-de la Cruz, D.; Green, M. D.; Ye, Y.; Elabd, Y. A.; Long, T. E.; Winey, K. I., Correlating backbone-to-backbone distance to ionic conductivity in amorphous polymerized ionic liquids. *Journal of Polymer Science Part B: Polymer Physics* **2012,** *50* (5), 338-346.

52. Qian, X.; Gu, N.; Cheng, Z.; Yang, X.; Wang, E.; Dong, S., Methods to study the ionic conductivity of polymeric electrolytes using ac impedance spectroscopy. *Journal of Solid State Electrochemistry* **2001,** *6* (1), 8-15.

53. Aliofkhazraei, M., *Modern electrochemical methods in nano, surface and corrosion science*. BoD–Books on Demand: 2014.

54. Krongelb, S.; Division, E. S. E.; Meeting, E. S., *Magnetic Materials, Processes, and Devices VII and Electrodeposition of Alloys: Proceedings of the International Symposia*. Electrochemical Society: 2003.

55. Sudha, L.; Sukumar, R.; Uma Rao, K., Evaluation of activation energy (Ea) profiles of nanostructured alumina polycarbonate composite insulation materials. *International Journal of Materials, Mechanics and Manufacturing* **2014,** *2* (1), 96-100.

56. Wilson, D. B.; Irwin, D. C., Genetics and properties of cellulases. In *Recent progress in bioconversion of lignocellulosics*, Springer: 1999; pp 1-21.

57. Yamashiki, T.; Matsui, T.; Saitoh, M.; Matsuda, Y.; Okajima, K.; Kamide, K.; Sawada, T., Characterisation of cellulose treated by the steam explosion method. Part 3: Effect of crystal forms (cellulose I, II and III) of original cellulose on changes in morphology, degree of polymerisaion, solubility and supermolecular structure by steam explosion. *British polymer journal* **1990,** *22* (3), 201-212.

58. Marsh, R. E.; Corey, R. B.; Pauling, L., An investigation of the structure of silk fibroin. *Biochimica et Biophysica acta* **1955,** *16*, 1-34.

59. Takahashi, Y.; Gehoh, M.; Yuzuriha, K., Structure refinement and diffuse streak scattering of silk (Bombyx mori). *International journal of biological macromolecules* **1999,** *24* (2-3), 127-138.

60. Chen, X.; Knight, D. P.; Shao, Z.; Vollrath, F., Regenerated Bombyx silk solutions studied with rheometry and FTIR. *Polymer* **2001,** *42* (25), 09969-09974.

61. Chen, X.; Shao, Z.; Marinkovic, N. S.; Miller, L. M.; Zhou, P.; Chance, M. R., Conformation transition kinetics of regenerated Bombyx mori silk fibroin membrane monitored by time-resolved FTIR spectroscopy. *Biophysical chemistry* **2001,** *89* (1), 25-34.

62. Blessing, B.; Trout, C.; Morales, A.; Rybacki, K.; Love, S. A.; Lamoureux, G.; O'Malley, S. M.; Hu, X.; Salas-de la Cruz, D., Morphology and ionic conductivity relationship in silk/cellulose biocomposites. *Polymer International* **2019,** *68* (9), 1580-1590.

63. Love, S. A.; Popov, E.; Rybacki, K.; Hu, X.; Salas-de la Cruz, D., Facile treatment to fine-tune cellulose crystals in cellulose-silk biocomposites through hydrogen peroxide. *International Journal of Biological Macromolecules* **2020**.

64. Murphy, E., The dependence of the conductivity of cellulose, silk and wool on their water content. *Journal of Physics and Chemistry of Solids* **1960,** *16* (1-2), 115-122.

65. Johnson, K. L.; Kendall, K.; Roberts, A., Surface energy and the contact of elastic solids. *Proceedings of the Royal Society of London. Series A, Mathematical and Physical Sciences* **1971,** *324* (1558), 301-313.

66. Ebenstein, D. M.; Pruitt, L. A., Nanoindentation of biological materials. *Nano Today* **2006,** *1* (3), 26-33.

67. Notbohm, J.; Poon, B.; Ravichandran, G., Analysis of nanoindentation of soft materials with an atomic force microscope. *Journal of Materials Research* **2012,** *27* (1), 229-237.

68. Griffin, P. J.; Freyer, J. L.; Han, N.; Geller, N.; Yin, X.; Gheewala, C. D.; Lambert, T. H.; Campos, L. M.; Winey, K. I., Ion Transport in Cyclopropenium-Based Polymerized Ionic Liquids. *Macromolecules* **2018,** *51* (5), 1681-1687.

69. Hu, X.; Kaplan, D.; Cebe, P., Determining beta-sheet crystallinity in fibrous proteins by thermal analysis and infrared spectroscopy. *Macromolecules* **2006,** *39* (18), 6161-6170.

70. Um, I. C.; Kweon, H.; Park, Y. H.; Hudson, S., Structural characteristics and properties of the regenerated silk fibroin prepared from formic acid. *International Journal of Biological Macromolecules* **2001,** *29* (2), 91-97.

71. He, S.-J.; Valluzzi, R.; Gido, S. P., Silk I structure in Bombyx mori silk foams. *International Journal of Biological Macromolecules* **1999,** *24* (2–3), 187-195.

72. Gong, Z.; Huang, L.; Yang, Y.; Chen, X.; Shao, Z., Two distinct [small beta]-sheet fibrils from silk protein. *Chemical Communications* **2009,** (48), 7506-7508.

73. Asakura, T.; Yamane, T.; Nakazawa, Y.; Kameda, T.; Ando, K., Structure of Bombyx mori silk fibroin before spinning in solid state studied with wide angle x-ray scattering and 13C cross-polarization/magic angle spinning NMR. *Biopolymers* **2001,** *58* (5), 521-525.

74. Asakura, T.; Okushita, K.; Williamson, M. P., Analysis of the Structure of Bombyx mori Silk Fibroin by NMR. *Macromolecules* **2015,** *48* (8), 2345-2357.

75. Liu, X.; Zhang, K.-Q., *Silk Fiber—Molecular Formation Mechanism, Structure-Property Relationship and Advanced Applications*. IntechOpen: 2014.

76. Saitoh, H.; Ohshima, K.-i.; Tsubouchi, K.; Takasu, Y.; Yamada, H., X-ray structural study of noncrystalline regenerated Bombyx mori silk fibroin. *International Journal of Biological Macromolecules* **2004,** *34* (5), 259-265.

77. Nieduszynski, I.; Preston, R., Crystallite size in natural cellulose. *Nature* **1970,** *225*, 273-274.

78. Eyley, S.; Thielemans, W., Surface modification of cellulose nanocrystals. *Nanoscale* **2014,** *6* (14), 7764-7779.

79. French, A. D., Idealized powder diffraction patterns for cellulose polymorphs. *Cellulose* **2014,** *21* (2), 885-896.

80. Fernandes, A. N.; Thomas, L. H.; Altaner, C. M.; Callow, P.; Forsyth, V. T.; Apperley, D. C.; Kennedy, C. J.; Jarvis, M. C., Nanostructure of cellulose microfibrils in spruce wood. *Proceedings of the National Academy of Sciences* **2011,** *108* (47), E1195-E1203.

81. Kafle, K.; Shin, H.; Lee, C. M.; Park, S.; Kim, S. H., Progressive structural changes of Avicel, bleached softwood, and bacterial cellulose during enzymatic hydrolysis. *Scientific Reports* **2015,** *5*.

82. Lee, M.; Choi, U. H.; Salas-de la Cruz, D.; Mittal, A.; Winey, K. I.; Colby, R. H.; Gibson, H. W., Imidazolium polyesters: structure–property relationships in thermal behavior, ionic conductivity, and morphology. *Advanced Functional Materials* **2011,** *21* (4), 708-717.

83. Ye, Y.; Elabd, Y. A., Anion exchanged polymerized ionic liquids: High free volume single ion conductors. *Polymer* **2011,** *52* (5), 1309-1317.

84. Bruce, P. G., *Solid State Electrochemistry*. Cambridge University Press: 1997.

85. Vainio, U.; Maximova, N.; Hortling, B.; Laine, J.; Stenius, P.; Simola, L. K.; Gravitis, J.; Serimaa, R., Morphology of Dry Lignins and Size and Shape of Dissolved Kraft Lignin Particles by X-ray Scattering. *Langmuir* **2004,** *20* (22), 9736-9744.

86. Kamel, S., Nanotechnology and its applications in lignocellulosic composites, a mini review. *Express Polymer Letters* **2007,** *1* (9), 546-575.

87. Migonney, V., *Biomaterials*. John Wiley & Sons, Incorporated: Somerset, UNITED STATES, 2014.

88. Ratner, B. D.; Hoffman, A. S.; Yaszemski, M. J.; Lemons, J. E.; Schoen, F. J., *Biomaterials Science : An Introduction to Materials in Medicine*. Elsevier Science & Technology: San Diego, UNITED STATES, 2012.

89. Kim, G.-T.; Jeong, S.; Xue, M.-Z.; Balducci, A.; Winter, M.; Passerini, S.; Alessandrini, F.; Appetecchi, G., Development of ionic liquid-based lithium battery prototypes. *Journal of Power Sources* **2012,** *199*, 239-246.

90. Osada, I.; de Vries, H.; Scrosati, B.; Passerini, S., Ionic-liquid-based polymer electrolytes for battery applications. *Angewandte Chemie International Edition* **2016,** *55* (2), 500-513.

91. Seki, S.; Kobayashi, Y.; Miyashiro, H.; Ohno, Y.; Usami, A.; Mita, Y.; Kihira, N.; Watanabe, M.; Terada, N., Lithium secondary batteries using modified-imidazolium room-temperature ionic liquid. *The Journal of Physical Chemistry B* **2006,** *110* (21), 10228-10230.

92. Guo, Q., *Polymer morphology: principles, characterization, and processing*. John Wiley & Sons: 2016.